MICROMECHANICS OF PIEZOCOMPOSITES

BY

LI LI

B.S., University of Science and Technology of China, 1985
M.S., University of Illinois at Urbana-Champaign, 1992

THESIS

Submitted in partial fulfillment of the requirements
for the degree of Doctor of Philosophy in Theoretical and Applied Mechanics
in the Graduate College of the
University of Illinois at Urbana-Champaign, 1995

Urbana, Illinois

Report Documentation Page

Form Approved
OMB No. 0704-0188

1. REPORT DATE	2. REPORT TYPE	3. DATES COVERED
JUL 1995		**00-00-1995 to 00-00-1995**

4. TITLE AND SUBTITLE	5a. CONTRACT NUMBER
Micromechanics of Piezocomposites	5b. GRANT NUMBER
	5c. PROGRAM ELEMENT NUMBER
6. AUTHOR(S)	5d. PROJECT NUMBER
	5e. TASK NUMBER
	5f. WORK UNIT NUMBER
7. PERFORMING ORGANIZATION NAME(S) AND ADDRESS(ES) **University of Illinois at Urbana-Champaign,Department of Theoretical and Applied Mechanics,Urbana,IL,61801**	8. PERFORMING ORGANIZATION REPORT NUMBER
9. SPONSORING/MONITORING AGENCY NAME(S) AND ADDRESS(ES)	10. SPONSOR/MONITOR'S ACRONYM(S)
	11. SPONSOR/MONITOR'S REPORT NUMBER(S)

12. DISTRIBUTION/AVAILABILITY STATEMENT
Approved for public release; distribution unlimited

13. SUPPLEMENTARY NOTES

14. ABSTRACT

Over the past two decades, materials engineers have developed piezoelectric-polymer composite materials that enable effective electromechanical properties to be tailored for a specific application. These materials are made by combining conventional piezoelectric ceramics with piezoelectrically passive polymers in a variety of geometrical configurations. As with any composite material, the properties and behavior of piezocomposites are highly dependent on the properties of the constituent materials and the local arrangement of the different phases. In particular, the ceramic-polymer interface plays an important role in determining the electromechanical coupling in the piezocomposite. In this dissertation, the electromechanical behavior of 1-3 piezocomposites is investigated from both theoretical and experimental stand points. Theoretical investigations centered on the development of a micromechanics model for predicting the local fields and effective behavior in piezocomposites with 1-3 connectivity. Since the presence of a thin interlayer or polymer coating around the ceramic rods can influence the local interaction between the piezoceramic and polymer matrix and change the overall performance of the composite, a finite composite cylinder model was developed to incorporate an interlayer with varying properties. Experimental studies focused on probing the surface displacements of 1-3 piezocomposites using a scanning heterodyne laser interferometer. Static surface displacements of 1-3 PZT rodepoxy samples with different interphase regions were measured and correlated with the effective low-frequency performance of the composite. Several types of interphase region were considered. Coatings with elastic moduli lower than that of the epoxy matrix were applied to the rods. The influence of a silane coupling agent was also investigated. Experimental displacement profiles were compared with micromechanical predictions using the finite composite cylinder model. The results demonstrate that the presence of an interphase between the piezoceramic and the polymer matrix influences the local deformations and changes the overall performance of the composite. Thus, the interphase plays an important role in determining the electromechanical coupling in the piezocomposite. The study of electromechanical coupling in piezocomposites was further developed by investigating the hydrostatic performance of 1-3 piezocomposites, an important issue in design of piezocomposites for low-frequency applications. Emphasis was placed on determining the stress transferred between the passive matrix and the active piezoceramic rods and using this data to indicate the level of electromechanical coupling. The stress field in the piezoelectric ceramic under hydrostatic loading was predicted using the

15. SUBJECT TERMS

16. SECURITY CLASSIFICATION OF:			17. LIMITATION OF ABSTRACT	18. NUMBER OF PAGES	19a. NAME OF RESPONSIBLE PERSON
a. REPORT	b. ABSTRACT	c. THIS PAGE			
unclassified	**unclassified**	**unclassified**	**Same as Report (SAR)**	**130**	

UNIVERSITY OF ILLINOIS AT URBANA-CHAMPAIGN

THE GRADUATE COLLEGE

JULY 1995

WE HEREBY RECOMMEND THAT THE THESIS BY

LI LI

ENTITLED MICROMECHANICS OF PIEZOCOMPOSITES

BE ACCEPTED IN PARTIAL FULFILLMENT OF THE REQUIREMENTS FOR

THE DEGREE OF DOCTOR OF PHILOSOPHY

Director of Thesis Research

Head of Department

Committee on Final Examination†

Chairperson

† Required for doctor's degree but not for master's.

UNIVERSITY OF ILLINOIS AT URBANA-CHAMPAIGN

GRADUATE COLLEGE DEPARTMENTAL FORMAT APPROVAL

THIS IS TO CERTIFY THAT THE FORMAT AND QUALITY OF PRESENTATION OF THE THESIS SUBMITTED BY LI LI AS ONE OF THE REQUIREMENTS FOR THE DEGREE OF DOCTOR OF PHILOSOPHY IS ACCEPTABLE TO THE DEPARTMENT OF THEORETICAL AND APPLIED MECHANICS.

Full Name of Department, Division or Unit

July 28, 1995

Date of Approval

James W. Phillips

Departmental Representative

MICROMECHANICS OF PIEZOCOMPOSITES

Li Li, Ph.D.
Department of Theoretical and Applied Mechanics
University of Illinois at Urbana-Champaign, 1995
Nancy R. Sottos, Advisor

ABSTRACT

Over the past two decades, materials engineers have developed piezoelectric-polymer composite materials that enable effective electromechanical properties to be tailored for a specific application. These materials are made by combining conventional piezoelectric ceramics with piezoelectrically passive polymers in a variety of geometrical configurations. As with any composite material, the properties and behavior of piezocomposites are highly dependent on the properties of the constituent materials and the local arrangement of the different phases. In particular, the ceramic-polymer interface plays an important role in determining the electromechanical coupling in the piezocomposite. In this dissertation, the electromechanical behavior of 1-3 piezocomposites is investigated from both theoretical and experimental stand points.

Theoretical investigations centered on the development of a micromechanics model for predicting the local fields and effective behavior in piezocomposites with 1-3 connectivity. Since the presence of a thin interlayer or polymer coating around the ceramic rods can influence the local interaction between the piezoceramic and polymer matrix and change the overall performance of the composite, a finite composite cylinder model was developed to incorporate an interlayer with varying properties. Experimental studies focused on probing the surface displacements of 1-3 piezocomposites using a scanning heterodyne laser interferometer. Static surface displacements of 1-3 PZT rod-epoxy samples with different interphase regions were measured and correlated with the

effective low-frequency performance of the composite. Several types of interphase region were considered. Coatings with elastic moduli lower than that of the epoxy matrix were applied to the rods. The influence of a silane coupling agent was also investigated. Experimental displacement profiles were compared with micromechanical predictions using the finite composite cylinder model. The results demonstrate that the presence of an interphase between the piezoceramic and the polymer matrix influences the local deformations and changes the overall performance of the composite. Thus, the interphase plays an important role in determining the electromechanical coupling in the piezocomposite.

The study of electromechanical coupling in piezocomposites was further developed by investigating the hydrostatic performance of 1-3 piezocomposites, an important issue in design of piezocomposites for low-frequency applications. Emphasis was placed on determining the stress transferred between the passive matrix and the active piezoceramic rods and using this data to indicate the level of electromechanical coupling. The stress field in the piezoelectric ceramic under hydrostatic loading was predicted using the analytical micromechanical model developed and a finite-element model as well. Optimal electromechanical coupling was achieved when a certain favorable stress field was induced in the piezoceramic. The influence of such design parameters as the matrix stiffness, the interphase stiffness, the interphase thickness, the Poisson's ratio of the polymers, and piezoceramic rod aspect ratio on the hydrostatic performance of 1-3 piezocomposites was also investigated. Although the current work is focused on the electromechanical behavior of 1-3 piezocomposites at low-frequency, the research results and conceptual understanding obtained have importance for optimizing the design of piezocomposites in other applications as well.

To

my mother and father

ACKNOWLEDGMENTS

I would like to express my sincere gratitude to my advisor, Prof. Nancy R. Sottos, for her encouragement and guidance during the course of this dissertation. I am grateful to the members of my dissertation committee, Prof. K. Jimmy Hsia, Prof. James W. Phillips and Prof. Scott R. White, for their valuable time and comments.

The financial support of the Office of Naval Research is greatly appreciated. This work was supported under grant N00014-92-J-1620.

I would like to thank my wife, Qiong (June), for her support, love and patience during the last five years. Finally, I would like to extend my deep appreciation to my parents who have always been a driving force in my pursuit of success.

TABLE OF CONTENTS

LIST OF TABLES

LIST OF FIGURES

LIST OF SYMBOLS

a_o amplitude of the sample beam in interferometric measurements

a_r amplitude of the reference beam in interferometric measurements

A_o sample beam in interferometric measurements

A_r reference beam in interferometric measurements

$A_i^{(i)}$ constant used in solving the boundary value problem in Chapter 2

c_{ijkl} elastic stiffness coefficient

c_{pq} elastic stiffness coefficient by the compressed notation

d diameter of the piezoceramic rod

d_{ijk} piezoelectric charge coefficient

d_{mm} piezoelectric charge coefficient by the compressed notation

d_h hydrostatic piezoelectric charge coefficient

$\bar{d}_h$ effective hydrostatic piezoelectric charge coefficient

D_i dielectric displacement vector component

E_i electric field intensity vector component

f_o frequency of the sample beam in interferometric measurements

f_r frequency of the reference beam in interferometric measurements

$F^{(i)}$ Love's stress function

E function used in solving the boundary value problem in Chapter 2

e_{ijk} piezoelectric coefficient

e_{mn} piezoelectric coefficient by the compressed notation

g_{ijk} piezoelectric voltage coefficient

g_{mn} piezoelectric voltage coefficient by the compressed notation

g_h hydrostatic piezoelectric voltage coefficient

$\bar{g}_h$ hydrostatic piezoelectric voltage coefficient

$g_{in}^{(i)}$ function used in solving the boundary value problem in Chapter 2

$h_{in}^{(i)}$ function used in solving the boundary value problem in Chapter 2

H half length of the interlayer center region

I intensity of the interferogram

I_0 zero-order modified Bessel function of the first kind

I_1 first-order modified Bessel function of the first kind

$\mathbf{k}^i$ unit vector in the incident direction

$\mathbf{k}^o$ unit vector in the observation direction

K_0 zero-order modified Bessel function of the second kind

K_1 first-order modified Bessel function of the second kind

l half length of the piezoceramic rod

n_j outwardly directed surface normal

p_i surface traction vector component

P_i polarization vector component

$P_{\max}$ maximum load in thin-section push-out test

$\tilde{P}_j$ constant used in solving the boundary value problem in Chapter 2

r radial component of a cylindrical coordinate system

r_1 radius of a piezoceramic rod

r_2 radius of a coated piezoceramic rod

r_3 radius of a piezocomposite cylinder

s_{ijkl} elastic compliance coefficient

s_{pq} elastic compliance coefficient by the compressed notation

S_{ij} strain component

t time

T_{ij} stress component

u displacement in the r direction

u_i displacement vector component

U function used in solving the boundary value problem in Chapter 2

w displacement in the z direction

W function used in solving the boundary value problem in Chapter 2

v_f piezoceramic rod volume fraction

V voltage

x_i component of a Cartesian system

$Y^{(i)}$ Young's modulus

z axial component of a cylindrical coordinate system

α_i constant used in solving the boundary value problem in Chapter 2

β_i constant used in solving the boundary value problem in Chapter 2

γ_i constant used in solving the boundary value problem in Chapter 2

$\delta\Delta$ change of optical path

ε_{ij} dielectric constant

$\bar{\varepsilon}_{ij}$ effective dielectric constant

θ hoop component of a cylindrical coordinate system

$\zeta^{(i)}$ constant used in solving the generalized plane strain problem in Chapter 2

$\eta^{(i)}$ constant used in solving the generalized plane strain problem in Chapter 2

λ wave length of light

μ_n eigenvalue for the boundary value problem in Chapter 2

$\nu^{(i)}$ Poisson's ratio

$\xi^{(i)}$ constant used in solving the generalized plane strain problem in Chapter 2

τ_0 average interfacial shear strength

ϕ scalar electric potential

ψ_o spatial phase of the sample beam in interferometric measurements

ψ_r spatial phase of the reference beam in interferometric measurements

ψ phase of the interferogram

$\Delta\psi$ change of the phase of the interferogram

Ω outer surface of a composite cylinder

1. INTRODUCTION

1.1 Piezoelectricity

Piezoelectricity, according to the original definition of the phenomenon discovered by Jacques and Pierre Curie brothers in 1880 (Jaffe, Cook and Jaffe, 1971),* is the ability of certain crystalline materials to develop an electric charge which is proportional to a mechanical stress. Soon after this discovery, it was also realized that the converse effect of a geometric strain developing upon the application of a voltage, was also inherent in these materials. Thus, piezoelectricity is an interaction between electrical and mechanical systems. The direct piezoelectric effect, the development of an electric charge upon the application of a mechanical stress, is described as (Nye, 1957)

$$P_i = d_{ijk} T_{jk} \tag{1.1}$$

where P_i is a component of the electric polarization (charge per unit area), d_{ijk} are the components of piezoelectric coupling coefficient, and T_{jk} are components of the applied mechanical stress. The converse effect, the development of a mechanical strain upon the application of an electric field to the piezoelectric, is described by

$$S_{ij} = d_{ijk} E_k \tag{1.2}$$

where S_{ij} is the strain produced and E_k is the applied electric field. In both cases, the piezoelectric coefficients d_{ijk} are numerically identical.

The piezoelectric effect is strongly linked to the crystal symmetry. Piezoelectricity is limited to 20 of the 32 crystal classes, known as point groups, for all crystalline materials. The crystals

* References are arranged alphabetically by author in the Bibliography, beginning on page 102.

which exhibit piezoelectricity have one common feature: the absence of a center of symmetry within the crystal. This absence of symmetry leads to polarity, the one-way direction of the charge vector. Most of the important piezoelectric materials are also ferroelectric, which is characterized by a transformation to high symmetry, non-piezoelectric phase at higher temperatures. The transformation temperature is known as the Curie temperature. For any piezoelectric materials, the Curie temperature is the absolute maximum use temperature.

Polycrystalline materials in which the crystal axes of the grains are randomly oriented exhibit zero net piezoelectric effect. Piezoelectric polycrystalline ceramics were discovered in the 1940s, soon followed by the development of the poling process in which the randomly oriented crystal axes are suitably aligned by the application of a strong electric field at elevated temperatures. After that discovery, researchers continued to develop better and more stable materials. Lead zirconate titanate (PZT) was first introduced in 1954 and has become the most widely used piezoceramic. Today piezoelectric ceramics, or piezoceramics, are used more widely than piezoelectric crystals.

Generally, mechanical stress T_{ij} and electric field E_i are coupled within a piezoelectric solid medium. Constitutive relations for a piezoelectric material can be written as (IEEE, 1978)

$$S_{ij} = s^E_{ijkl} T_{kl} + d_{ijk} E_k \tag{1.3}$$

$$D_i = d_{ijk} T_{jk} + e^T_{ij} E_j \tag{1.4}$$

where D_i is the dielectric displacement given by the sum $e_0 E_i + P_i$. Here e_{ij} are dielectric constants, s_{ijkl} are elastic compliance components, and ε_0 is the dielectric constant of free space. Superscripts T and E have been added to e_{ij} and s_{ijkl} to show that these constants describe dielectric and elastic properties measured under conditions of constant stress and constant electric field, respectively.

The constitutive relations can be written in alternate forms, such as

$$T_{ij} = c^{E}_{ijkl} S_{kl} - e_{ijk} E_k \tag{1.5}$$

$$D_i = e_{ijk} S_{jk} + \varepsilon^{S}_{ij} E_j . \tag{1.6}$$

where the piezoelectric constants e_{ijk} are related to the piezoelectric constants d_{imn} and the elastic stiffness constants c^{E}_{mnjk} by the expression $e_{ijk} = d_{imn} c^{E}_{mnjk}$. An abbreviated subscript notation can be introduced to reduce the three subscripts of the piezoelectric constants and the four subscripts of the elastic constants into two subscripts. Relations between the piezoelectric constants and elastic constants with full subscripts and those with abbreviated subscripts are outlined in the *IEEE Standard on Piezoelectricity* (IEEE, 1978).

In Eqs. (1.3) and (1.4) the strain and electric field are derivable from the mechanical displacement and electric potential as

$$S_{ij} = \tfrac{1}{2}\left(u_{i,j} + u_{j,i}\right) \tag{1.7}$$

$$E_i = -f_{,i} . \tag{1.8}$$

To complete the formulation of the stationary linear theory of piezoelectricity, one must supplement Eqs. (1.3) to (1.6) with the equations of elastic equilibrium and the electrostatic equation, which in the absence of body forces and free electric charge are

$$T_{ij,j} = 0 \tag{1.9}$$

$$D_{i,i} = 0 . \tag{1.10}$$

Piezoelectric materials are widely used in hydro- and electro-acoustics, electro-optics, communications, and measurement techniques (Dokmeci, 1980). The research on piezoelectric materials and piezoelectricity has resulted in a huge volume of literature. Two references that provide an overview on this topic are included in the Bibliography (IEEE, 1978; Ikeda, 1990).

1.2 Piezoelectric Composites

1.2.1 Background

Composite piezoelectric materials have been developed over the past the two decades which enable the effective properties to be tailored for a specific application. These materials are made by combining conventional piezoelectric ceramics with piezoelectrically passive polymers in a variety of geometrical configurations. Piezocomposites were originally developed for underwater hydrophone applications in the low-frequency range, but have also been extended to such other applications as ultrasonic transducers for acoustic imaging and medical applications (Gururaja, Safari et al., 1988) . Recently, piezoelectric ceramics are being investigated for use as sensor or actuator elements in smart structures.

Unlike structural composite materials which are formulated to optimize mechanical properties, piezocomposites are designed to maximize their coupled field behavior. The key consideration in designing a piezocomposite, whether as a sensor or as an actuator, is to ensure the maximum efficiency in electromechanical energy conversion (Smith, 1992). As with any composite material, the properties and behavior of piezocomposites are highly dependent on the properties of the constituent materials and the local arrangement of the different phases. In particular, the ceramic-polymer interface plays an important role in determining the electromechanical coupling in the piezocomposite (Li and Sottos, 1995).

The first attempt at making piezoelectric composites occurred in the early 1970s when researchers tried to develop flexible piezoelectrics (Pauer, 1973). In the late 1970s a

comprehensive research program on piezoceramic-polymer composites was carried out at Pennsylvania State University. Piezocomposites have since become an important addition to the range of composite materials, and numerous papers have been written regarding manufacturing, modeling, vibration modes, and various applications. Piezocomposites have advantages over single-phase piezoelectrics for certain applications. Gururaja et al. summarized the pioneering work on piezocomposites at Pennsylvania State University in a section of the book *Electronic Ceramics* published in 1988 (Gururaja, Safari et al., 1988). A review article of all work prior to 1989 was presented by Smith at the 1989 IEEE Ultrasonic Symposium (Smith, 1989).

A variety of piezocomposites can be made by combining piezoelectric ceramics with passive polymers. These composites are commonly classified according to their connectivity (Newnham, 1986). Connectivity in a composite refers to the way in which the different phases are arranged, and is designated by such numbers as 1-3, 3-2, etc. The numbers represent the number of dimensions in which each phase is self-connected. Some piezocomposites with different connectivities are shown in Fig. 1.1.

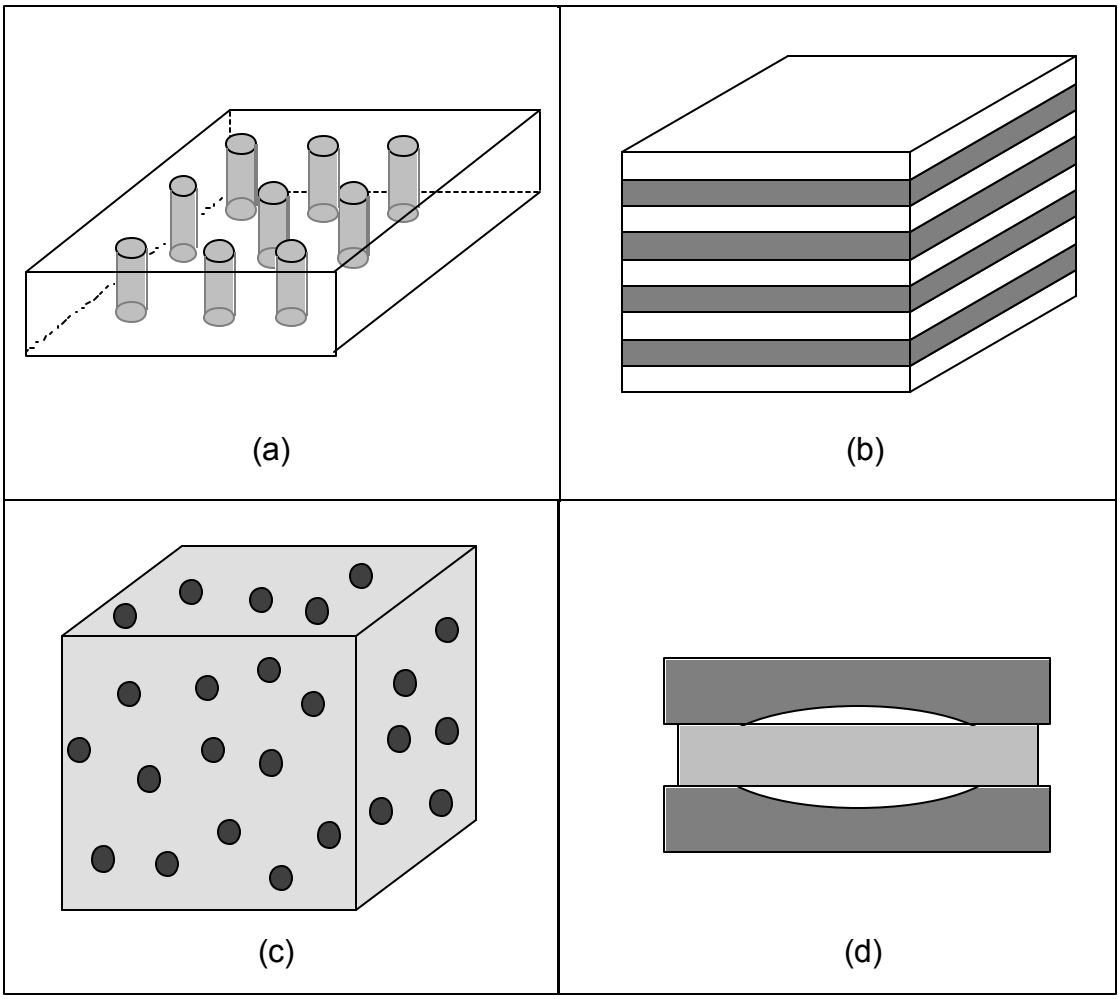

Fig. 1.1. Piezocomposites with different connectivities.

(a) A 1-3 piezocomposite with piezoceramic rods embedded in a continuous polymer matrix.

(b) A 2-2 piezocomposite found in multilayer piezoceramic actuators.

(c) A piezocomposite with 0-3 connectivity.

(d) The moonie 2-2 piezocomposite, an advanced piezoelectric sensor and actuator.

The literature regarding piezocomposites can be roughly divided into five basic categories: (1) micromechanical analysis of low-frequency effective elastic, dielectric, and piezoelectric behavior and use of low-frequency parameters in hydrophone and one-dimensional transducer models; (2) prediction of the various resonance modes associated with the composites and their coupling to one another (including experimental and finite-element analysis studies); (3) presentation of techniques for composite manufacture; (4) reports of composite transducer performance results and (5) reports on smart-material and smart structure systems applications. Papers written on the first topic are most critical for the current investigation and are summarized in the following section.

1.2.2 Micromechanical Models

Most of the existing micromechanics works concerning the electro-mechanical coupling phenomena in piezocomposites involve the derivation of relations for the effective elastic constants and effective piezoelectric constants. Classical models, such as the Voigt uniform-strain model and the Reuss uniform-stress model, have been utilized (Lees and Davidson, 1977). More refined models include the parallel-serial model (Haun and Newnham, 1986) and the model by Smith (1993). These simple models are all based on assumption that either strain components or the corresponding stress components are equal in the two phases. In addition, Jensen (1991) has used a concentric cylinder model to characterize 1-3 piezocomposites. This model, which estimates the six technically most important constants of the nine constants in the *e*-set, consists of a piezoelectric rod and a concentric elastic tube subjected to axisymmetric load. Because the displacement assumption introduced in Jensen's study is equivalent to that of generalized plane strain, the concentric tube model also leads to homogeneous strain along the axial direction of the cylinder. Cao, Zhang and Cross (1992) presented a theoretical study on the static performance of 1-3 piezocomposites. Inhomogeneous displacement profiles were derived for a single-rod composite and a single-tube 1-3 ceramic-polymer composite under

uniaxial or hydrostatic stress. The effect of lateral stress is not included in the study and the analysis is essentially one-dimensional.

Recent developments of micromechanics of piezocomposites also include the work of Dunn and Taya (1993), who estimated the effective properties of a two-phase piezocomposite using dilute, self-consistent, Mori-Tanaka and differential micromechanical models. Progress in micromechanical analysis of piezocomposites has also been made by Benveniste (1993a, 1993b) and Benveniste and Dvorak (1992). Benveniste and Dvorak (1992) extended the uniform-fields concept for the uncoupled mechanical case to the piezoelectric behavior in binary piezocomposites and derived the universal relations for the effective piezoelectric constants of such composites. More recently, Benveniste (1994a) combined the composite cylinder assemblage model with these universal relations for the effective piezoelectric constants and derived some exact expressions for the effective constants that characterize two-phase fibrous piezocomposites. A summary and discussion of his recent contribution in the micromechanics of piezocomposites was given by Benveniste recently (Benveniste, 1994b).

1.2.3 Experimental Characterization

Experimental characterization of piezocomposites can be roughly divided into two categories. The first is associated with measurements of dielectric and piezoelectric constants by using either the direct piezoelectric effect or the resonance method outlined in the IEEE Standard on Piezoelectricity (IEEE, 1978). The second involves measuring surface velocity and displacement at certain frequencies by laser probing methods.

Klicker (1980) used a Berlincourt piezo d_{33} meter and measured the d_{33} value at different locations on the surface of a 1-3 piezocomposite. He then chose the average value as the measured effective piezoelectric constant $\bar{d}_{33}$ of the composite. This method was also used

recently by Kim, Rittenmyer and Kahn (1993). Klicker (1980) also used a static technique based on the direct effect to measure the effective hydrostatic piezoelectric constant $\bar{d}_h$.

Measuring surface displacement at resonance frequencies using a laser heterodyne interferometer was reported by Wang and Auld (1985) and Gururaja, Schulze et al. (1985). Rittenmyer and Dubbelday (1992) reported a direct measurement of the temperature-dependent piezoelectric coefficients of composite materials by laser-Doppler vibrometry. Zhang et al. (1994) measured the surface displacement profile of a 2-2 piezocomposite at low frequency (200 Hz) by a double-beam laser dilatometer. The low-frequency performance of a single rod piezocomposite has been investigated by Sottos et al. (1993) by a laser heterodyne interferometer. However, characterizing the static deformation in piezocomposites has not been presented in the literature.

1.3 Overview of the Dissertation

This dissertation investigates the behavior of electromechanical coupling in piezocomposites. The work focuses on several topics of practical importance that have not been adequately addressed in the existing literature. These topics include the load transfer between the piezoceramic and the polymer matrix; the micromechanics of piezocomposites, incorporating any existing interphase between the ceramic and the matrix; the optimization of electromechanical coupling by varying interphase properties; and the experimental characterization of the performance of piezocomposites for low frequency applications. Special attention has been given to the important issue of tailoring the ceramic-polymer interface/interphase for optimal performance. The study has been carried out from both theoretical and experimental standpoints. The balance was achieved by conducting innovative laser interferometric measurements and developing analytical and numerical (finite-element) models to study the performance of the materials. Although the work is focused on the

performance of 1-3 piezocomposites at low frequency, the research results have importance for other applications as well.

In Chapter 2, a concentric composite cylinder model is developed to study the local fields and effective behavior in piezoceramic rod-polymer composites with 1-3 connectivity. This composite model is similar to the well known "composite cylinder assemblage" model, which is used commonly for continuous fiber composites. This composite model is characterized by its finite length, chosen to equal to that of the embedded piezoceramic rods. The displacement, stress, and electric fields in the composite model are found using the displacement and electrical potentials. The solution is compared with solutions of simple plane strain-models and other micromechanical models. The effective piezoelectric constants $\bar{d}_{33}$ and $\bar{d}_{31}$ for the composite are then calculated using the derived solution.

Chapter 3 focuses on experimental characterization of local deformation in 1-3 piezocomposites. A laser heterodyne micro-interferometer is used to study the static performance of 1-3 piezocomposites. Surface displacement profiles of composite samples are measured around the piezoceramic rods. The displacement profiles are also compared with the analytical results.

Electromechanical coupling is discussed further in Chapter 4. The focus is on optimizing hydrostatic performance of 1-3 piezocomposites, an important issue in design of piezocomposites for low-frequency applications. Emphasis was placed on determining the stress transferred between the passive matrix and the active piezoceramic rods and using this data to indicate the level of electromechanical coupling. The stress field in the piezoelectric ceramic is studied using the solutions developed in Chapter 2. Optimal electromechanical coupling can be achieved when a certain favorable stress field is induced in the piezoceramic. The influence of such design parameters as the matrix stiffness, the interphase stiffness, the

interphase thickness, the Poisson's ratio of the polymer and piezoceramic rod aspect ratio, on the hydrostatic performance of 1-3 piezocomposites is investigated.

Finally, Chapter 5 summarizes the important findings of the thesis. Concluding remarks and recommendations for future work are presented.

2. MICROMECHANICS OF PIEZOCOMPOSITES

2.1 Introduction

Consider a 1-3 piezocomposite with an array of aligned piezoelectric ceramic rods embedded in a passive polymer matrix, as shown in Fig. 2.1. The piezoelectric ceramic rods are a poled polycrystalline ceramic which is isotropic in a plane normal to the poling direction and effectively exhibits transversely isotropic elastic behavior. Piezoelectric ceramics of this family, such as barium titanate, lead zirconate titanate (PZT), lead metaniobate, and modified lead titanate, have been developed for a broad spectrum of applications. The convention is to define the poling direction as the x_3 direction and the x_1 - x_2 plane as the isotropic plane. Constitutive relations for piezoceramics poled in the x_3 direction can then be written in the matrix form (IEEE, 1978)

$$\begin{Bmatrix} D_1 \\ D_2 \\ D_3 \end{Bmatrix} = \begin{bmatrix} 0 & 0 & 0 & 0 & d_{15} & 0 \\ 0 & 0 & 0 & d_{15} & 0 & 0 \\ d_{31} & d_{31} & d_{33} & 0 & 0 & 0 \end{bmatrix} \begin{Bmatrix} T_{11} \\ T_{22} \\ T_{33} \\ T_{23} \\ T_{13} \\ T_{12} \end{Bmatrix} + \begin{bmatrix} e_{11}^T & 0 & 0 \\ 0 & e_{11}^T & 0 \\ 0 & 0 & e_{33}^T \end{bmatrix} \begin{Bmatrix} E_1 \\ E_2 \\ E_3 \end{Bmatrix} \tag{2.1}$$

$$\begin{Bmatrix} S_{11} \\ S_{22} \\ S_{33} \\ S_{23} \\ S_{13} \\ S_{12} \end{Bmatrix} = \begin{bmatrix} s_{11}^E & s_{12}^E & s_{13}^E & 0 & 0 & 0 \\ s_{12}^E & s_{11}^E & s_{13}^E & 0 & 0 & 0 \\ s_{13}^E & s_{13}^E & s_{33}^E & 0 & 0 & 0 \\ 0 & 0 & 0 & s_{44}^E & 0 & 0 \\ 0 & 0 & 0 & 0 & s_{44}^E & 0 \\ 0 & 0 & 0 & 0 & 0 & 2(s_{11}^E - s_{12}^E) \end{bmatrix} \begin{Bmatrix} T_{11} \\ T_{22} \\ T_{33} \\ T_{23} \\ T_{13} \\ T_{12} \end{Bmatrix} + \begin{bmatrix} 0 & 0 & d_{31} \\ 0 & 0 & d_{31} \\ 0 & 0 & d_{33} \\ 0 & d_{15} & 0 \\ d_{15} & 0 & 0 \\ 0 & 0 & 0 \end{bmatrix} \begin{Bmatrix} E_1 \\ E_2 \\ E_3 \end{Bmatrix}. \tag{2.2}$$

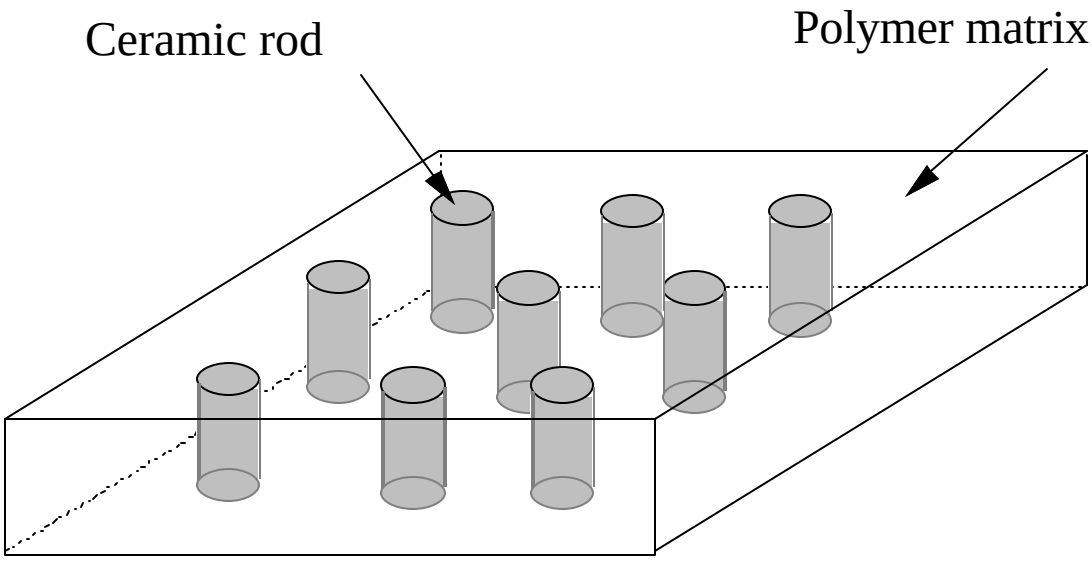

Fig. 2.1. Schematic of a 1-3 piezocomposite.

The concentric finite composite cylinder model shown in Fig. 2.2 is chosen as the representative volume element (RVE) for the 1-3 piezocomposite. The length of the composite cylinder model is chosen as the length of the piezoceramic rods embedded in the polymer matrix. If the length of the rods approaches infinity i.e., if the rods are continuous, this composite cylinder model will approach the well known "composite cylinder assemblage" of Hashin and Rosen (1964) and Hashin (1979).

Because the actual stress transfer is through the interface between the rods and the matrix, the incorporation of any existing interphase region into the micromechanical analysis of 1-3 piezocomposites may be important for understanding composite behavior. A thin interlayer is introduced between the piezoceramic rods and the matrix in the micromechanical model. It is proposed that the presence of this thin interlayer can influence the effective behavior of the composite and change the sensitivity. Both the interlayer and the matrix are considered as isotropic and nonpiezoelectric.

2.2 Formulation of the Micromechanical Analysis

As shown in the schematic diagram of the three-phase composite cylinder in Fig. 2.2, the region $r < r_1$ (ceramic rod), the region $r_1 < r < r_2$ (interlayer) and the region $r_2 < r < r_3$ (embedding polymer matrix) are denoted by superscripts (1), (2) and (3), respectively. The composite aggregate is subjected to homogeneous boundary conditions in the form

$$p_i(\Omega) = T_{ij}^0 n_j \tag{2.3}$$

$$\phi(\Omega) = -E_i^0 x_i \tag{2.4}$$

where p_i denotes the traction vector, f is the electric potential, T_{ij}^0 is a constant stress tensor, E_i^0 is a constant electric field vector, n_j is the normal of, Ω, the outer surface of

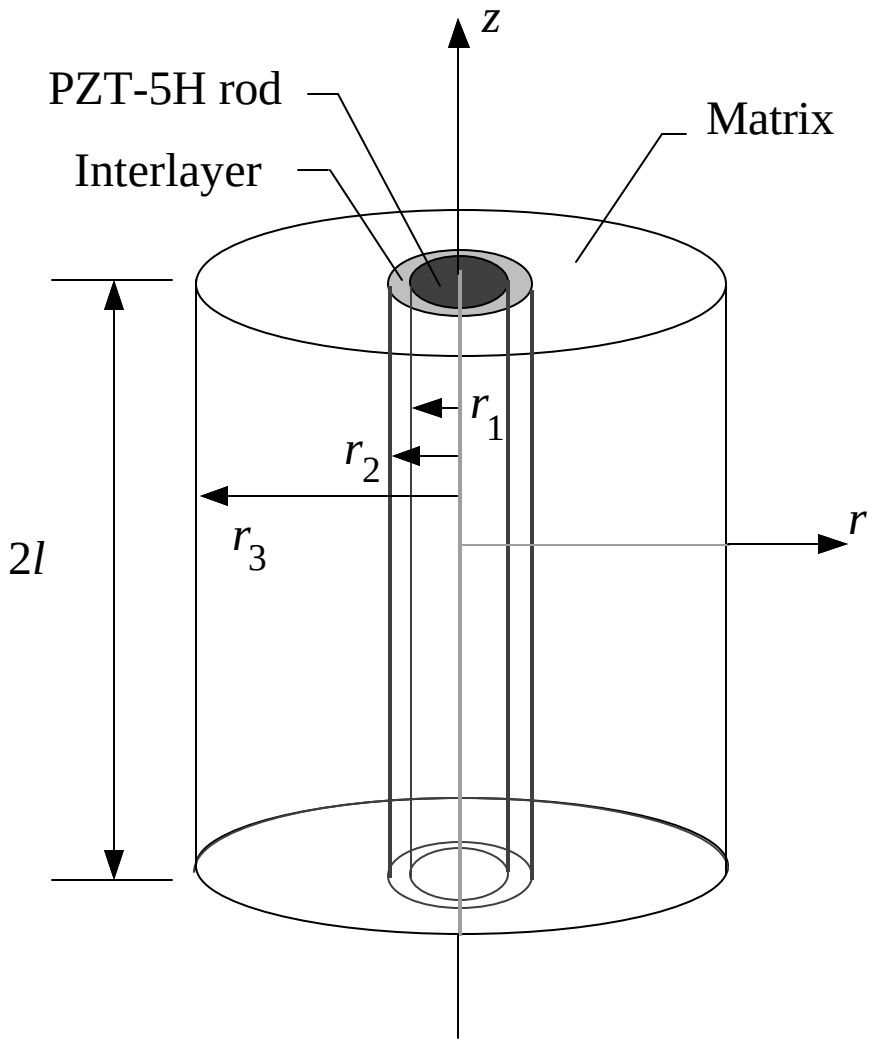

Fig. 2.2. Schematic of the three-phase composite cylinder model.

the composite cylinder, and x_i denotes the components of the Cartesian system. Because of the symmetry of the geometry and the boundary conditions, the deformation is also axisymmetric.

In cylindrical coordinates, the axially symmetric state of deformation is characterized by

$$u_r^{(i)} = u^{(i)}(r,z). \tag{2.5}$$

$$u_q^{(i)} = 0 \tag{2.6}$$

$$u_z^{(i)} = w^{(i)}(r,z) \qquad (i = 1,2,3). \tag{2.7}$$

For a transversely isotropic piezoelectric rod the constitutive relations can be written in cylindrical coordinates as

$$T_{rr}^{(1)} = c_{11}^{(1)}S_{rr}^{(1)} + c_{12}^{(1)}S_{\theta\theta}^{(1)} + c_{13}^{(1)}S_{zz}^{(1)} - e_{31}^{(1)}E_z^{(1)} \tag{2.8}$$

$$T_{\theta\theta}^{(1)} = c_{12}^{(1)}S_{rr}^{(1)} + c_{11}^{(1)}S_{\theta\theta}^{(1)} + c_{13}^{(1)}S_{zz}^{(1)} - e_{31}^{(1)}E_z^{(1)} \tag{2.9}$$

$$T_{zz}^{(1)} = c_{13}^{(1)}S_{rr}^{(1)} + c_{13}^{(1)}S_{\theta\theta}^{(1)} + c_{33}^{(1)}S_{zz}^{(1)} - e_{33}^{(1)}E_z^{(1)} \tag{2.10}$$

$$T_{rz}^{(1)} = c_{44}^{(1)}S_{rz}^{(1)} - e_{15}^{(1)}E_r^{(1)} \tag{2.11}$$

$$T_{r\theta}^{(1)} = T_{\theta z}^{(1)} = 0 \tag{2.12}$$

$$D_r^{(1)} = e_{15}^{(1)}S_{rz}^{(1)} + \varepsilon_{11}^{(1)}E_r^{(1)} \tag{2.13}$$

$$D_\theta^{(1)} = 0 \tag{2.14}$$

$$D_z^{(1)} = e_{31}^{(1)}S_{rr}^{(1)} + e_{31}^{(1)}S_{\theta\theta}^{(1)} + e_{33}^{(1)}S_{zz}^{(1)} + \varepsilon_{33}^{(1)}E_z^{(1)}. \tag{2.15}$$

The constitutive relations for the isotropic, nonpiezoelectric interlayer and matrix have the form

$$T_{rr}^{(i)} = c_{11}^{(i)}S_{rr}^{(i)} + c_{12}^{(i)}S_{\theta\theta}^{(i)} + c_{12}^{(i)}S_{zz}^{(i)} \tag{2.16}$$

$$T_{\theta\theta}^{(i)} = c_{12}^{(i)}S_{rr}^{(i)} + c_{11}^{(i)}S_{\theta\theta}^{(i)} + c_{12}^{(i)}S_{zz}^{(i)} \tag{2.17}$$

$$T_{zz}^{(i)} = c_{12}^{(i)}S_{rr}^{(i)} + c_{12}^{(i)}S_{\theta\theta}^{(i)} + c_{11}^{(i)}S_{zz}^{(i)} \tag{2.18}$$

$$T_{rz}^{(i)} = \frac{1}{2}(c_{11}^{(i)} - c_{12}^{(i)})S_{rz}^{(i)} \qquad (i = 2,3)\,. \tag{2.19}$$

Substitution of the constitutive relations and the strain-displacement relations into the equilibrium equations and the electrostatic equation gives the following governing equations in terms of displacements and electric field (i=1,2,3):

$$c_{11}^{(i)}\left(\frac{\partial^2 u^{(i)}}{\partial r^2} + \frac{1}{r}\frac{\partial u^{(i)}}{\partial r} - \frac{u^{(i)}}{r^2}\right) + (c_{13}^{(i)} + c_{44}^{(i)})\frac{\partial^2 w^{(i)}}{\partial r \partial z} + c_{44}^{(i)}\frac{\partial^2 u^{(i)}}{\partial z^2} - \\ - e_{31}^{(i)}\frac{\partial E_z^{(i)}}{\partial r} - e_{15}^{(i)}\frac{\partial E_r^{(i)}}{\partial z} = 0 \tag{2.20}$$

$$c_{44}^{(i)}\left(\frac{\partial^2 w^{(i)}}{\partial r^2} + \frac{1}{r}\frac{\partial w^{(i)}}{\partial r}\right) + (c_{13}^{(i)} + c_{44}^{(i)})\left(\frac{\partial^2 u^{(i)}}{\partial r \partial z} + \frac{1}{r}\frac{\partial u^{(i)}}{\partial z}\right) + \\ + c_{33}^{(i)}\frac{\partial^2 w^{(i)}}{\partial z^2} - e_{33}^{(i)}\frac{\partial E_z^{(i)}}{\partial z} - e_{15}^{(i)}\left(\frac{\partial E_r^{(i)}}{\partial r} + \frac{E_r^{(i)}}{r}\right) = 0 \tag{2.21}$$

$$e_{15}^{(i)}\left(\frac{\partial^2 w^{(i)}}{\partial r^2} + \frac{1}{r}\frac{\partial w^{(i)}}{\partial r}\right) + (e_{31}^{(i)} + e_{15}^{(i)})\left(\frac{\partial^2 u^{(i)}}{\partial r \partial z} + \frac{1}{r}\frac{\partial u^{(i)}}{\partial z}\right) + \\ + e_{33}^{(i)}\frac{\partial^2 w^{(i)}}{\partial z^2} + e_{33}^{(i)}\frac{\partial E_z^{(i)}}{\partial z} + e_{11}^{(i)}\left(\frac{\partial E_r^{(i)}}{\partial r} + \frac{E_r^{(i)}}{r}\right) = 0 \tag{2.22}$$

For the ceramic rod (region 1), the governing equations for mechanical deformation and electric field are coupled. The equations are solved by introducing two displacement potential functions and one electrical potential function such that

$$u^{(1)}(r,z) = \frac{\partial U(r)}{\partial r}\cos\mu z \tag{2.23}$$

$$w^{(1)}(r,z) = -W(r)\sin\mu z \tag{2.24}$$

$$E_r^{(1)}(r,z) = \frac{\partial E(r)}{\partial r}\sin \mu z \tag{2.25}$$

$$E_z^{(1)}(r,z) = \mu E(r)\cos \mu z \tag{2.26}$$

where U, W and E are functions of r only.

In order to satisfy the equations of equilibrium and the electrostatic equation, the functions U, W and E must satisfy the equations

$$(c_{11}^{(1)}\nabla_1^2 - c_{44}^{(1)}\mu^2)U - (c_{44}^{(1)} + c_{13}^{(1)})\mu W - (e_{31}^{(1)} + e_{15}^{(1)})\mu E = 0 \tag{2.27}$$

$$(c_{44}^{(1)} + c_{13}^{(1)})\mu\nabla_1^2 U + (c_{44}^{(1)}\nabla_1^2 - c_{33}^{(1)}\mu^2)W + (e_{15}^{(1)}\nabla_1^2 - e_{33}^{(1)}\mu^2)E = 0 \tag{2.28}$$

$$(e_{31}^{(1)} + e_{15}^{(1)})\mu\nabla_1^2 U + (e_{15}^{(1)}\nabla_1^2 - e_{33}^{(1)}\mu^2)W - (\varepsilon_{11}^{(1)}\nabla_1^2 - \varepsilon_{33}^{(1)}\mu^2)E = 0 \tag{2.29}$$

where $\nabla_1^2 = \frac{\partial^2}{\partial r^2} + \frac{1}{r}\frac{\partial}{\partial r}$.

Equations (2.27), (2.28), and (2.29) can be further reduced into a higher order ordinary differential equation

$$(\tilde{P}_1\nabla_1^6 + \tilde{P}_2\nabla_1^4 + \tilde{P}_3\nabla_1^2 + \tilde{P}_4)\{U, W, E\} = 0 \tag{2.30}$$

where $\tilde{P}_1$, $\tilde{P}_2$, $\tilde{P}_3$, and $\tilde{P}_4$ are dependent on the material properties of the piezoelectric rod and are given in the Appendix.

The solutions of Eq. (2.30) for a solid rod are

$$U = A_1^{(1)}I_0(\alpha_1 r) + A_2^{(1)}I_0(\alpha_2 r) + A_3^{(1)}I_0(\alpha_3 r) \tag{2.31}$$

$$W = A_1^{(1)}\beta_1 I_0(\alpha_1 r) + A_2^{(1)}\beta_2 I_0(\alpha_2 r) + A_3^{(1)}\beta_3 I_0(\alpha_3 r) \tag{2.32}$$

$$E = A_1^{(1)}\gamma_1 I_0(\alpha_1 r) + A_2^{(1)}\gamma_2 I_0(\alpha_2 r) + A_3^{(1)}\gamma_3 I_0(\alpha_3 r) \tag{2.33}$$

where α_i are the roots of the equation

$$\tilde{P}_1\alpha_i^6 + \tilde{P}_2\alpha_i^4 + \tilde{P}_3\alpha_i^2 + \tilde{P}_4 = 0 \tag{2.34}$$

and the constants β_i and γ_i are given by

$$(c_{44}^{(1)} + c_{13}^{(1)})\mu\beta_i + (e_{31}^{(1)} + e_{15}^{(1)})\mu\gamma_i = (c_{11}^{(1)}\alpha_i^2 - \mu^2 c_{44}^{(1)}) \tag{2.35}$$

$$(c_{44}^{(1)}\alpha_i^2 - \mu^2 c_{33}^{(1)})\beta_i + (e_{15}^{(1)}\alpha_i^2 - \mu^2 e_{33}^{(1)})\gamma_i = -(c_{44}^{(1)} + c_{13}^{(1)})\mu\alpha_i^2 . \tag{2.36}$$

The structure of the solutions of Eqs. (2.31), (2.32), and (2.33) depends on the nature of the value of α_i^2, and hence depends on the values of the material properties. For a PZT-5H rod (Morgan Matroc Inc., 1989), α_2^2 and α_3^2 are complex conjugates. Because the displacements and stresses are real, the functions *U*, *W* and *E* are chosen in the form

$$U = A_1^{(1)} I_0(a_1 r) + A_2^{(1)}\,\mathrm{Re}\left[I_0(a_2 r)\right] + A_3^{(1)}\,\mathrm{Im}\left[I_0(a_2 r)\right] \tag{2.37}$$

$$W = A_1^{(1)} b_1 I_0(a_1 r) + A_2^{(1)}\,\mathrm{Re}\left[b_2 I_0(a_2 r)\right] + A_3^{(1)}\,\mathrm{Im}\left[b_2 I_0(a_2 r)\right] \tag{2.38}$$

$$E = A_1^{(1)} g_1 I_0(a_1 r) + A_2^{(1)}\,\mathrm{Re}\left[g_2 I_0(a_2 r)\right] + A_3^{(1)}\,\mathrm{Im}\left[g_2 I_0(a_2 r)\right] \tag{2.39}$$

where I_0 is the zero-order modified Bessel function of the first kind.

The complementary displacements, stresses and dielectric displacements for the ceramic rod (*i*=1) are then obtained as

$$u_c^{(1)} = \sum_{n=1}^{\infty} \cos(m_n z)\left[A_{1n}^{(1)} h_{1n}^{(1)}(r) + A_{2n}^{(1)} h_{2n}^{(1)}(r) + A_{3n}^{(1)} h_{3n}^{(1)}(r)\right] \tag{2.40}$$

$$w_c^{(1)} = \sum_{n=1}^{\infty} \sin(m_n z)\left[A_{1n}^{(1)} h_{4n}^{(1)}(r) + A_{2n}^{(1)} h_{5n}^{(1)}(r) + A_{3n}^{(1)} h_{6n}^{(1)}(r)\right] \tag{2.41}$$

$$T_{rr\ c}^{(1)} = \sum_{n=1}^{\infty} \cos(m_n z)\left[A_{1n}^{(1)} h_{7n}^{(1)}(r) + A_{2n}^{(1)} h_{8n}^{(1)}(r) + A_{3n}^{(1)} h_{9n}^{(1)}(r)\right] \tag{2.42}$$

$$T_{qq\ c}^{(1)} = \sum_{n=1}^{\infty} \cos(m_n z)\left[A_{1n}^{(1)} h_{10n}^{(1)}(r) + A_{2n}^{(1)} h_{11n}^{(1)}(r) + A_{3n}^{(1)} h_{12n}^{(1)}(r)\right] \tag{2.43}$$

$$T_{zz\ c}^{(1)} = \sum_{n=1}^{\infty} \cos(m_n z)\left[A_{1n}^{(1)} h_{13n}^{(1)}(r) + A_{2n}^{(1)} h_{14n}^{(1)}(r) + A_{3n}^{(1)} h_{15n}^{(1)}(r)\right] \tag{2.44}$$

$$T_{rz\ c}^{(1)} = \sum_{n=1}^{\infty} \sin(m_n z)\left[A_{1n}^{(1)} h_{16n}^{(1)}(r) + A_{2n}^{(1)} h_{17n}^{(1)}(r) + A_{3n}^{(1)} h_{18n}^{(1)}(r)\right] \tag{2.45}$$

$$D_{r\ c}^{(1)} = \sum_{n=1}^{\infty} \sin(m_n z)\left[A_{1n}^{(1)} h_{19n}^{(1)}(r) + A_{2n}^{(1)} h_{20n}^{(1)}(r) + A_{3n}^{(1)} h_{21n}^{(1)}(r)\right] \tag{2.46}$$

$$D_{z\ c}^{(1)} = \sum_{n=1}^{\infty} \cos(m_n z)\left[A_{1n}^{(1)} h_{22n}^{(1)}(r) + A_{2n}^{(1)} h_{23n}^{(1)}(r) + A_{3n}^{(1)} h_{24n}^{(1)}(r)\right] \tag{2.47}$$

where $A_{1n}^{(1)}$, $A_{2n}^{(1)}$, and $A_{3n}^{(1)}$ are sets of constants and are to be determined from the boundary conditions. The m_n's are the eigenvalues and determined by the boundary conditions at $z = \pm l$,

$$m_n = \frac{np}{2l} \qquad (n = 1, 3, 5, \ldots). \tag{2.48}$$

The functions $h_{1n}^{(1)}(r)$ through $h_{24n}^{(1)}(r)$ are given in the Appendix.

For the isotropic and nonpiezoelectric interlayer (*i*=2) and matrix (*i*=3) the governing equations, Eqs. (2.20) through (2.22), reduce to

$$\nabla^2 u^{(i)} - \frac{u^{(i)}}{r^2} + \frac{c_{11}^{(i)} + c_{12}^{(i)}}{c_{11}^{(i)} - c_{12}^{(i)}} \frac{\partial}{\partial r}\left(\frac{\partial u^{(i)}}{\partial r} + \frac{u^{(i)}}{r} + \frac{\partial w^{(i)}}{\partial z}\right) = 0 \tag{2.49}$$

$$\nabla^2 w^{(i)} + \frac{c_{11}^{(i)} + c_{12}^{(i)}}{c_{11}^{(i)} - c_{12}^{(i)}} \frac{\partial}{\partial r}\left(\frac{\partial u^{(i)}}{\partial r} + \frac{u^{(i)}}{r} + \frac{\partial w^{(i)}}{\partial z}\right) = 0 \tag{2.50}$$

where $\nabla^2 = \frac{\partial^2}{\partial r^2} + \frac{1}{r}\frac{\partial}{\partial r} + \frac{\partial^2}{\partial z^2}$.

The complementary solution to Eqs. (2.49) and (2.50) is obtained by using Love's stress function provided the stress function $F^{(i)}(r,z)$ satisfies the equation,

$$\nabla^2\nabla^2 F^{(i)} = 0 \qquad (i = 2,3) \tag{2.51}$$

Thus, the complementary solution for the interlayer (i=2) and the matrix (i=3) are given by

$$u_c^{(i)} = \sum_{n=1}^{\infty} \cos(m_n z)\left[A_{1n}^{(i)} h_{1n}^{(i)}(r) + A_{3n}^{(i)} h_{2n}^{(i)}(r) + A_{2n}^{(i)} g_{1n}^{(i)}(r) + A_{4n}^{(i)} g_{2n}^{(i)}(r)\right] \tag{2.52}$$

$$w_c^{(i)} = \sum_{n=1}^{\infty} \sin(m_n z)\left[A_{1n}^{(i)} h_{3n}^{(i)}(r) + A_{3n}^{(i)} h_{4n}^{(i)}(r) + A_{2n}^{(i)} g_{3n}^{(i)}(r) + A_{4n}^{(i)} g_{4n}^{(i)}(r)\right] \tag{2.53}$$

$$T_{rr}^{(i)}{}_c = \sum_{n=1}^{\infty} \cos(m_n z)\left[A_{1n}^{(i)} h_{5n}^{(i)}(r) + A_{3n}^{(i)} h_{6n}^{(i)}(r) + A_{2n}^{(i)} g_{5n}^{(i)}(r) + A_{4n}^{(i)} g_{6n}^{(i)}(r)\right] \tag{2.54}$$

$$T_{qq}^{(i)}{}_c = \sum_{n=1}^{\infty} \cos(m_n z)\left[A_{1n}^{(i)} h_{7n}^{(i)}(r) + A_{3n}^{(i)} h_{8n}^{(i)}(r) + A_{2n}^{(i)} g_{7n}^{(i)}(r) + A_{4n}^{(i)} g_{8n}^{(i)}(r)\right] \tag{2.55}$$

$$T_{zz}^{(i)}{}_c = \sum_{n=1}^{\infty} \cos(m_n z)\left[A_{1n}^{(i)} h_{9n}^{(i)}(r) + A_{3n}^{(i)} h_{10n}^{(i)}(r) + A_{2n}^{(i)} g_{9n}^{(i)}(r) + A_{4n}^{(i)} g_{10n}^{(i)}(r)\right] \tag{2.56}$$

$$T_{rz}^{(i)}{}_c = \sum_{n=1}^{\infty} \sin(m_n z)\left[A_{1n}^{(i)} h_{11n}^{(i)}(r) + A_{3n}^{(i)} h_{12n}^{(i)}(r) + A_{2n}^{(i)} g_{11n}^{(i)}(r) + A_{4n}^{(i)} g_{12n}^{(i)}(r)\right] \tag{2.57}$$

$$T_{rz}^{(i)}{}_c = \sum_{n=1}^{\infty} \sin(m_n z)\left[A_{1n}^{(i)} h_{11n}^{(i)}(r) + A_{3n}^{(i)} h_{12n}^{(i)}(r) + A_{2n}^{(i)} g_{11n}^{(i)}(r) + A_{4n}^{(i)} g_{12n}^{(i)}(r)\right] \tag{2.58}$$

where $h_{1n}^{(i)}(r)$ through $h_{12n}^{(i)}(r)$ are expressions containing the material constants and the modified Bessel functions of the first kind, $I_0(m_n r)$ and $I_1(m_n r)$, and $g_{1n}^{(i)}(r)$ through $g_{12n}^{(i)}(r)$ are expressions containing the material constants and the modified Bessel functions of the second kind, $K_0(m_n r)$ and $K_1(m_n r)$. The functions $h_{1n}^{(i)}(r)$ through $h_{12n}^{(i)}(r)$ and $g_{1n}^{(i)}(r)$ through $g_{12n}^{(i)}(r)$ (i=2,3) are given in the Appendix. The constants $A_{1n}^{(i)}$, $A_{2n}^{(i)}$, $A_{3n}^{(i)}$ and $A_{4n}^{(i)}$ (i=2, 3) are to be determined by boundary conditions.

The final solution in each region is achieved by superposing the complementary solution and an additional solution corresponding to a generalized plane-strain state in order to satisfy all the boundary conditions. The generalized plane-strain solution for the ceramic rod (i=1) is given by

$$u_g^{(1)} = \xi^{(1)} r + \frac{\eta^{(1)}}{r} \tag{2.59}$$

$$w_g^{(1)} = \zeta^{(1)} z \tag{2.60}$$

$$T_{rr\ g}^{(1)} = c_{11}^{(1)}\left(x^{(1)} - \frac{h^{(1)}}{r^2}\right) + c_{12}^{(1)}\left(x^{(1)} + \frac{h^{(1)}}{r^2}\right) + c_{13}^{(1)} z^{(1)} - e_{31}^{(1)} E_{z\ g}^{(1)} \tag{2.61}$$

$$T_{qq\ g}^{(1)} = c_{12}^{(i)}\left(x^{(1)} - \frac{h^{(1)}}{r^2}\right) + c_{11}^{(1)}\left(x^{(1)} + \frac{h^{(1)}}{r^2}\right) + c_{13}^{(1)} z^{(1)} - e_{31}^{(1)} E_{z\ g}^{(1)} \tag{2.62}$$

$$T_{zz\ g}^{(1)} = 2c_{13}^{(1)}\xi^{(1)} + c_{33}^{(1)}\zeta^{(1)} - e_{33}^{(1)} E_{z\ g}^{(1)} \tag{2.63}$$

$$T_{rz\ g}^{(1)} = T_{qz\ g}^{(1)} = T_{rq\ g}^{(1)} = D_{r\ g}^{(1)} = 0. \tag{2.64}$$

The generalized plane strain solution for the interlayer (i=2) and matrix (i=3) is given by

$$u_g^{(i)} = \xi^{(i)} r + \frac{\eta^{(i)}}{r} \tag{2.65}$$

$$w_g^{(i)} = z^{(i)} z \tag{2.66}$$

$$T_{rr\ g}^{(i)} = c_{11}^{(i)}\left(x^{(i)} - \frac{h^{(i)}}{r^2}\right) + c_{12}^{(i)}\left(x^{(i)} + \frac{h^{(i)}}{r^2}\right) + c_{13}^{(i)} z^{(i)} \tag{2.67}$$

$$T_{qq\ g}^{(i)} = c_{12}^{(i)}\left(x^{(i)} - \frac{h^{(i)}}{r^2}\right) + c_{11}^{(i)}\left(x^{(i)} + \frac{h^{(i)}}{r^2}\right) + c_{13}^{(i)} z^{(i)} \tag{2.68}$$

$$T_{zz\ g}^{(i)} = 2c_{13}^{(i)}\xi^{(i)} + c_{33}^{(i)}\zeta^{(i)} \tag{2.69}$$

$$T_{rz\ g}^{(i)} = T_{\theta z\ g}^{(i)} = T_{r\theta\ g}^{(i)} = 0. \tag{2.70}$$

The constants $\xi^{(i)}$, $\eta^{(i)}$ and $z^{(i)}$ (i=1, 2, 3) are to be determined by the boundary conditions.

2.3 Boundary Conditions

The total stresses $T_{ij} = T_{ij_c} + T_{ij_g}$, displacements $u_i = u_{ic} + u_{ig}$ and the total electrical potential $f = f_c + f_g$ are required to satisfy the boundary conditions. The boundary conditions for the single embedded ceramic rod with interlayer shown in Fig. 2.2 are as follows:

(1) At $r = 0$, the solution is bounded.

(2) At $z = \pm l$, the normal traction is $p_z = T_{zz}^0$, the shear stresses constitute a system in equilibrium and the voltage applied is $\pm E_z^0 l$. These conditions are written as

$$T_{zz}^{(1)} = T_{zz}^{(2)} = T_{zz}^{(3)} = T_{zz}^0 \tag{2.71}$$

$$\int T_{rz}^{(i)} dr = 0 \tag{2.72}$$

$$\phi = \pm E_z^0 l . \tag{2.73}$$

(3) At $r = r_3$, the normal surface traction is $p_r = T_{rr}^0$ and the tangential traction is free, i.e.

$$T_{rr}^{(3)} = T_{rr}^0 \tag{2.74}$$

$$T_{rz}^{(3)} = 0. \tag{2.75}$$

For both the rod-interphase boundary and the interphase-matrix boundary, continuity of displacements and traction (perfect adhesion) is assumed. Also the ceramic rod-interphase boundary is treated as a dielectric-air boundary. Thus, the interface boundary conditions are expressed as

(4) At $r = r_1$

$$u^{(1)} = u^{(2)} \tag{2.76}$$

$$w^{(1)} = w^{(2)} \tag{2.77}$$

$$T_{rr}^{(1)} = T_{rr}^{(2)} \tag{2.78}$$

$$T_{rz}^{(1)} = T_{rz}^{(2)} \tag{2.79}$$

$$D_{rr}^{(1)} = 0\,. \tag{2.80}$$

(5) At $r = r_2$

$$u^{(2)} = u^{(3)} \tag{2.81}$$

$$w^{(2)} = w^{(3)} \tag{2.82}$$

$$T_{rr}^{(2)} = T_{rr}^{(3)} \tag{2.83}$$

$$T_{rz}^{(2)} = T_{rz}^{(3)}\,. \tag{2.84}$$

Application of the boundary conditions at $r = 0$ yields

$$\eta^{(1)} = 0 \tag{2.85}$$

The remaining boundary conditions generate two systems of linear equations which determine the unknown constants $\xi^{(1)}$, $\xi^{(2)}$, $\xi^{(3)}$, $\eta^{(2)}$, $\eta^{(3)}$, $z^{(1)}$, $z^{(2)}$, $z^{(3)}$, $A_{1n}^{(1)}$, $A_{2n}^{(2)}$, $A_{3n}^{(2)}$ and $A_{1n}^{(i)}$, $A_{2n}^{(i)}$, $A_{3n}^{(i)}$, $A_{4n}^{(i)}$ (i=2, 3).

2.4 Static Performance of Piezocomposites: The Local Displacement Field

In general, the piezoceramic and polymer in a 1-3 piezocomposite will have different deformations when the composite is subjected to an external electrical or mechanical stimulus. These deformations are dependent on the relative compliance of the ceramic and the polymer matrix and the interface between them. The local deformation also determines the effective behavior of the composite. The composite cylinder model developed is used to simulate the local deformations of a 1-3 piezocomposite driven by an external electric field.

Consider a 1-3 piezocomposite subjected to an electric field in the form of

$$p_i(\Omega) = 0 \tag{2.86}$$

$$\phi(\pm l) = \pm E_z^0 l = \pm\frac{V}{2} \tag{2.87}$$

where V is the voltage applied to the ends of the composite cylinder. Using the solution method outlined above, predictions were made of the static displacements of a single-rod piezoelectric composite assuming the PZT-5H properties listed in Table 2.1 (Morgan Matroc Inc., 1989). Geometric parameters are $r_1 = 0.375$ mm, $r_2 = 0.475$ mm, $r_3 = 3.0$ mm and $l = 5.0$ mm. The voltage applied to the ends of the composite cylinder is 70 V.

Table 2.1. Elastic and piezoelectric properties of PZT-5H rods .

Property	PZT-5H	Property	PZT-5H
$c_{11}^{(1)}$ (GPa)	126	$e_{31}^{(1)}$ (C/m^2)	–6.55
$c_{12}^{(1)}$ (GPa)	79.5	$e_{33}^{(1)}$ (C/m^2)	23.3
$c_{13}^{(1)}$ (GPa)	84.1	$e_{15}^{(1)}$ (C/m^2)	17.0
$c_{33}^{(1)}$ (GPa)	117	$d_{31}^{(1)}$ (10^{-12} m/V)	–274
$c_{44}^{(1)}$ (GPa)	23.0	$d_{33}^{(1)}$ (10^{-12} m/V)	593
$\varepsilon_{33}^{S\,(1)}$ (10^{-8} F/m)	1.30	$d_h^{(1)}$ (10^{-12} m/V)	45
$\varepsilon_{11}^{S\,(1)}$ (10^{-8} F/m)	1.50	$\varepsilon_{33}^{T\,(1)}$ (10^{-8} F/m)	3.01

2.4.1 Comparison with simple models

The axial displacement at $z = l$ of the piezocomposite cylinder is first calculated for the case of no interlayer. Displacement values are compared with those predicted by simple plane-strain models and are plotted as a function of radial distance in Fig. 2.3. The displacement profile obtained according to the simple models is uniform because all of the simple models (Haun and Newnham, 1986; Chan and Unsworth, 1989; Jensen 1991) assume uniform deformation in each constituent and give the same prediction of the effective composite piezoelectric constant, $\bar{d}_{33}$, which is expressed as

$$\bar{d}_{33} = \frac{v_f d_{33}^{(1)} s_{33}^{(3)}}{v_f s_{33}^{(3)} + (1 - v_f) s_{33}^{(1)}} \tag{2.88}$$

where v_f is the volume fraction of piezoelectric ceramic rods and $s_{pq}^{(i)}$ are elastic compliance constants for each phase.

When a 1-3 piezocomposite in these simple models is subjected to uniform axial electric field (E_z) only, the axial strain is given by $\bar{S}_{zz} = \bar{d}_{33} E_z$ and the axial displacement is $w = \bar{S}_{zz} z$.

The present solution predicts a nonuniform displacement profile. The maximum displacement occurs in the rod and decreases rapidly with radial distance in the matrix. As the length of the rod, $2l$, approaches infinity, the solution approaches that of a generalized plane-strain model, such as the concentric cylinder model by Jensen (1991).

2.4.2 Influence of the interlayer properties

A parametric study was carried out to assess systematically the influence of the interlayer properties on the static displacement of the current 1-3 piezocomposite model.

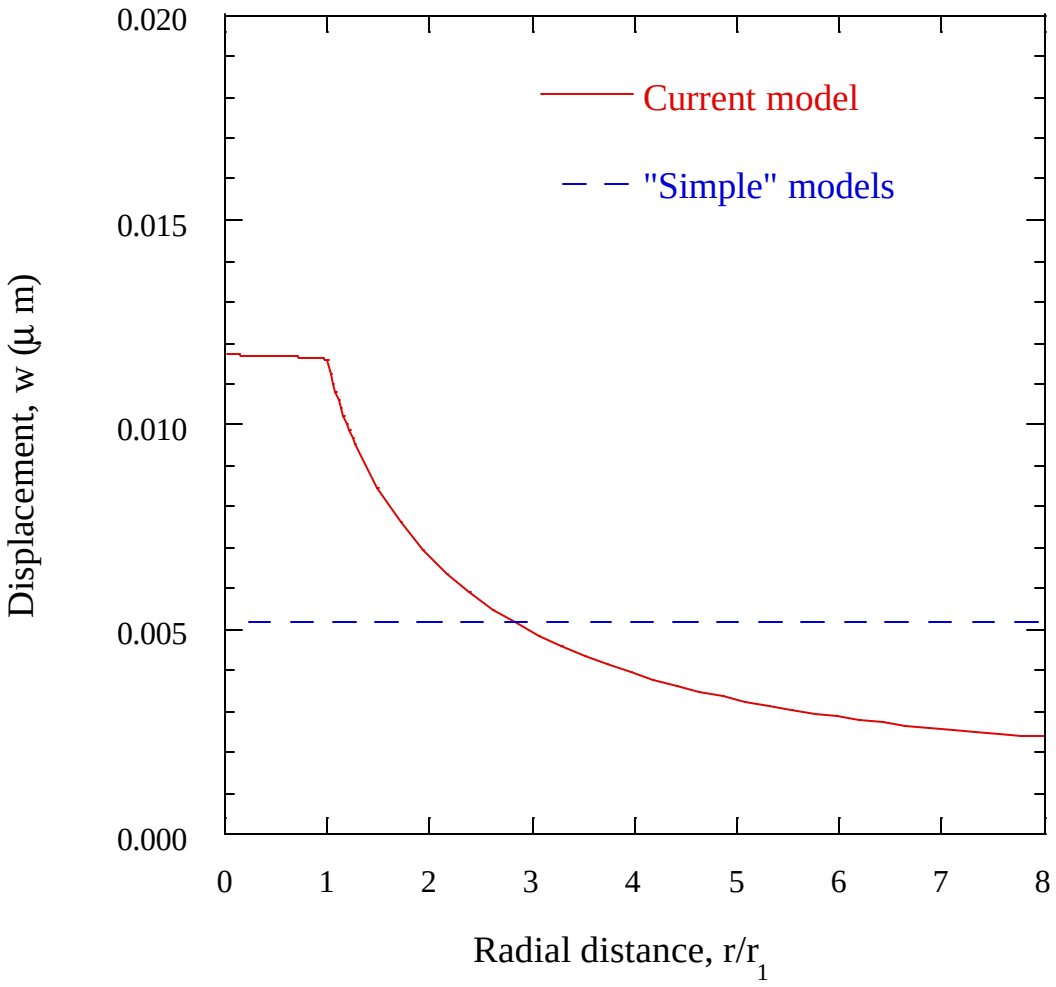

Fig. 2.3. Predictions using the current model and simple plane-strain model of axial displacement at $z = l$.

The interlayer was chosen to have an elastic stiffness either higher or lower than the neat matrix. The properties of the various interlayers used in the calculations are given in Table 2.2. The symbol, $Y^{(2)}$, in Table 2.2 represents the Young's modulus of the interlayer and $\nu^{(2)}$ is the Poisson's ratio. The Young's modulus and the Poisson's ratio of the surrounding matrix are kept as $Y^{(3)} = 2.101$ GPa and $n^{(3)} = 0.3$. Four different cases were considered. In Case 1 the interlayer and the matrix are the same. In Case 2 the interlayer is softer than the matrix while in Case 3 the interlayer is stiffer than the matrix. In Case 4 the interlayer modulus is one hundredth of the matrix modulus. The matrix is assumed to be Spurr epoxy and the properties were calculated using data from the manufacturer and room temperature tension tests.

Table 2.2. Elastic properties of interlayer used for parametric studies.

Property	Case 1	Case 2	Case 3	Case 4
$c_{11}^{(2)}$ (GPa)	2.827	0.565	14.135	0.0287
$c_{12}^{(2)}$ (GPa)	1.211	0.242	6.055	0.01211
$Y^{(2)}$ (GPa)	2.101	0.420	10.50	0.021
$n^{(2)}$	0.3	0.3	0.3	0.3

Axial displacement profiles at $z = l$ of the piezocomposite cylinder corresponding to interlayers with various elastic properties are shown in Fig. 2.4. In the calculation, the parameters r_1, r_2, r_3, l and V remain unchanged. It is seen in Fig. 2.4 that the axial displacement of the PZT rod is significantly influenced by introducing a compliant interlayer with a thickness of only 0.1 mm. The axial displacement of the PZT rod increases as the modulus of the interlayer decreases. The maximum displacement of the rod can be increased 64% by reducing the interlayer modulus to one hundredth of the matrix modulus.

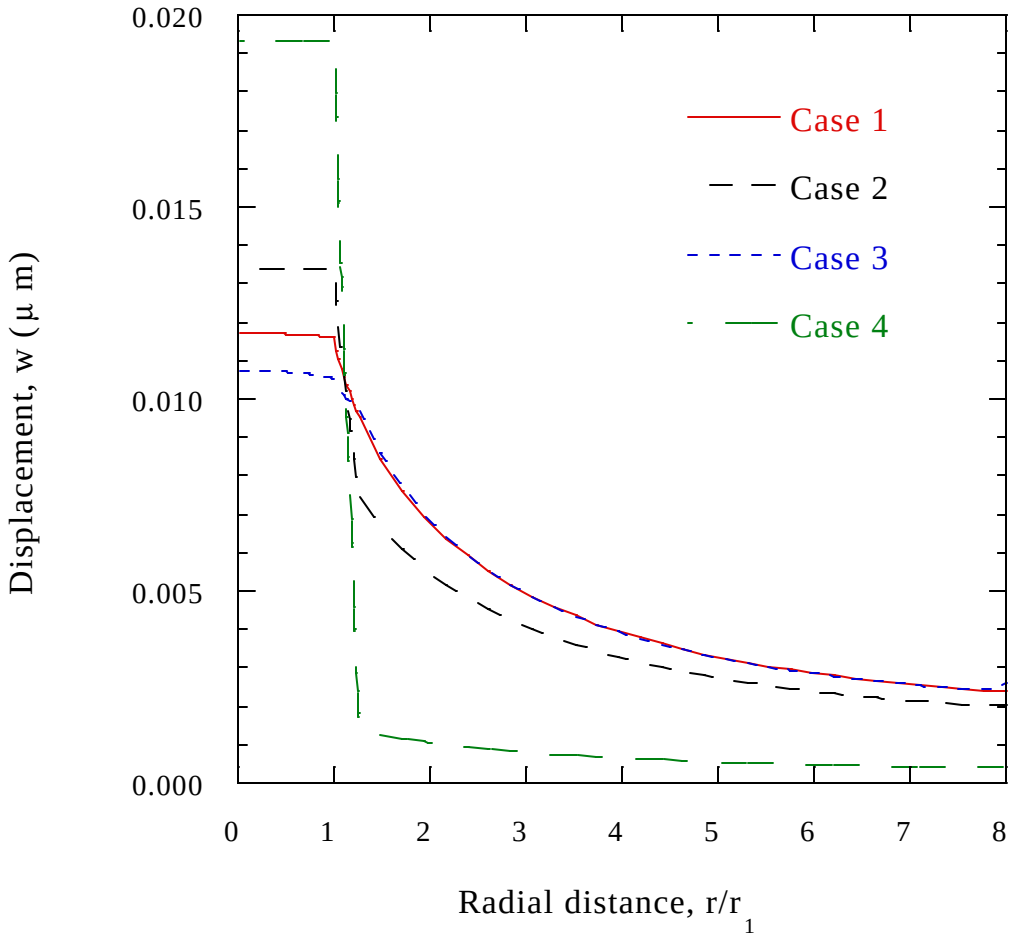

Fig. 2.4. Axial displacement profiles at $z = l$ for interlayers of varying moduli and thickness of 0.1 mm.

2.4.3 Influence of the matrix properties

The influence of the matrix was examined by keeping the interlayer properties constant while varying the matrix properties. Three different cases were considered. In Case 1 the interlayer and the matrix are the same. In Case 5 the matrix is softer than the interlayer while in Case 6 the matrix is stiffer than the interlayer. Properties of the interlayer are $Y^{(2)} = 2.101$ GPa and $n^{(2)} = 0.3$. The parameters r_1, r_2, r_3, l and V also remain unchanged. Properties of the matrix are tabulated in Table 2.3 and the results are shown in Fig. 2.5. The out-of-plane displacement of the single-rod piezocomposite depends highly on the modulus of the matrix. The trend of displacement variation shown in Fig. 2.5 agrees with that predicted by simple models, i.e., a composite with lower matrix modulus has a larger displacement.

Table 2.3. Elastic properties of matrix and interlayer used for parametric studies.

Property	Case 1	Case 5	Case 6
$c_{11}^{(3)}$ (GPa)	2.827	0.565	14.135
$c_{12}^{(3)}$ (GPa)	1.211	0.242	6.055
$Y^{(3)}$ (GPa)	2.101	0.420	10.50
$n^{(3)}$	0.3	0.3	0.3
$Y^{(2)}$ (GPa)	2.101	2.101	2.101
$n^{(2)}$	0.3	0.3	0.3

2.4.4 Influence of the interlayer thickness

The study of interaction between the polymer matrix, the interphase and the piezoelectric ceramic was further developed by investigating the influence of interlayer thickness on the displacement profile. Thickness variations were studied for both a soft interlayer (Case 2 in Table 2.2) and a stiff interlayer (Case 3 in Table 2.2).

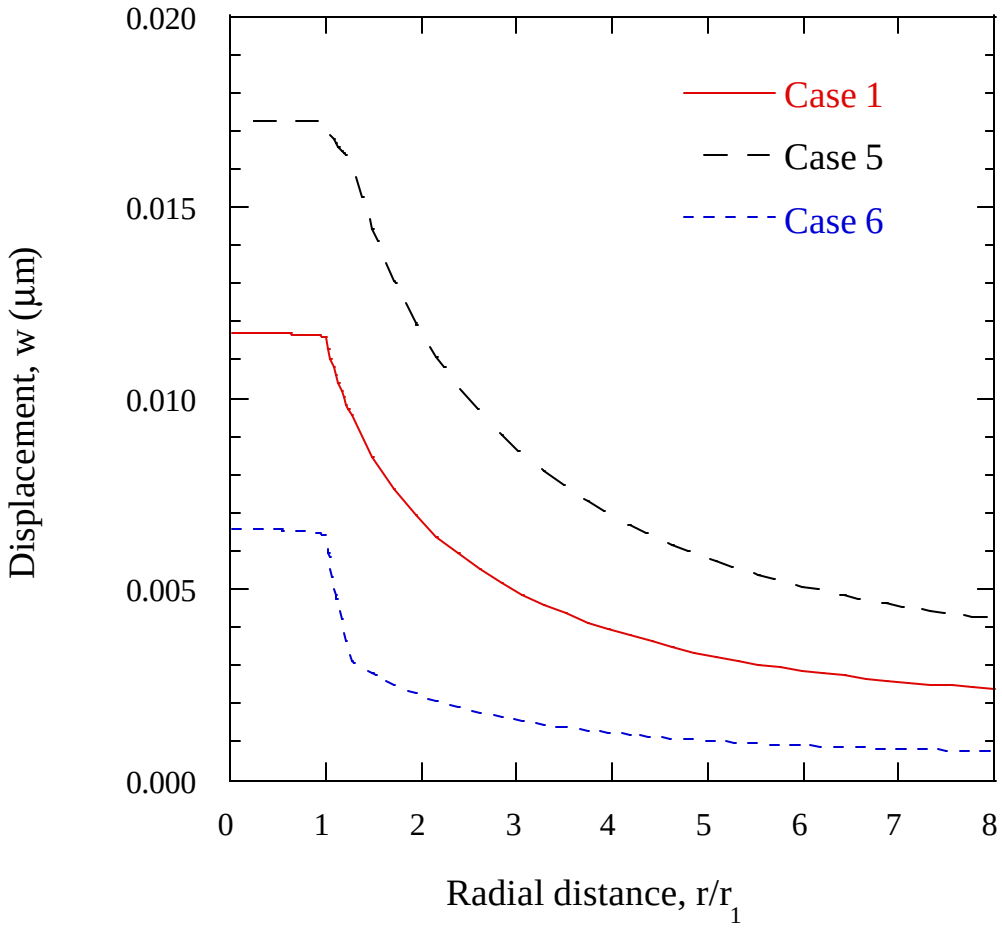

Fig. 2.5. Axial displacement profiles at $z = l$ for matrices of varying moduli (the interlayer thickness = 0.1 mm).

The thickness of the interlayer is defined as $r_2 - r_1$. The maximum axial displacement which is achieved at the center of the rod is plotted versus the interlayer thickness. Results are shown in Fig. 2.6 and Fig. 2.7. For a soft interlayer, the displacement increases as the interlayer thickness increases. For a stiff interlayer, the displacement decreases as the interlayer thickness increases. The results show that the influence of the interlayer becomes more significant as the thickness of the interlayer increases.

2.4.5 Influence of the ceramic rod volume fraction

The volume fraction of ceramic rods is an important parameter for designing and evaluating piezocomposites. In the current single-rod model, the volume fraction of rods is calculated by $v_f = (r_1/r_3)^2$. The effect of increasing rod volume fraction is shown in Fig. 2.8 where maximum axial displacement is plotted as a function of v_f. Interlayer and matrix parameters used in the calculation correspond to Case 2 in Table 2.2. As the volume fraction of rods increases, the maximum displacement also increases.

2.5 Effective Properties of Piezocomposites

Consider the overall behavior of the 1-3 piezocomposite shown in Fig. 2.1 exhibiting transverse isotropy. The constitutive relations between the average field variables ($\langle T_{ij} \rangle$, $\langle E_i \rangle$) and ($\langle S_{ij} \rangle$, $\langle D_i \rangle$) are described by means of the effective properties such that

$$\begin{Bmatrix} \langle D_1 \rangle \\ \langle D_2 \rangle \\ \langle D_3 \rangle \end{Bmatrix} = \begin{bmatrix} 0 & 0 & 0 & 0 & \bar{d}_{15} & 0 \\ 0 & 0 & 0 & \bar{d}_{15} & 0 & 0 \\ \bar{d}_{31} & \bar{d}_{31} & \bar{d}_{33} & 0 & 0 & 0 \end{bmatrix} \begin{Bmatrix} \langle T_{11} \rangle \\ \langle T_{22} \rangle \\ \langle T_{33} \rangle \\ \langle T_{23} \rangle \\ \langle T_{13} \rangle \\ \langle T_{12} \rangle \end{Bmatrix} + \begin{bmatrix} \bar{e}_{11}^T & 0 & 0 \\ 0 & \bar{e}_{11}^T & 0 \\ 0 & 0 & \bar{e}_{33}^T \end{bmatrix} \begin{Bmatrix} \langle E_1 \rangle \\ \langle E_2 \rangle \\ \langle E_3 \rangle \end{Bmatrix} \tag{2.89}$$

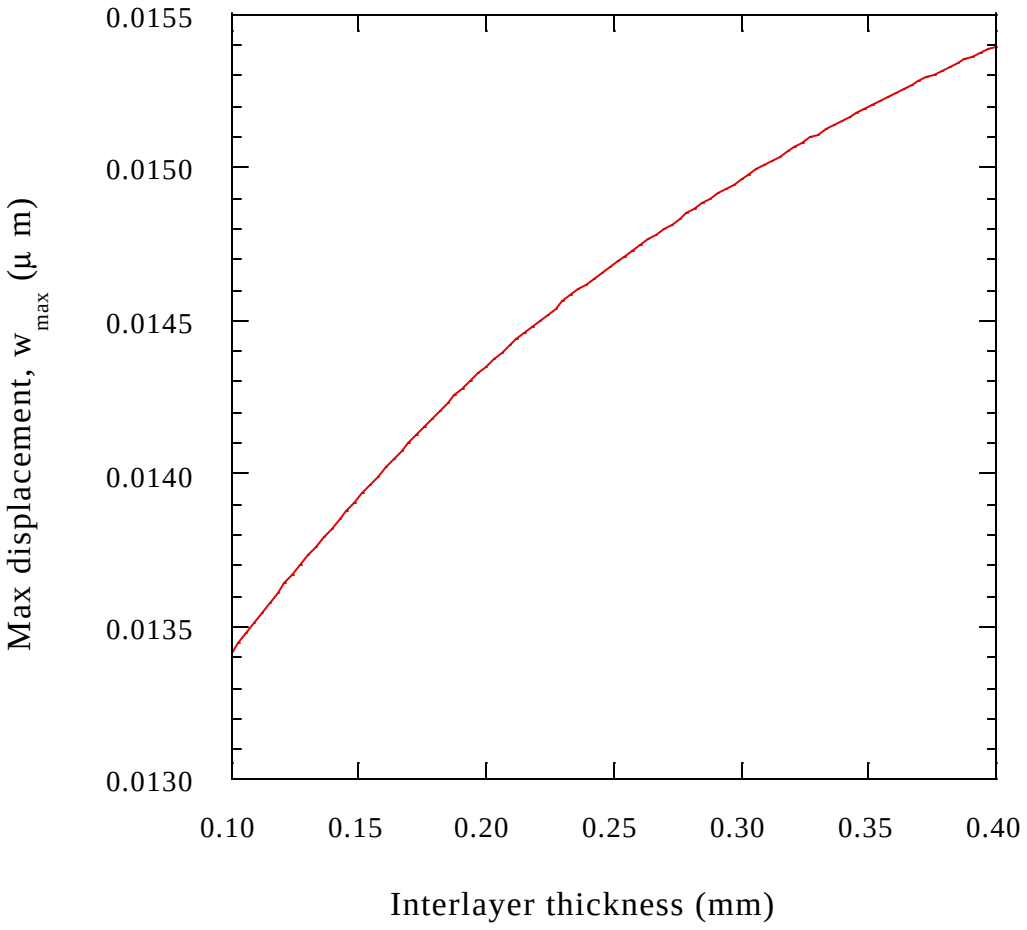

Fig. 2.6. Variation of the maximum axial rod displacement with interlayer thickness, for a soft interlayer ($Y^{(2)} = Y^{(3)}/5$).

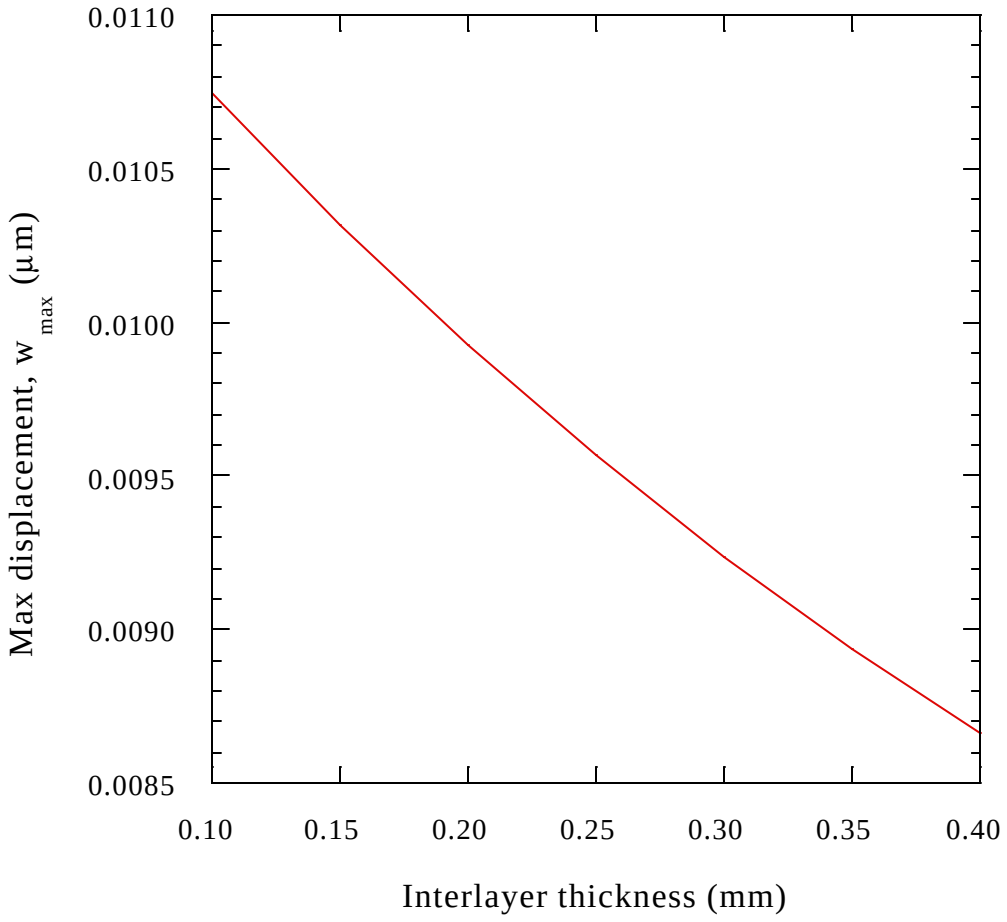

Fig. 2.7. Variation of the maximum axial rod displacement with interlayer thickness, for a stiff interlayer ($Y^{(2)} = 5Y^{(3)}$).

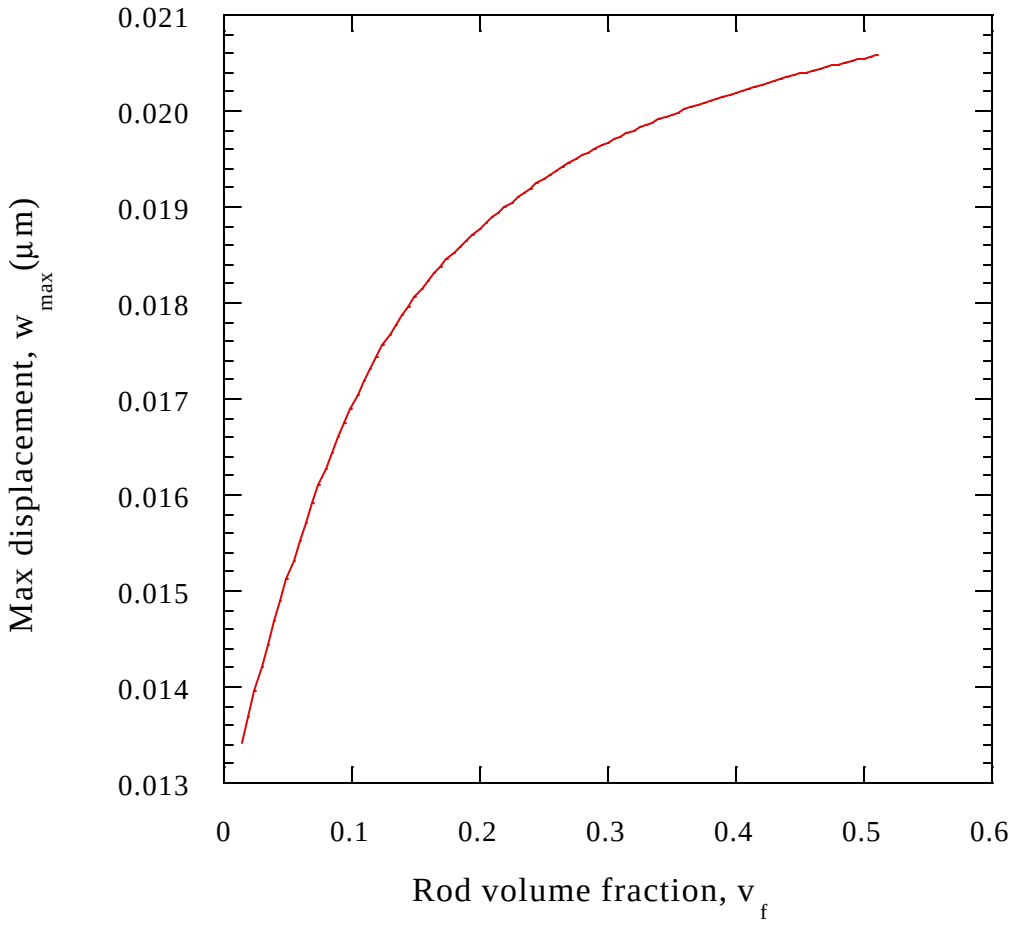

Fig. 2.8. Variation of the maximum axial rod displacement with volume fraction of PZT rods.

$$\begin{Bmatrix} \langle S_{11} \rangle \\ \langle S_{22} \rangle \\ \langle S_{33} \rangle \\ \langle S_{23} \rangle \\ \langle S_{13} \rangle \\ \langle S_{12} \rangle \end{Bmatrix} = \begin{bmatrix} \bar{s}_{11}^E & \bar{s}_{12}^E & \bar{s}_{13}^E & 0 & 0 & 0 \\ \bar{s}_{12}^E & \bar{s}_{11}^E & \bar{s}_{13}^E & 0 & 0 & 0 \\ \bar{s}_{13}^E & \bar{s}_{13}^E & \bar{s}_{33}^E & 0 & 0 & 0 \\ 0 & 0 & 0 & \bar{s}_{44}^E & 0 & 0 \\ 0 & 0 & 0 & 0 & \bar{s}_{44}^E & 0 \\ 0 & 0 & 0 & 0 & 0 & 2(\bar{s}_{11}^E - \bar{s}_{12}^E) \end{bmatrix} \begin{Bmatrix} \langle T_{11} \rangle \\ \langle T_{22} \rangle \\ \langle T_{33} \rangle \\ \langle T_{23} \rangle \\ \langle T_{13} \rangle \\ \langle T_{12} \rangle \end{Bmatrix} + \begin{bmatrix} 0 & 0 & \bar{d}_{31} \\ 0 & 0 & \bar{d}_{31} \\ 0 & 0 & \bar{d}_{33} \\ 0 & \bar{d}_{15} & 0 \\ \bar{d}_{15} & 0 & 0 \\ 0 & 0 & 0 \end{bmatrix} \begin{Bmatrix} \langle E_1 \rangle \\ \langle E_2 \rangle \\ \langle E_3 \rangle \end{Bmatrix} \quad (2.90)$$

where $\langle \bullet \rangle$ represents volume average and an over bar denotes an effective property for the piezocomposite.

2.5.1 Effective piezoelectric constants $\bar{d}_{33}$ and $\bar{d}_{31}$

In order to determine $\bar{d}_{33}$, one can impose the following boundary conditions on the piezocomposite

$$p_z(\pm l) = T_{zz}^0 \quad (2.91)$$

$$p_r(r_3) = 0 \quad (2.92)$$

$$\phi(\Omega) = 0 \quad (2.93)$$

which correspond to axial loading along the x_3 axis of the composite and no external electric field applied. The volume average of the resulting dielectric displacement in the composite cylinder element shown in Fig. 2.2 is calculated as

$$\langle D_z^{(1)} \rangle = \langle d_{31} T_{rr}^{(1)} \rangle + \langle d_{31} T_{qq}^{(1)} \rangle + \langle d_{33} T_{zz}^{(1)} \rangle + \langle e_{33}^T E_z^{(1)} \rangle . \quad (2.94)$$

The effective piezoelectric constant of the 1-3 piezocomposite $\bar{d}_{33}$ is then given by

$$\bar{d}_{33} = \frac{\langle D_z^{(1)} \rangle}{T_{zz}^0} . \quad (2.95)$$

To determine $\bar{d}_{31}$, a radial stress is applied to the boundary of the piezocomposite such that

$$p_z(\pm l) = 0 \tag{2.96}$$

$$p_r(r_3) = T_{rr}^0 \tag{2.97}$$

$$\phi(\Omega) = 0 \tag{2.98}$$

The volume average of the dielectric displacement in the composite cylinder element is again of the form

$$\langle D_z^{(1)} \rangle = \langle d_{31} T_{rr}^{(1)} \rangle + \langle d_{31} T_{qq}^{(1)} \rangle + \langle d_{33} T_{zz}^{(1)} \rangle + \langle e_{33}^T E_z^{(1)} \rangle . \tag{2.99}$$

The effective piezoelectric constant $\bar{d}_{31}$ of the 1-3 piezocomposite is then given by

$$\bar{d}_{31} = \frac{\langle D_z^{(1)} \rangle}{2\, T_{rr}^0} . \tag{2.100}$$

2.5.2 Predictions of $\bar{d}_{33}$ and $\bar{d}_{31}$

The piezoelectric charge constants $\bar{d}_{33}$ and $\bar{d}_{31}$ are calculated using Eqs. (2.95) and (2.100). The constants $\bar{d}_{33}$ and $\bar{d}_{31}$ are plotted against the volume fraction of PZT rods in Fig. 2.9 for the case of no interlayer and fixed PZT rod aspect ratio, $2l/d$. Here d is diameter of the piezoceramic rod and $2l$ is length of the rod. Like the maximum static displacement, both $\bar{d}_{33}$ and $-\bar{d}_{31}$ increase with increasing rod volume fraction. Both $\bar{d}_{33}$ and $-\bar{d}_{31}$ are maximum for the pure ceramic when the rod volume fraction is unity. However, some properties of the composite, like the effective hydrostatic piezoelectric constant $\bar{d}_h = \bar{d}_{33} + 2\bar{d}_{31}$ discussed in Chapter 4, can be improved for the intermediate rod volume fraction region. The values of $\bar{d}_{33}$

and $-\bar{d}_{31}$ predicted by the simple generalized plane-strain model are also plotted in Fig. 2.9. These values are higher than that obtained from the current model.

It is shown in Fig. 2.10 and Fig. 2.11 the influence of the PZT rod aspect ratio on the effective piezoelectric constants $\bar{d}_{33}$ and $\bar{d}_{31}$ for the case of no interlayer. The values of $\bar{d}_{33}$ and $-\bar{d}_{31}$ increase with increasing aspect ratio, but there is a saturation of the effect for $2l/d > 500$. These saturated values of $\bar{d}_{33}$ and $\bar{d}_{31}$ approach the values predicted by the simple generalized plane-strain model. The influence of the interlayer modulus on the effective piezoelectric constants $\bar{d}_{33}$ and $\bar{d}_{31}$ is shown in Fig. 2.12 and Fig. 2.13 for an interlayer that is 0.1 mm thick. The effect of the interlayer modulus depends on rod volume fraction. For an interlayer with modulus lower than that of the matrix, $\bar{d}_{33}$ and $-\bar{d}_{31}$ decrease for low rod volume fraction and increase for high rod volume fraction ($v_f > 0.5$). For an interlayer with modulus slightly higher than the matrix the $\bar{d}_{33}$ and $-\bar{d}_{31}$ decrease for $0 < v_f < 0.6$. For a very compliant interlayer both $\bar{d}_{33}$ and $-\bar{d}_{31}$ decrease, but the hydrostatic piezoelectric constant $\bar{d}_h$ may increase, as will be discussed in detail in Chapter 4.

2.6 Discussion

Difficulties exist in manufacturing 1-3 piezocomposites with large $2l/d$ ratio. In practice, values of $2l/d$ are typically less than 25. Thus, 1-3 piezocomposites should be modeled as aligned short-fiber composites and not as continuous-fiber composites. In this chapter, a three-dimensional analytical model was developed for studying the local fields and effective behavior in 1-3 piezocomposites.

The results obtained using the current model demonstrate that the local out-of-plane displacements of the composite are highly dependent on the interaction between the polymer matrix, a thin interlayer, and the piezoelectric ceramic. In order to enhance the out-of-plane displacement, a passive matrix with small Young's modulus should be chosen. This result is

similar to that obtained from simple models. However, the overall stiffness of the composite is dependent on the matrix modulus, especially for lower volume fractions. By introducing a thin compliant interlayer, the out-of-plane displacement of the rod is greatly increased while the requirement for overall stiffness of the composite can still be satisfied. The interlayer essentially serves to couple or decouple the rods from the matrix, depending on the interlayer stiffness. Interlayer properties were also found to influence significantly the effective charge constants $\bar{d}_{33}$ and $\bar{d}_{31}$ for the piezocomposite. Thus, the interlayer can be tailored to optimize the properties and increase the sensitivity of 1-3 piezocomposites.

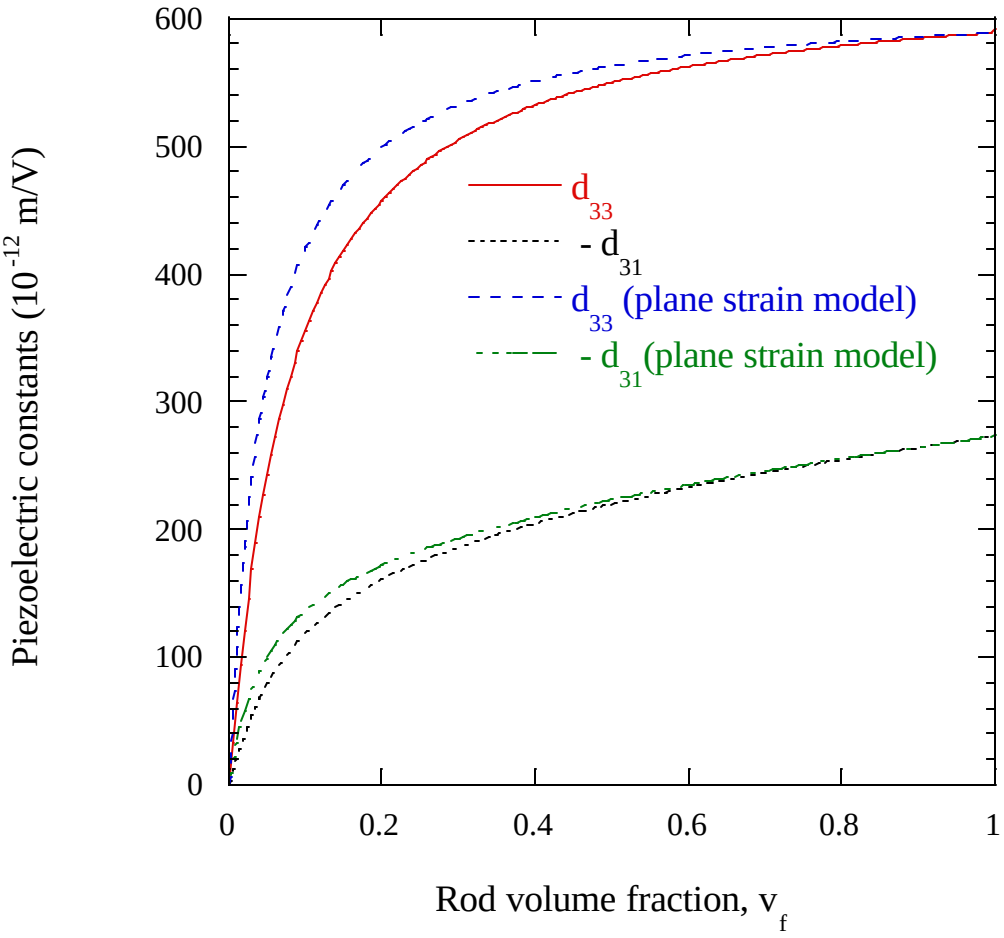

Fig. 2.9. Variation of effective piezoelectric constants with PZT rod volume fraction for the case of no interlayer.

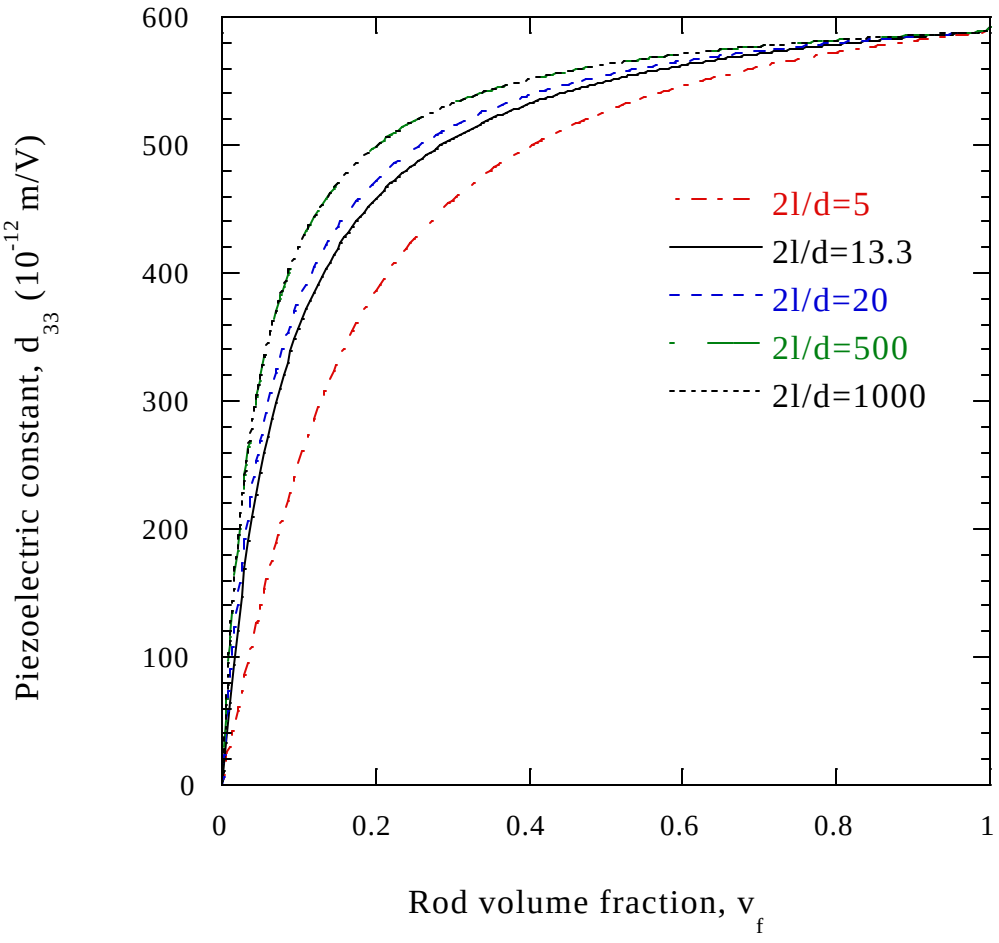

Fig. 2.10. Variation of $\bar{d}_{33}$ with PZT rod aspect ratio $2l/d$.

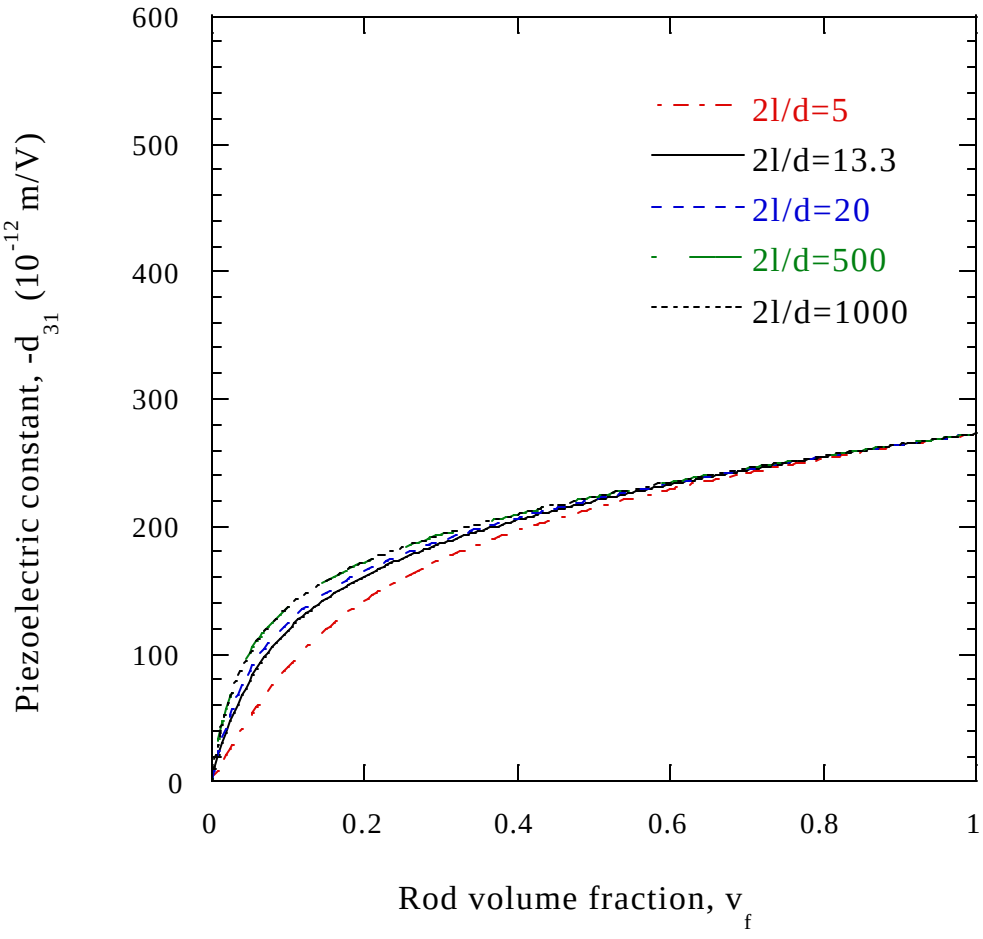

Fig. 2.11. Variation of $\bar{d}_{31}$ with PZT rod aspect ratio $2l/d$.

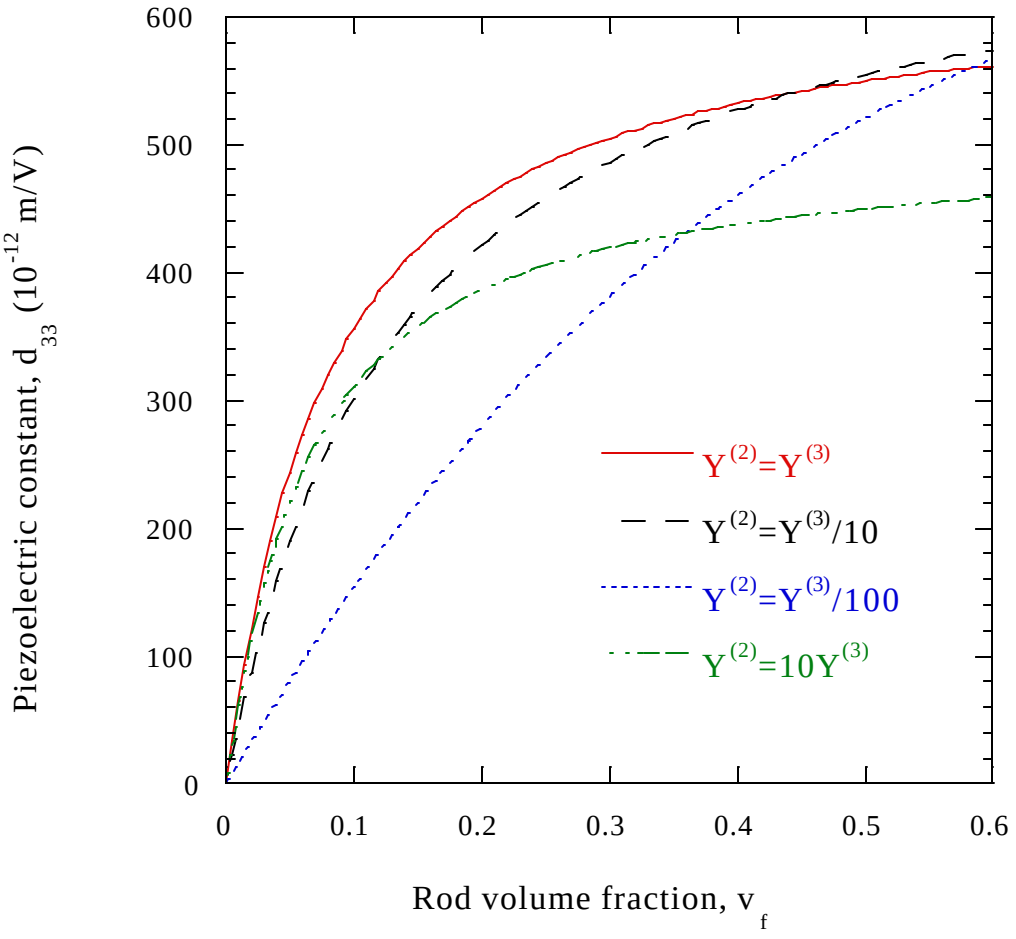

Fig. 2.12. Variation of $\bar{d}_{33}$ with interlayer modulus for an interlayer of 0.1 mm thickness.

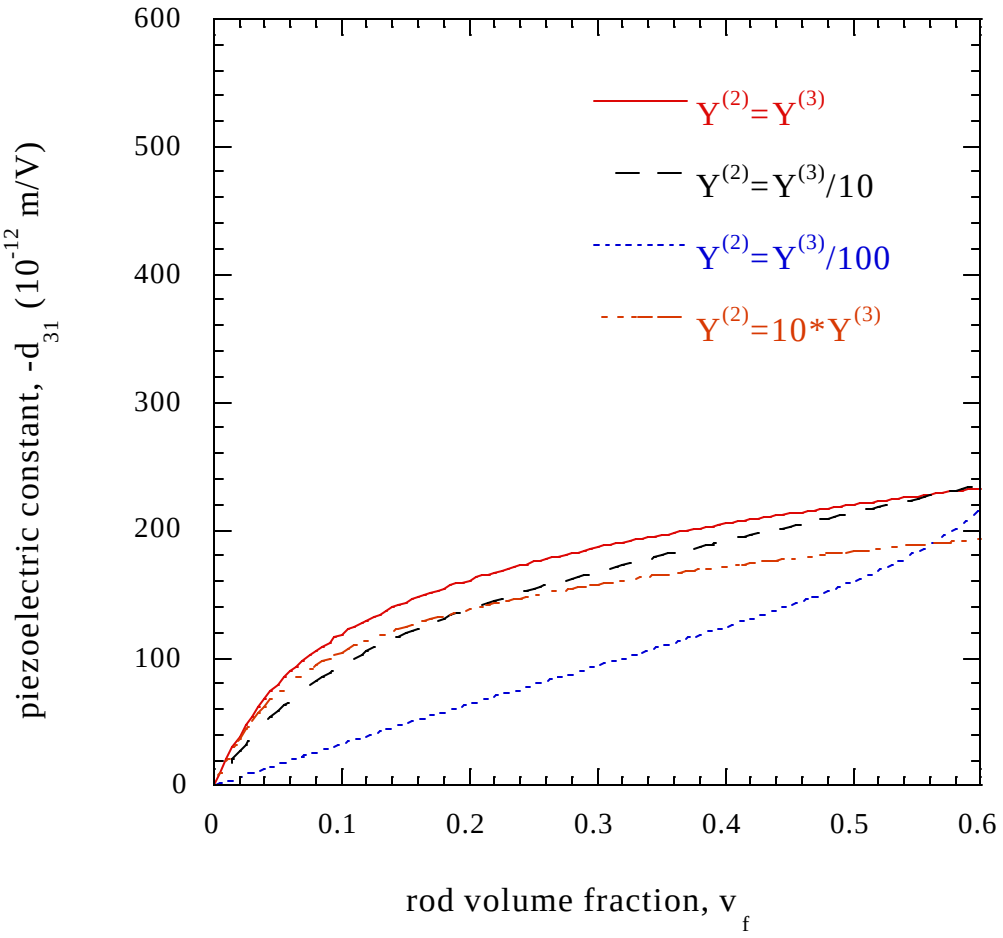

Fig. 2.13. Variation of $\bar{d}_{31}$ with interlayer modulus for an interlayer of 0.1 mm thickness.

3. IN-SITU DISPLACEMENT MEASUREMENTS OF PIEZOCOMPOSITES

3.1 Motivation

In Chapter 2, a composite cylinder model was used to predict the local deformations of a 1-3 piezocomposite driven by an external electric field. The local deformations were highly sensitive to the piezoelectric properties of the rod and the elastic properties of the polymer. The properties of the interface region between the rods and the matrix were also shown to have a significant effect on local behavior. The in-situ rod displacements induced by application of electric field (converse piezoelectric effect) are indicative of piezocomposite performance. For example, the average out-of-plane surface displacement can be correlated with the effective piezoelectric constant $\bar{d}_{33}$ for the composite.

In this chapter, the in-situ static displacements of a 1-3 piezocomposite are investigated experimentally using laser interferometry. Displacement profiles are measured for several different interface conditions and are correlated with the rod/polymer adhesion. Experimental results are also compared with predictions made by using the composite cylinder solutions derived in Chapter 2.

3.2 Micro-interferometric Method

Quantitative analysis of the local static deformations in 1-3 piezoceramic-polymer composites is a challenging problem. Since the deformations are small and nonuniform, the experimental technique must have an out-of-plane sensitivity of approximately 5 nm and a spatial resolution commensurate with the dimensions of the composite unit cell. Previous investigations by Sottos, Scott and McCullough (1991) and Ryan, Scott and Sottos (1990) have demonstrated the utility of heterodyne micro-interferometric methods for nondestructively measuring displacements in the interfacial regions of polymer matrix composites. Because a

long distance microscope with a high magnification is used, the interferometer probe has the capability to resolve small displacements in a very small region. The current investigation adapts this micro-interferometric technique for measuring in-situ surface displacements in 1-3 piezocomposites.

3.2.1 Apparatus

A scanning heterodyne micro-interferometer similar to that described in Sottos, Scott and McCullough (1991) is utilized to measure the surface displacements of 1-3 piezocomposite samples. A schematic diagram of the scanning heterodyne micro-interferometer is shown in Fig. 3.1. A single, linearly polarized light beam of wavelength 514.5 nm from an argon laser (Lexel Laser model 3500) is incident upon a 40 MHz acousto-optic modulator (AOM) producing two beams which are sent along different arms of the interferometer. The first beam, which follows path A in Fig. 3.1, is shifted in frequency by 40 MHz and is used as a reference beam. The second beam with the same frequency as the beam incident upon the AOM is directed along path B in Fig. 3.1 and is used to illuminate the sample surface. Hence, the sample serves as a mirror in this arm of the interferometer. The sample is mounted on a translation and rotation stage, such that only the outer edges of the back face of the sample are actually touching the fixture. This arrangement allows the sample to displace freely. The sample is manually adjusted for angular tilt when aligning the interferometer.

The combination of the polarizing beam splitter and the quarter-wave plate allows the sample to be illuminated at normal incidence without excessive light loss. The polarizing cube reflects vertically polarized light, and transmits horizontally polarized light. The vertical polarized light incident upon the cube is reflected through the quarter-wave plate, which circularly polarizes it. After reflection from the sample, the beam passes back

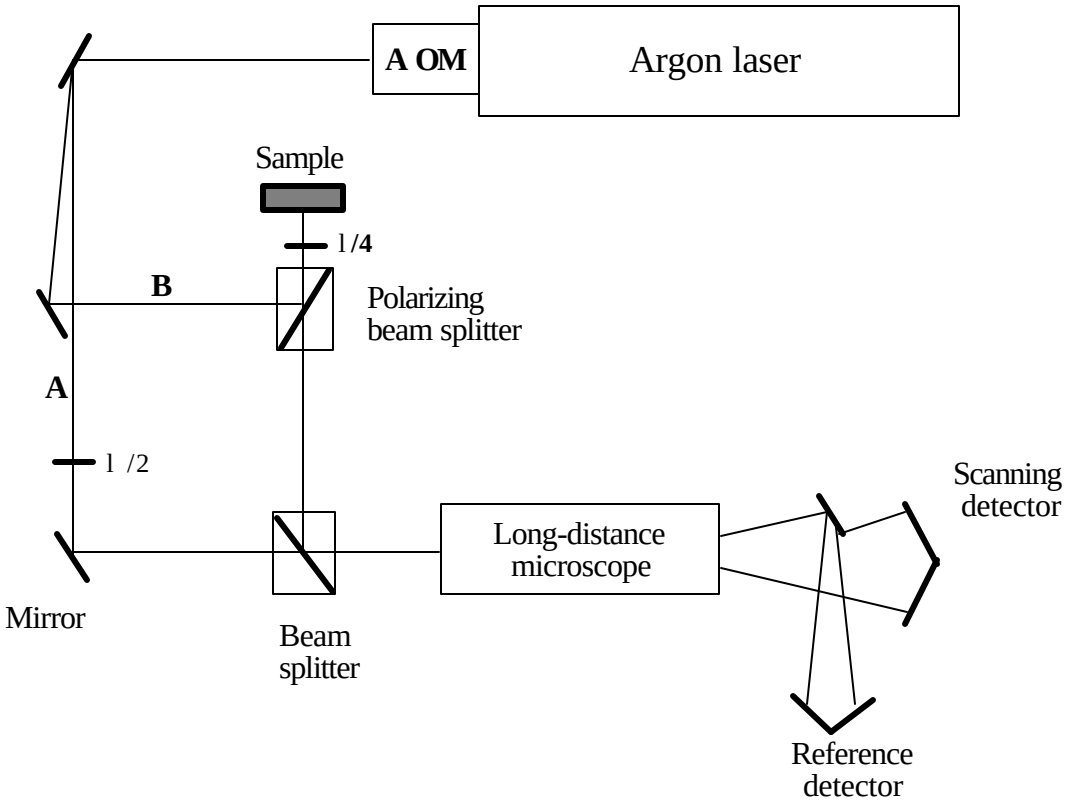

Fig. 3.1. Schematic of the scanning micro-interferometer.

through the quarter-wave plate, producing a horizontally polarized beam that passes through the polarizing cube toward the nonpolarizing beam splitter. The half-wave plate in the reference arm rotates the polarization of the modulated beam to match that of the beam from the sample arm. The two beams are recombined at the nonpolarizing beam splitter.

The combined beams then arrive at the primary lens of the long-distance microscope (Infinity model K2) placed before the eyepiece lens as shown in Fig. 3.1. An image (interferogram) of the sample surface is magnified onto the image plane with this long-distance microscope, where a scanning photodiode detector scans the magnified image. The large numerical aperture of the long distance microscope increases light gathering power and permits high-resolution imaging. Through the use of different lenses, magnifications from 1x to 100x are attainable. Depending on the magnification of the image, the in-plane resolution is limited either by the optical system or by the diameter of the detector window.

A dynamic image which travels at a 40 MHz beat signal across the image plane is formed because of the difference in frequency between the sample and reference beams. One corner of the image plane is reflected by a mirror onto a second photodetector. The signal at this stationary photodetector is used as a phase reference signal. The phase of the image signal is continuously compared with the phase of the reference signal. As a result, such dynamic disturbances as air turbulence, mechanical vibration, and thermal drift, that occur within the interferometer but away from the sample, do not affect the measurements.

The signal processing unit of the interferometer is shown in Fig. 3.2. The scanning photodiode detector is moved across the magnified sample image using two actuators

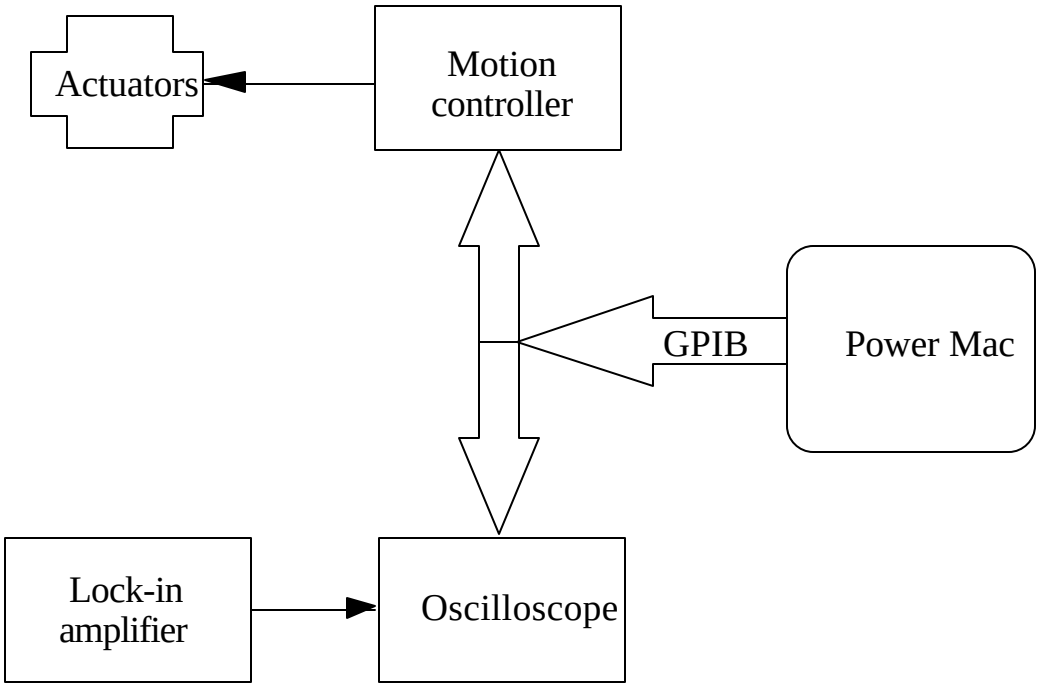

Fig. 3.2. Signal processing unit of the scanning interferometer.

which are perpendicular to each other. The actuators (Newport model 850B) are controlled by a microcomputer-controlled motion controller (Newport model PMC200P). A high-frequency lock-in amplifier (EG&G PARC model 5202) is used to measure the phase of the image signal. The output signal from the lock-in amplifier is digitized by a digital oscilloscope (Tektronix model TDS 420). Both the oscilloscope and the motion controller are interfaced with a central control unit, a Power Macintosh (Apple model 8100/80) via the IEEE-488.2 interface. The sweep rate of the oscilloscope is synchronized to the scanning of the photodetector by a Virtual Instrument (VI) written in LabVIEW (National Instruments) graphic language.

3.2.2 Principle of operation

For the calculation of the change of optical path length produced by out-of-plane motions, incidence wave is assumed to be plane, which is a reasonable assumption in the focal zone a Gaussian beam. With reference to Fig. 3.3, the formula which relates the change of optical path length $d\Delta$ to surface displacement $\mathbf{u}$ can be derived as (Monchalin et al., 1989)

$$\delta\Delta = (\mathbf{k}^i - \mathbf{k}^o) \bullet \mathbf{u} \tag{3.1}$$

Here $\mathbf{k}^i$ is the unit vector in the incident direction while $\mathbf{k}^o$ is that of the observation direction. For detecting out-of-plane displacement w, as in this study, the angle between $\mathbf{k}^i$ and $\mathbf{k}^o$ is 180^o. Thus Eq. (3.1) is simplified to

$$d\Delta = 2w \tag{3.2}$$

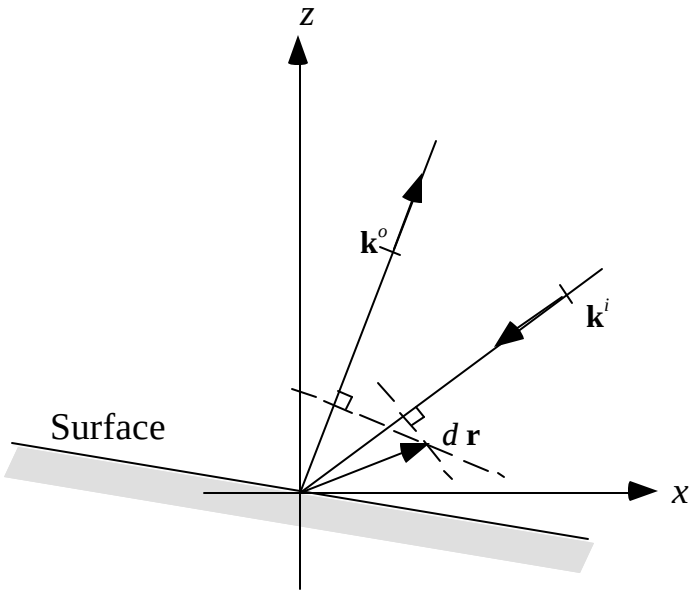

Fig. 3.3. Schematic of the displacement and optical path relation.

Let A_o denote the sample beam and A_r be the reference beam. On the image plane (xy plane) A_o and A_r are expressed as

$$A_o = a_o(x,y)\exp\left[i\left[2\pi f_o t + \psi_o(x,y)\right]\right] \tag{3.3}$$

$$A_r = a_r(x,y)\exp\left[i\left[2\pi f_r t + \psi_r(x,y)\right]\right] \tag{3.4}$$

where $a_o(x,y)$ and $a_r(x,y)$ are the amplitudes of A_o and A_r respectively.

The intensity of the superposed sample wave and reference wave, which is detected by the photodetector, is given as

$$I = a_o^2 + a_r^2 + 2a_o a_r \cos\left[2p(f_r - f_o)t + (y_r - y_o)\right]. \tag{3.5}$$

Here the frequency difference $f_r - f_o$ is set by the AOM at 40 MHz. The phase of the scanning detector output current, $\psi = \psi_r - \psi_o$, is measured with reference to the stationary detector. Any out-of-plane displacement of the sample surface produces a phase shift in the 40 MHz beat signal at the corresponding image plane. The relation between this phase shift $\Delta\psi$ and the change of optical path length $d\Delta$ due to out-of-plane displacement is

$$\Delta\psi = \frac{2\pi}{\lambda}\delta\Delta \tag{3.6}$$

where λ is the wavelength of the laser light. The displacement w can then be calculated from this phase shift. Obtaining a $\lambda/100 \approx 5$ nm sensitivity would require a phase measurement accuracy of approximately 7^o, which is guaranteed by the lock-in amplifier used.

3.3 Sample Preparation and Characterization

3.3.1 Sample fabrication

The interferometer is used to measure the static deformations resulting from activating a single PZT rod embedded in a polymer matrix. A schematic of the specimen is shown in Fig. 3.4. The piezoceramic (PZT) rods produced by Ceramic Processing Systems were 1 mm in diameter and poled in an oil bath under an electric field of 20 kV/cm. The axial piezoelectric constant was measured as $d_{33} = 420 \times 10^{-12}$ m/V . For the matrix, a Shell EPON-828 epoxy resin with a Shell DETA curing agent was chosen. The samples were fabricated by placing a PZT rod into the center of a mold which was then filled with epoxy. The samples were cured at room temperature for 7 days and post cured at 40 ^{o}C for 4 hours to raise the glass transition temperature of the epoxy.

The influence of a distinct interface region between the rod and the polymer was investigated by fabricating samples with several different interface conditions. In the first type (I), the rods were embedded with no special interface treatment or coating as described above. In the second type (II), a thin polymeric coating with a Young's modulus lower than that of the bulk matrix was applied to the rods prior to being embedded. Type III samples had an even lower modulus (almost rubber-like) coating applied to the rods. Finally for the fourth sample type (IV), the rods were treated with a silane coupling agent obtained from Fiber Materials Inc.

Spurr epoxy (Polysciences) was used for the compliant coatings (types II and III). Spurr epoxy is a four-component system. The modulus was varied by changing the concentration of the flexibilizer--diglycidyl ether of polypropylenglycol (DER) in the stoichiometric mix. Table 3.1 lists the various compositions of Spurr used in this study and the designation of each composition. Coatings were applied by dipping the rods in the epoxy and curing at 70 ^{o}C for 8 hours. To increase the thickness, a second layer of

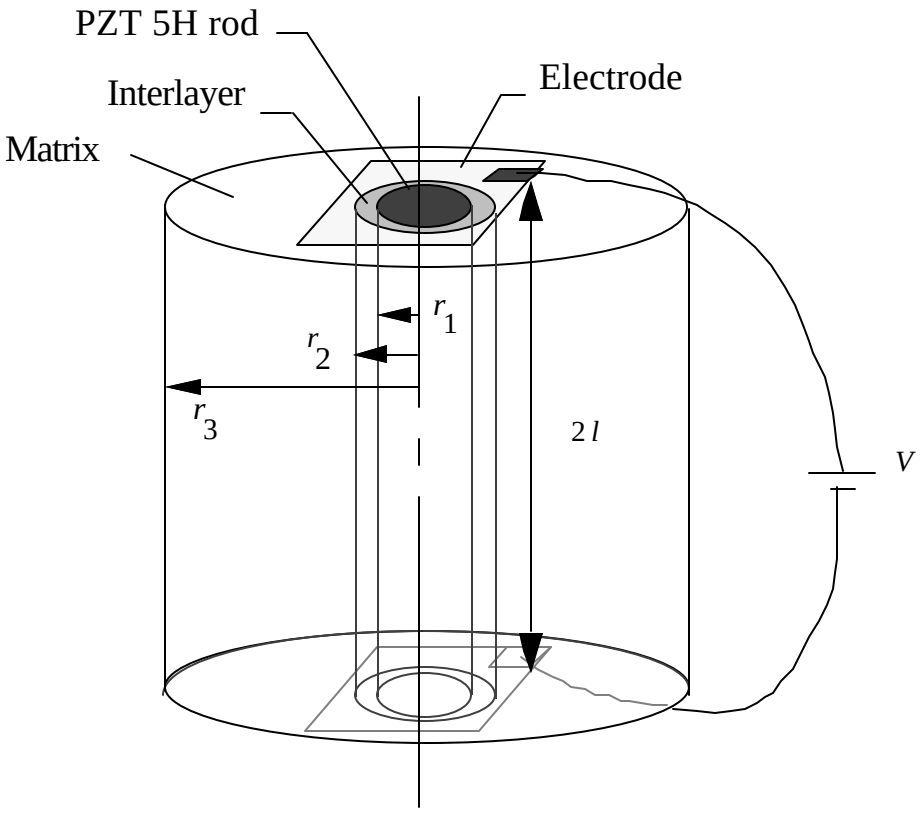

Fig. 3.4. Schematic of the sample for interferometric measurements.

coating was applied to the first layer. Properties of the coatings as measured by uniaxial tension tests are listed in Table 3.2.

Table 3.1. Spurr epoxy compositions.

Coating	VCD	DER	NSA	DMAE
Type I	10 g	6 g	26 g	0.4 g
Type II	10 g	9.1 g	26 g	0.4 g
Type III	10 g	19.6 g	26 g	0.4 g

Table 3.2. Properties of the Spurr epoxy coatings.

Coating	Young's modulus (GPa)
Type I	2.1
Type II	0.6
Type III	0.01

3.3.2 Interfacial adhesion

It is essential to have some measure of the interfacial bond strength between the coated PZT rods and the polymer matrix for the evaluation of mechanical response and the development of well-designed interfaces. Displacement measurements are sensitive to the PZT/polymer adhesion as well as the elastic properties of the coating. Although the literature abounds with studies of fiber/matrix adhesion in polymer composites, very little work has been carried out on piezoceramic/polymer adhesion.

A thin-section push-out test was adopted to measure the PZT rod/polymer interface strength (Li, Durkin and Sottos, 1994). This test, which has been used extensively to measure the in-situ interfacial shear strength in fibrous composites, is useful for evaluating the effects of coatings on debonding. A schematic of the thin-section push-out apparatus is shown in Fig. 3.5. Single rod samples as described in Section 3.3.1 were cut to a length of approximately 3.5 mm. Tests were conducted by applying an axial load to the rod using the punch, which was attached to an Instron testing machine. A constant cross-head displacement rate of 0.05 mm/sec was used for the tests. A typical load versus displacement curve is shown in Fig. 3.6. The maximum load corresponds to the point at which the rod debonded from the matrix. Using the maximum load, P_{max}, and the sample dimensions, one can calculate the average interfacial shear strength, t_0, expressed as

$$\tau_0 = \frac{P_{max}}{4\pi rl} \tag{3.7}$$

Although this simplified equation only calculates an average interfacial strength, it is useful for comparing adhesion changes due to the different interlayers or surface treatments used in this study. The effects of different coating types on interfacial shear strength are summarized in Table 3.3. The results show that the addition of a interlayer with lower elastic modulus has almost no effect on the average interfacial shear strength

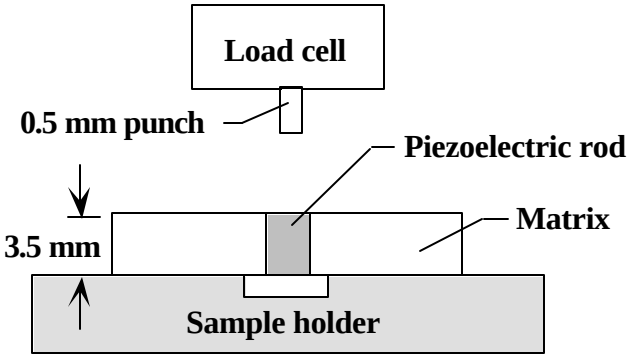

Fig. 3.5. Schematic of the thin-section push-out test.

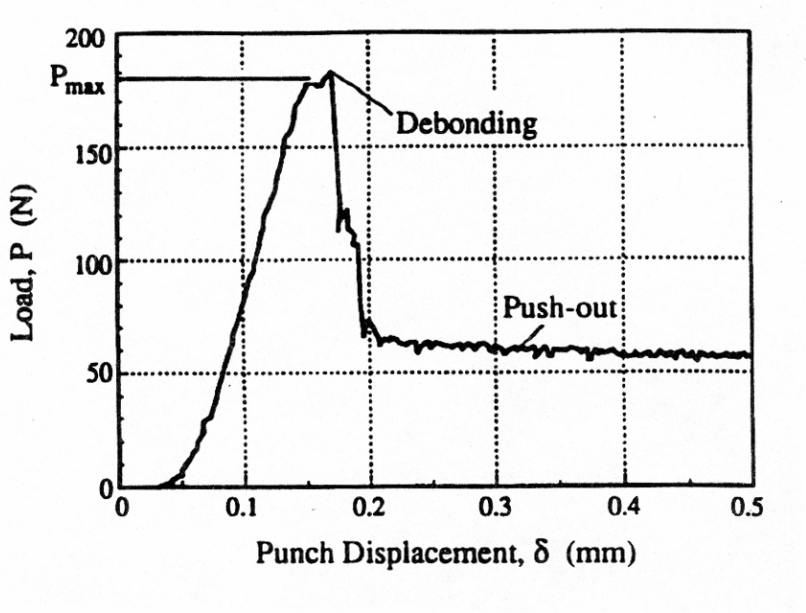

Fig. 3.6. A typical load-displacement curve for the push-out test.

at room temperature. The results also show that the interfacial shear strength is significantly increased by the silane coupling agent.

Table 3.3 Average interfacial shear strength.

Coating	Interfacial Shear Strength
Type I	17.3 MPa
Type II & Type III	18.7 MPa
Type IV	22.4 MPa

3.3.3 Surface preparation for interferometric measurement

For the interferometric experiments, single rod samples were cut to a length of 5 mm and the front face finely polished. Polishing of the face on which the laser probe measurements are made was critical to insure a flat surface free of scratches. After polishing, a thin gold coating was evaporated on the front surface of the sample to provide a highly reflective surface for the interferometric measurement as well as an electrode for applying the electric field. Silver paint was applied to the back surface of the sample to provide a second electrode.

3.4 Experimental Procedure and Results

The piezoceramic rod was actuated by applying a static voltage across the piezocomposite sample. Two types of displacement measurements are reported below. In the first type of measurement, maximum displacement is recorded as a function of time after actuation. In the second type of measurement, displacement profiles of the single-rod composite are obtained.

3.4.1 Maximum surface displacement

For the maximum displacement measurement, the scanning detector is fixed in the center of the PZT rod. An electric field is applied across the sample, which triggers the acquisition of the phase data as the sample responds. The phase change is then converted to displacement for that particular point. Measured displacements are plotted as a function of time for all four types of sample in Fig. 3.7. The applied voltage is also shown in this figure. The composite cylinder model discussed in Chapter 2 predicts that the maximum displacement will occur at the center of the ceramic rod. It can be seen in Fig. 3.7 that the displacement at the center of the PZT rod jumps rapidly in about 600 ms from zero to its stable value when the dc voltage is turned on. The displacements of the samples with a low-modulus interphase (types II and III) were higher than that of the untreated samples (type I). Because the adhesion between the Spurr epoxy coated rods is very similar to that of the untreated rods (see Table 3.3), the increase in displacement is due solely to the reduction in stiffness of the interlayer surrounding the rod. The samples treated with a silane coupling agent (type IV) had a lower displacement than the untreated samples (type I). This decrease in displacement may be attributed to the increase in adhesion between the silane treated rod and the surrounding matrix or to the formation of a stiffer interlayer near the rod due to a reaction between the silane coupling agent and the matrix during sample cure. The extent of reaction of the silane with the matrix is not well known and therefore makes it very difficult to assess the properties near the rod surface.

3.4.2 Surface displacement profile

Surface displacement profiles are obtained by scanning the detector in a radial path from the rod center. To measure the net displacements of the sample, one makes an initial scan of the surface before activation. The sample is then activated and a second scan is run. During each scan, phase data are continuously recorded and stored. Figure 3.8 is a typical plot of the raw data from the surface profiles before and after activation. Displacements are calculated by

subtracting the phase data of the initial scan lines from the final ones. All out-of-plane displacements are measured relative to the same reference point, which is at a distance at least 3 times the rod radius away from the rod center.

Figure 3.9 shows the measured displacement profiles along the radial direction of the samples for each interphase type. A nonuniform experimental displacement profile is observed with maximum displacement in the PZT rod region. The surface displacement decreases with radial distance in the matrix. The axial displacement of the PZT rod is significantly influenced by a thin compliant coating. The rod displacement increases as the modulus of the coating decreases. This observation is consistent with the results predicted theoretically. Although a thin compliant coating decouples the rod from the matrix and increases the rod displacement, it also increases the nonuniformity of the displacement profile across the composite. On the other hand, samples with silane coupling agent have smaller and more uniform surface displacements.

3.5 Discussion

A one to one comparison of theory and experiment is difficult because the mechanical properties of the interphase cured with silane coupling agent and the thicknesses of the coatings are unknown. However, trends in the variation of surface displacement profile due to changes in interphase properties can be assessed. Predictions of surface displacement profile were made by using the theoretical analysis derived in Chapter 2. Elastic properties for the PZT rod in Table 2.1 are used. The measured value of $d_{33} = 420 \times 10^{-12}$ m/V is used and the value of d_{31} is estimated to be $d_{31} = -198 \times 10^{-12}$ m/V. Material properties for EPON 828 epoxy are listed in Table 3.4. Geometric parameters are $r_1 = 0.5$ mm, $r_2 = 0.6$ mm, $r_3 = 3.0$ mm, and $l = 2.5$ mm. The displacement profiles for samples with different interphase modulus are shown in Fig. 3.10 for an applied dc voltage of 300V. These displacements are relative to, $r = 3r_1$, the point where the reference detector is located in the experiments. The variations of surface displacement profile due to changes in interphase properties as shown in Fig. 3.10 are in

good agreement with the experimentally observed trends for the untreated samples (type I) and samples with a low modulus interlayer (types II and III). The measured displacement profile for the silane coupling agent treated samples (type IV) is lower than the predicted displacement profile for samples with a high modulus interlayer as shown in Fig. 3.10. This decrease in the measured displacement may be attributed to the increase in adhesion between the silane treated rod and the surrounding matrix.

Table 3.4. Materials properties for EPON 828 epoxy.

$Y^{(3)}$ (GPa)	$\nu^{(3)}$
2.5	0.3

Micro-interferometric measurements as well as the theoretical predictions demonstrate that the out-of-plane displacements of the composite are highly dependent on the interaction between the polymer matrix, a thin interlayer and the piezoelectric ceramic. By introducing a thin compliant interlayer, the out-of-plane displacement of the rod is greatly increased while the requirement for overall stiffness of the composite can still be satisfied. The interlayer essentially serves to couple or decouple the rods from the matrix, depending on the interlayer stiffness. On the other hand a silane coupling agent can improve the interfacial adhesion and reduce the nonuniformity of the displacement profile in whole composite region. The measured displacement profile can also be used to estimate the effective piezoelectric constants $\bar{d}_{33}$ of the composite. For thin-section 1-3 piezocomposites, $\bar{d}_{33}$ can be calculated from the out-of-plane displacement as

$$\bar{d}_{33} = \frac{1}{\Omega}\int \frac{2w(x,y)}{V} d\Omega \tag{3.8}$$

where V is the voltage applied and the integral is over the area, Ω, measured on the surface of the composite sample.

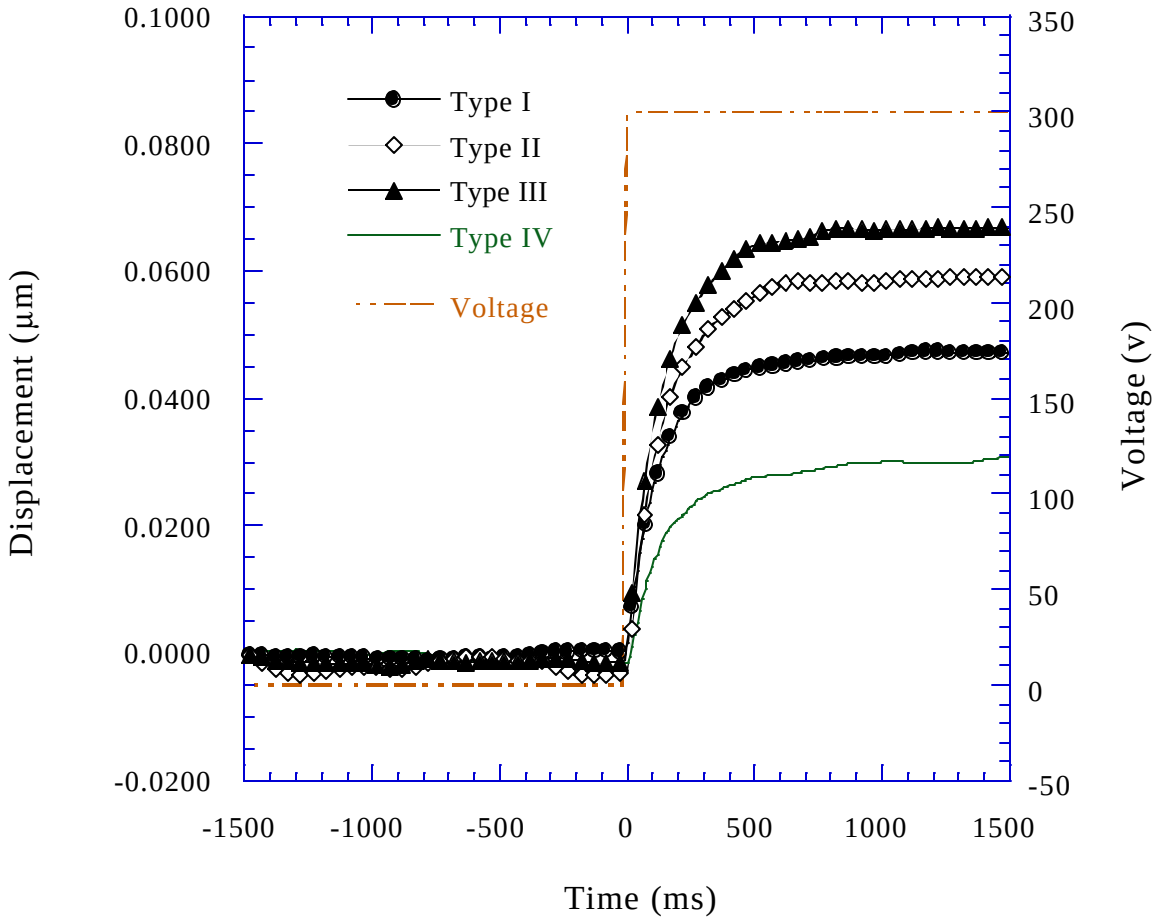

Fig. 3.7. Displacements measured at the center of the PZT rod.

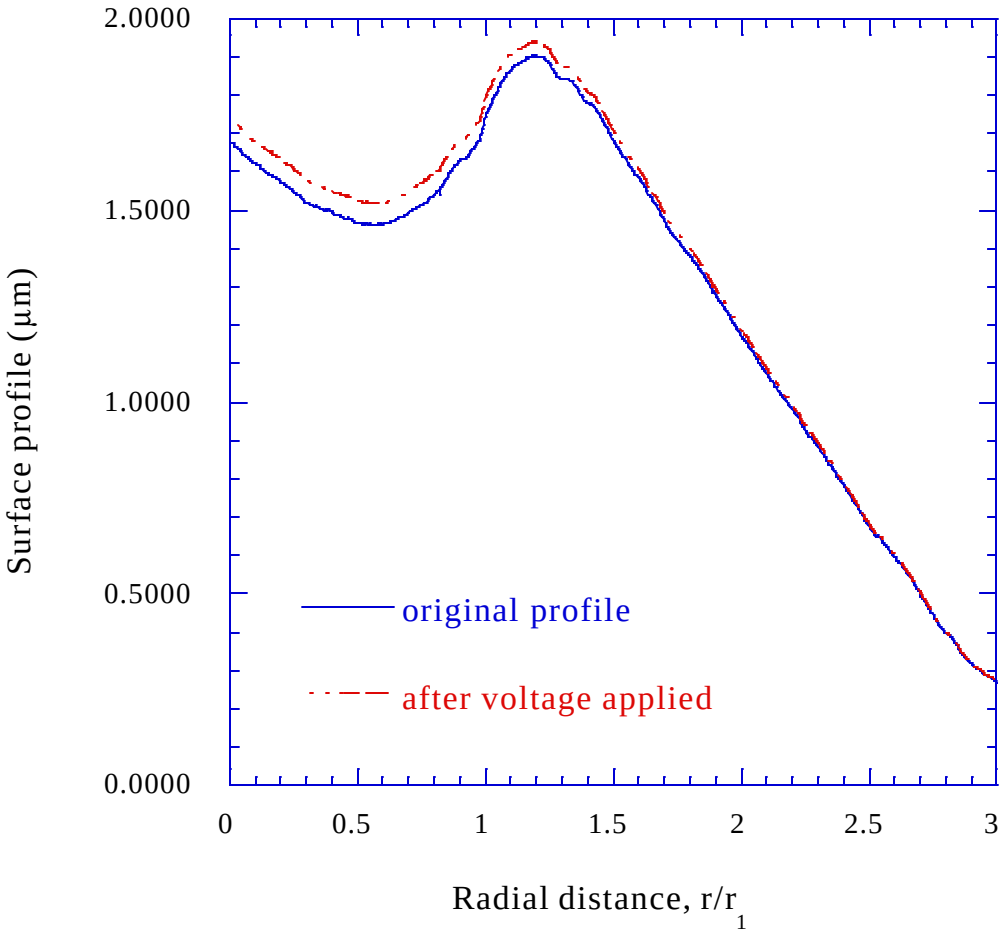

Fig. 3.8. Measured composite sample profiles.

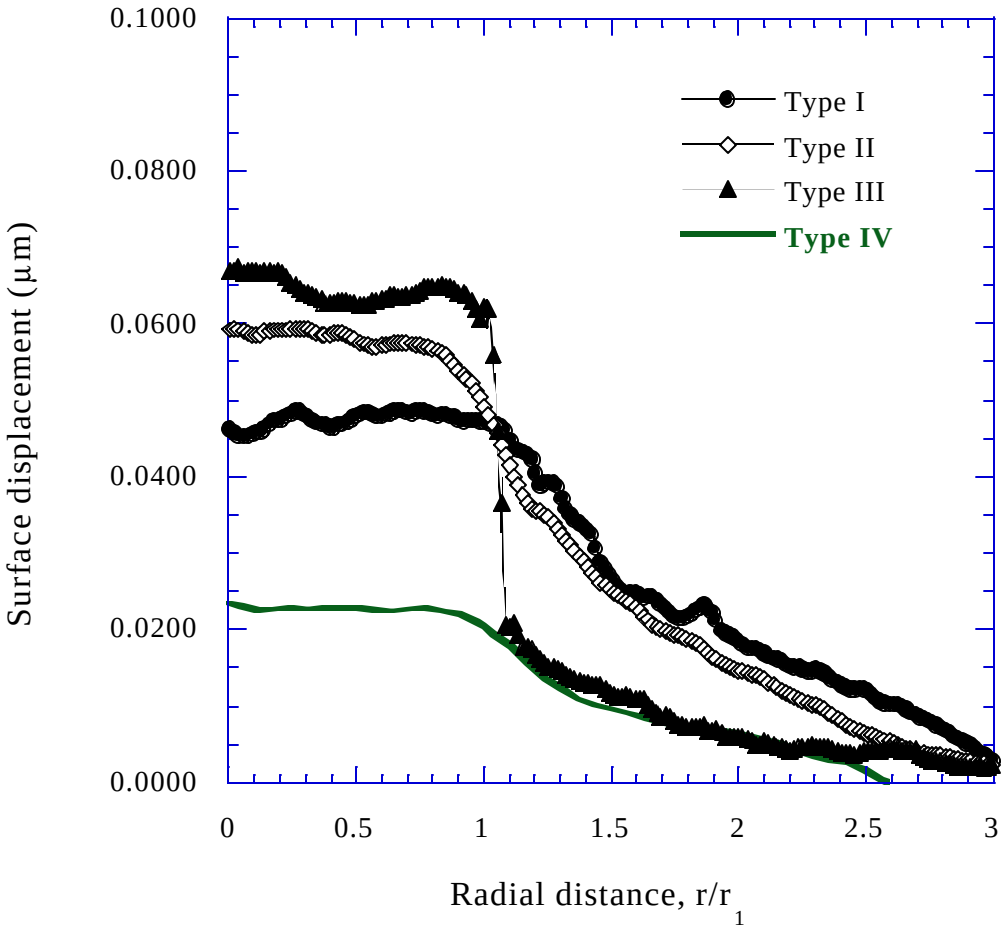

Fig. 3.9. Displacement profiles measured on the composite sample surface.

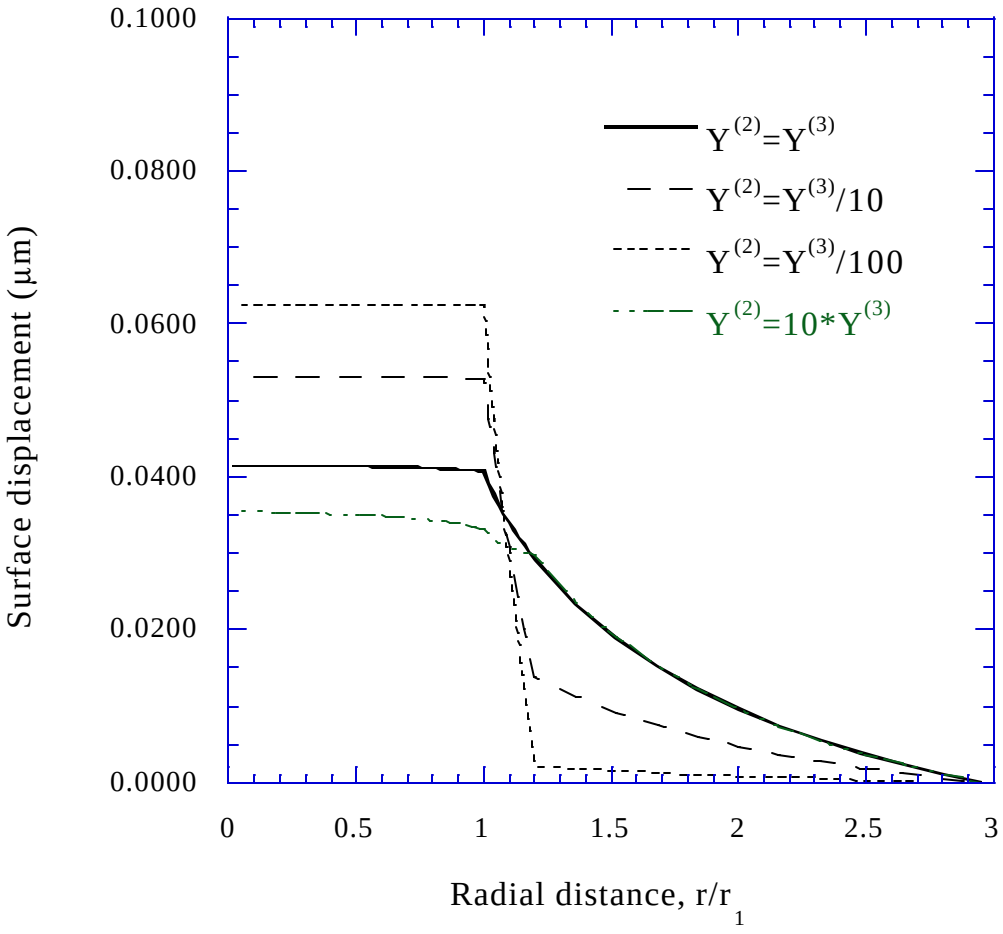

Fig. 3.10. Displacement profiles predicted by theoretical analysis (relative to $r = 3r_1$).

4. ELECTROMECHANICAL COUPLING IN PIEZOCOMPOSITES

4.1 Introduction

The key principle in designing piezoelectric ceramic-polymer composites is to maximize the electromechanical coupling. Maximum coupling is achieved by building a composite structure that transfers the applied external stresses to the composite's piezoelectric component in a pattern that most nearly approximates the piezoceramic's maximally coupled stress patterns (Smith, 1992). In this chapter, this principle is applied to the hydrostatic behavior of 1-3 piezocomposites.

Piezoceramics, which are used commonly as ultrasonic transducer materials, suffer from several disadvantages when used for hydrophone application. The piezoelectric response of a PZT ceramic under hydrostatic pressure is shown schematically in Fig. 4.1. The stress induced electric displacement D_3 can be resolved into two parts. The first part corresponds to the axial stress while the second part corresponds to the lateral stress. Due to the opposite sign of the piezoelectric charge coefficients d_{33} and d_{31}, these two parts are opposite in sign and the net piezoelectric effect is small. The hydrostatic piezoelectric coefficient d_h of PZT is defined as $d_h = 2d_{31} + d_{33}$. The coefficient d_h of PZT is low even though the magnitudes of both d_{33} and d_{31} are large. The hydrostatic voltage coefficient $g_h = \frac{d_h}{e_{33}^T}$ is also small because of the high dielectric constant e_{33}^T.

Smith (1992) has shown that the combination of a lateral stress with sign opposite to that of the axial stress provides the maximal coupling to D_3 in a PZT ceramic as shown in Fig. 4.2. Thus, an effective way to increase the magnitude of d_h and g_h is the use of a composite structure design. Among various types of composite, piezoelectric composites with 1-3 connectivity have attracted a great deal of attention and have been used widely for underwater hydrophone applications (Haun and Newnham, 1986).

$$D_3 = d_{31}T_{11} + d_{31}T_{22} \qquad D_3 = d_{33}T_{33} \qquad D_3 = d_{31}(T_{11} + T_{22}) + d_{33}T_{33}$$
$$= 2d_{31}(-p) > 0 \qquad = d_{33}(-p) < 0 \qquad = d_h(-p)$$

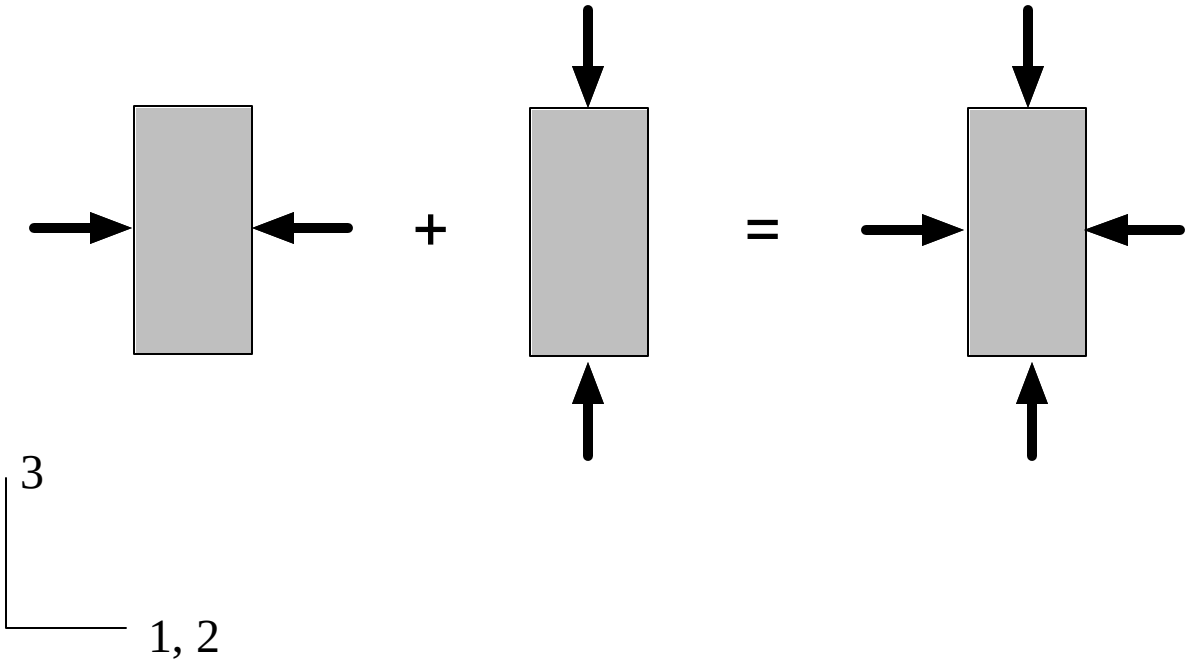

Fig. 4.1. Schematic of the hydrostatic response of a piezoceramic.

$$D_3(\max) = d_{31}(T_{11} + T_{22}) + d_{33}T_{33}$$
$$\approx d_{33}T_{33} - 2d_{31}p$$

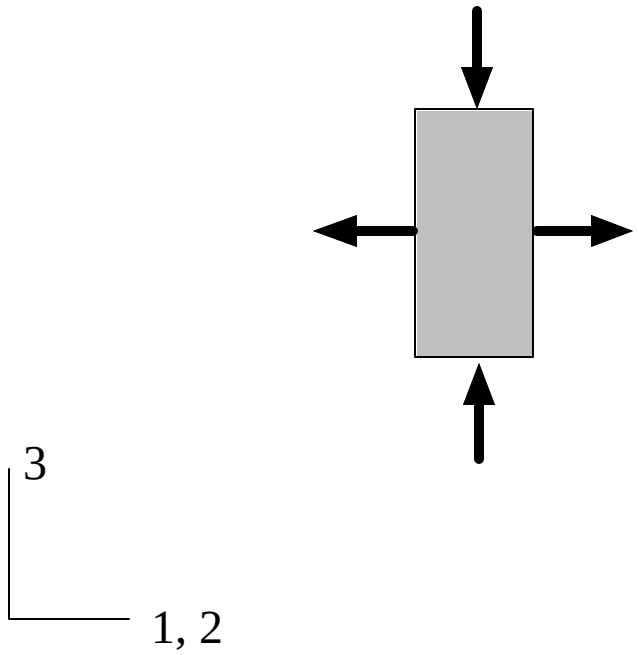

Fig. 4.2. Schematic of the maximum direct stress pattern in a PZT.

The hydrostatic response of a 1-3 piezocomposite is shown schematically in Fig. 4.3. The volume average of the stress-induced electric displacement $\langle D_3 \rangle$ is dependent on the volume average axial stress and volume average lateral stress in the piezoceramic rods. Because of the stress transfer from the piezoelectrically passive polymer phase to the piezoelectrically active ceramic phase, the hydrostatic response of this piezocomposite can be dramatically improved over the single-phase piezoceramic. In designing 1-3 piezocomposites, the goal of maximizing the electromechanical coupling can be achieved either by increasing the axial stress or by effectively reducing the lateral stress in the piezoceramic rods.

Maximizing electromechanical coupling in piezocomposites is an inverse problem. In the following two sections, the electromechanical coupling in 1-3 piezocomposites is quantified in terms of the effective hydrostatic piezoelectric constants $\bar{d}_h$ and $\bar{g}_h$. Since there is no universal method for solving inverse problems, a parametric study is performed to examine systematically the influence of matrix stiffness, rod aspect ratio, interlayer stiffness, and rod volume fraction on the hydrostatic performance of a 1-3 piezocomposite in terms of the effective hydrostatic piezoelectric coefficients.

4.2 Effective Hydrostatic Performance of 1-3 Piezocomposites

To study electromechanical coupling in 1-3 piezocomposites for hydrostatic applications, the following boundary conditions are imposed on the piezocomposite cylinder developed in Chapter 2:

$$\left.\begin{aligned} p_z(\pm l) &= -p \\ p_r(r_3) &= -p \\ \phi(\Omega) &= 0 \end{aligned}\right\} \tag{4.1}$$

where p represents constant pressure.

$$\left\langle D_3^{(1)} \right\rangle = \left\langle d_{31} T_{11}^{(1)} \right\rangle + \left\langle d_{31} T_{22}^{(1)} \right\rangle + \left\langle d_{33} T_{33}^{(1)} \right\rangle$$

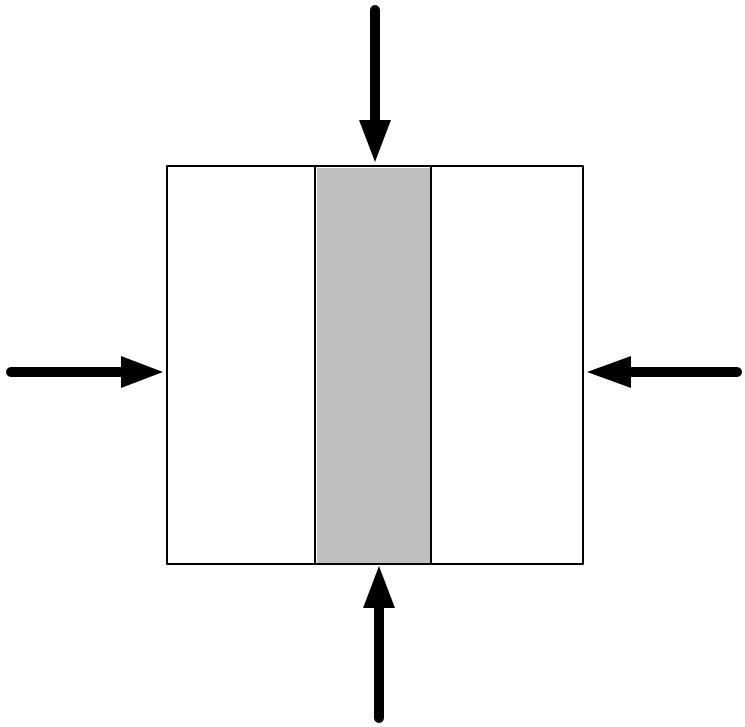

Fig. 4.3. Schematic of the hydrostatic response of a 1-3 piezocomposite.

The volume average of the hydrostatic pressure-induced electric displacement in the composite cylinder is given by

$$\left\langle D_z^{(1)} \right\rangle = \left\langle d_{31} T_{rr}^{(1)} \right\rangle + \left\langle d_{31} T_{qq}^{(1)} \right\rangle + \left\langle d_{33} T_{zz}^{(1)} \right\rangle + \left\langle e_{33}^{T} E_z^{(1)} \right\rangle \tag{4.2}$$

where $\langle \bullet \rangle$ represents volume average. For a homogeneous PZT rod with a hydrostatic piezoelectric constant d_h, the volume average of the pure hydrostatic pressure-induced electric displacement is

$$D_z = -d_h p \,. \tag{4.3}$$

Thus the effective hydrostatic piezoelectric constant of the 1-3 piezocomposite is given by

$$\bar{d}_h = \frac{\left\langle D_z^{(1)} \right\rangle}{-p} \,. \tag{4.4}$$

The effective dielectric constant $\bar{e}_{33}^{T}$ of the composite can also be predicted by using the composite cylinder model. Since the dielectric constant of the polymer is very small when compared with that of the piezoceramic, the effective dielectric constant is approximated as

$$\bar{e}_{33}^{T} \approx e_{33}^{T(1)} v_f \tag{4.5}$$

where $e_{33}^{T(1)}$ is the dielectric constant of the piezoceramic and v_f is the volume fraction of the piezoceramic rods. The effective piezoelectric voltage constant is given by

$$\bar{g}_h = \frac{\bar{d}_h}{\bar{e}_{33}^{T}} \,. \tag{4.6}$$

The composite figure of merit defined as $\bar{d}_h \bar{g}_h$ is approximated as

$$\bar{d}_h \bar{g}_h \approx \frac{\bar{d}_h^{\,2}}{\varepsilon_{33}^{T\,(1)} v_f} \tag{4.7}$$

Predictions were made of the effective piezoelectric constants and the figure of merit in 1-3 piezoelectric composites using the Eqs. (4.4), (4.6) and (4.7). The piezoceramic rods are assumed to be PZT-5H (Morgan Matroc Inc., 1989) and the properties are listed in Table 2.1. The polymer matrix is assumed to be Spurr epoxy with the properties which are given in Table 2.3 (Case 1). The diameter of the PZT-5H rods is 0.75 mm.

4.3 Load Transfer and Stress Amplification

4.3.1 Predictions of effective $\bar{d}_h$ and $\bar{g}_h$ for a 1-3 piezocomposite

Predictions of the effective hydrostatic piezoelectric constant $\bar{d}_h$ for a typical PZT-5H rod aspect ratio ($2l/d = 13.3$) using the finite concentric cylinder model are plotted in Fig. 4.4 for a range of rod volume fractions (no interlayer). Here $2l$ is the length of the PZT rods and d is the diameter. The effective $\bar{d}_h$ exceeds the d_h of the constituent ceramic, approaching a value three times as high as that of pure PZT-5H ($d_h = 45 \times 10^{-12}$ m/V). The prediction of $\bar{d}_h$ made from the generalized plane-strain model is also shown in Fig. 4.4. The value corresponding to the generalized plane-strain model is larger than that of the finite concentric cylinder model. Additionally the peak value of $\bar{d}_h$ shifts to a lower volume fraction region for the plane-strain prediction.

Calculated values of $\bar{g}_h$ and $\bar{d}_h \bar{g}_h$ are plotted in Fig. 4.5 and Fig. 4.6, respectively, as a function of the rod volume fraction for $2l/d = 13.3$. The $\bar{g}_h$ peaks at low ceramic

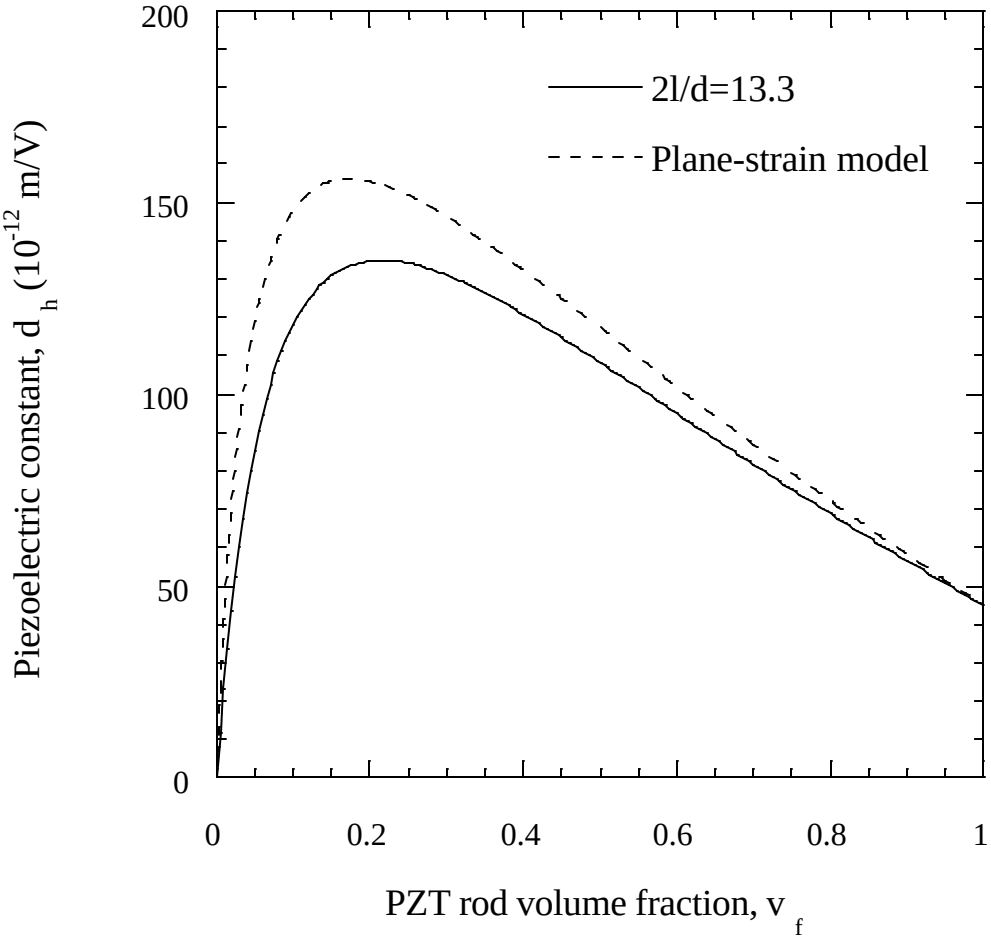

Fig. 4.4. Variation of $\bar{d}_h$ with volume fraction of PZT rods for the case of no interlayer.

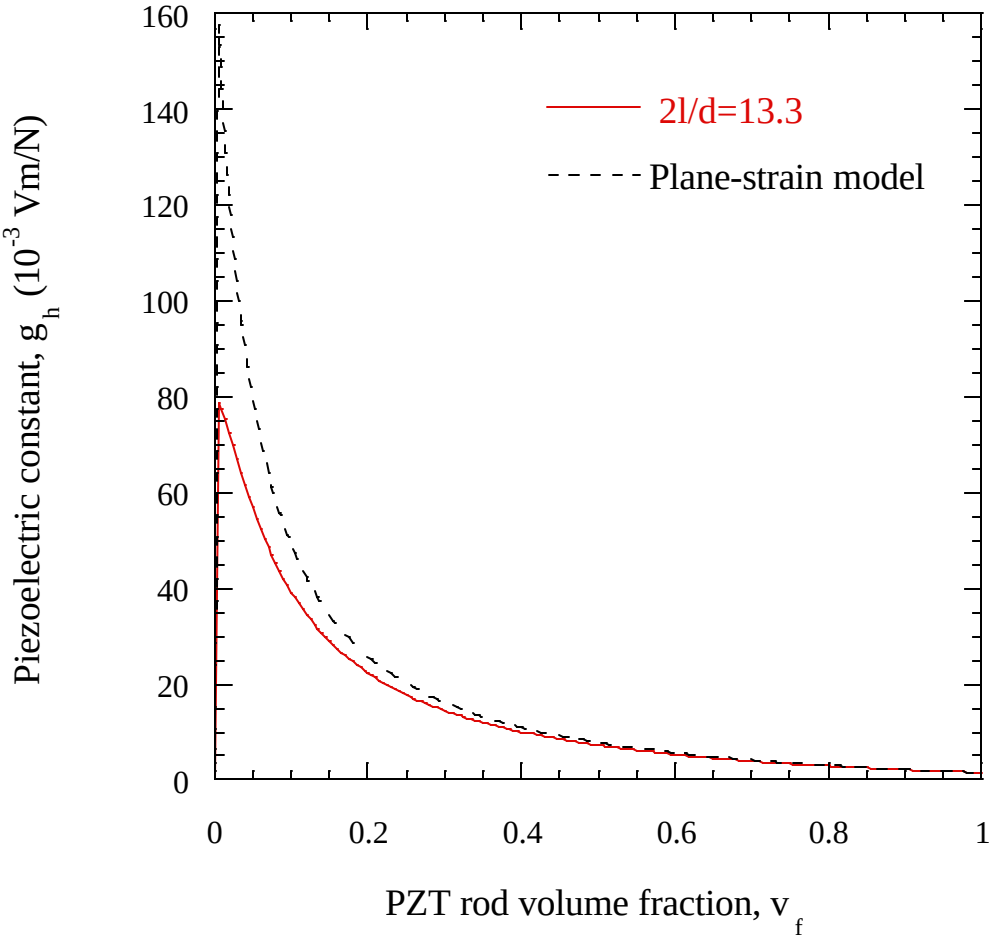

Fig. 4.5. Variation of $\bar{g}_h$ with volume fraction of PZT rods for the case of no interlayer.

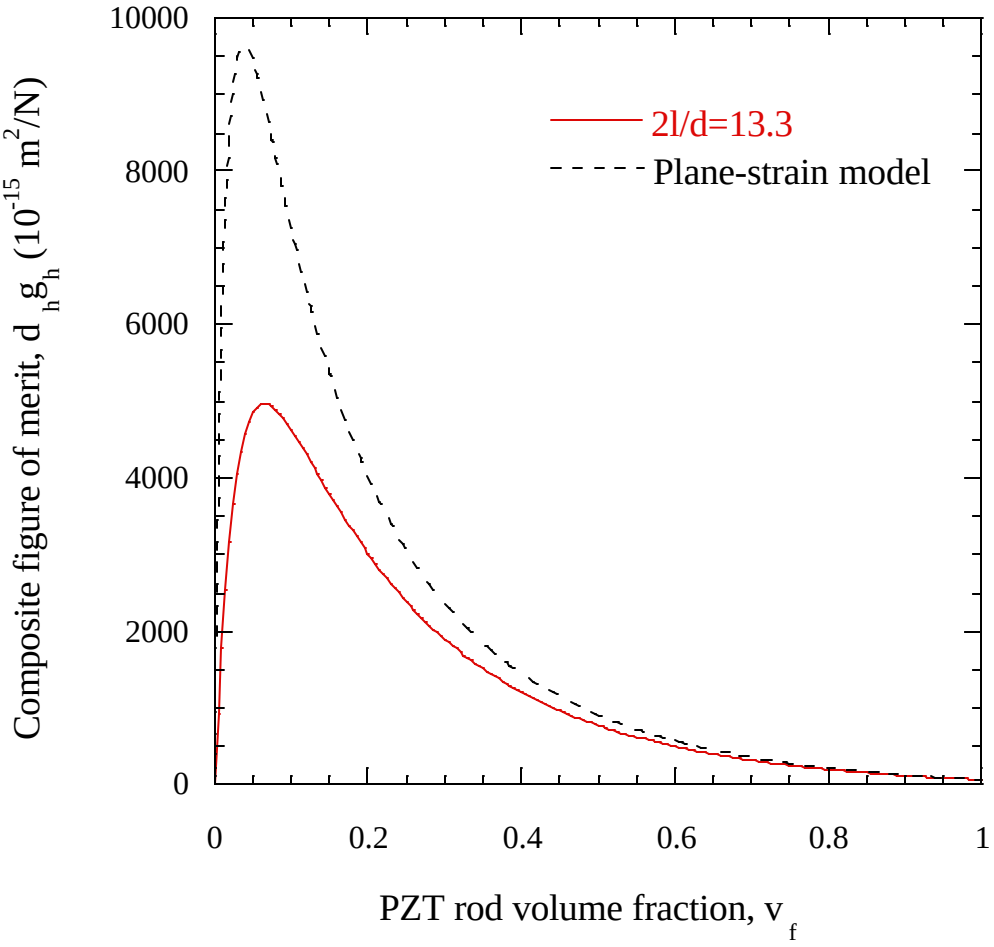

Fig. 4.6. Variation of $\bar{d}_h \bar{g}_h$ with volume fraction of PZT rods for the case of no interlayer.

content, attaining a value greater than that for the pure ceramic ($g_h = 1.5\times10^{-3}$ Vm/N). This enhancement is due to the dilution of the dielectric permittivity and the increase of $\bar{d}_h$. A somewhat broader peak in the figure of merit, $\bar{d}_h\bar{g}_h$, also appears at low PZT-5H content for essentially the same reason as its $\bar{g}_h$ peak. The value attained is significantly higher than the pure ceramic ($d_h g_h = 67.5\times10^{-15}$ m^2/N). Again, the plane strain model predicts significantly higher values of $\bar{d}_h$ and $\bar{d}_h\bar{g}_h$ than the composite cylinder model.

The stress pattern in the piezoceramic is depicted in terms of the normalized average stresses in the PZT rods which are plotted in Fig. 4.7 along with the $\bar{d}_h$ for the same case as in Fig. 4.4. There is a large stress amplification in the axial stress $T_{zz}^{(1)}$ especially for the low PZT rod volume fraction region. Although the lateral stress is also slightly increased, competition among the axial stress, the lateral stress and the volume fraction of the PZT rod gives an enhanced effective hydrostatic piezoelectric constant $\bar{d}_h$. Thus, axial stress amplification is beneficial for the enhancement of $\bar{d}_h$.

4.3.2 Influence of PZT rod aspect ratio on $\bar{d}_h$

The aspect ratio of the PZT rods, $2l/d$, has been proven in experiments to be a critical parameter in 1-3 piezocomposites. The effect of the aspect ratio is not included in the simple generalized plane-strain models (Smith, 1993; Jensen, 1991; Cao, Zhang and Cross, 1992). However, this effect can be studied using the current finite concentric cylinder model. A parametric study was carried out to assess the influence of PZT-5H rod aspect ratio on $\bar{d}_h$. Material properties of PZT-5H and the polymer matrix are the same as in Table 2.1 and Table 2.3 (Case 1). The results are plotted in Fig. 4.8 for several different aspect ratios. For each case, the $\bar{d}_h$ exhibits a peak value which shifts to higher volume fractions with decreasing aspect ratio. The peak value increases with increasing aspect ratio, but there is a saturation of the effect for $2l/d > 500$. Thus, the enhancement of axial stress in the PZT rod from increasing the rod aspect ratio has an upper limit. This

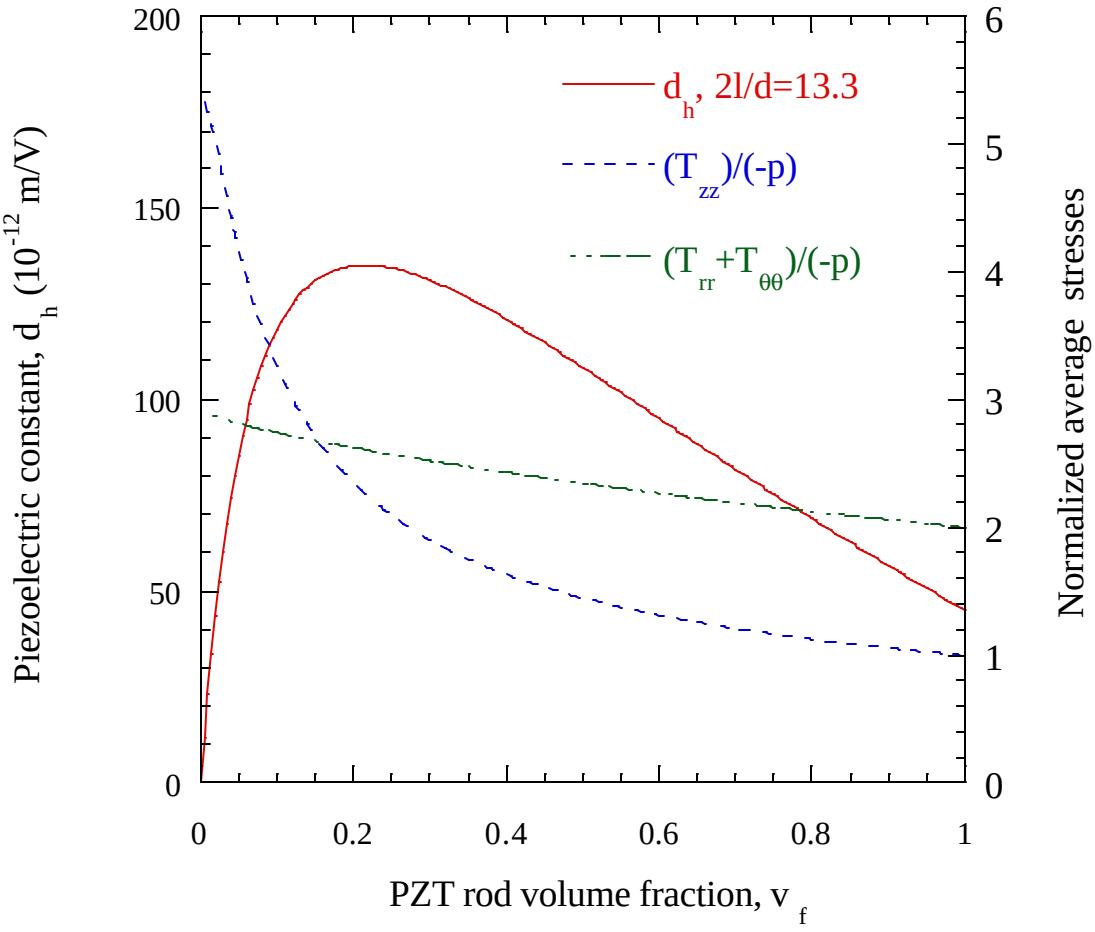

Fig. 4.7. Variation of $\bar{d}_h$ and the average stresses in the PZT rod with rod volume fraction for the case of no interlayer.

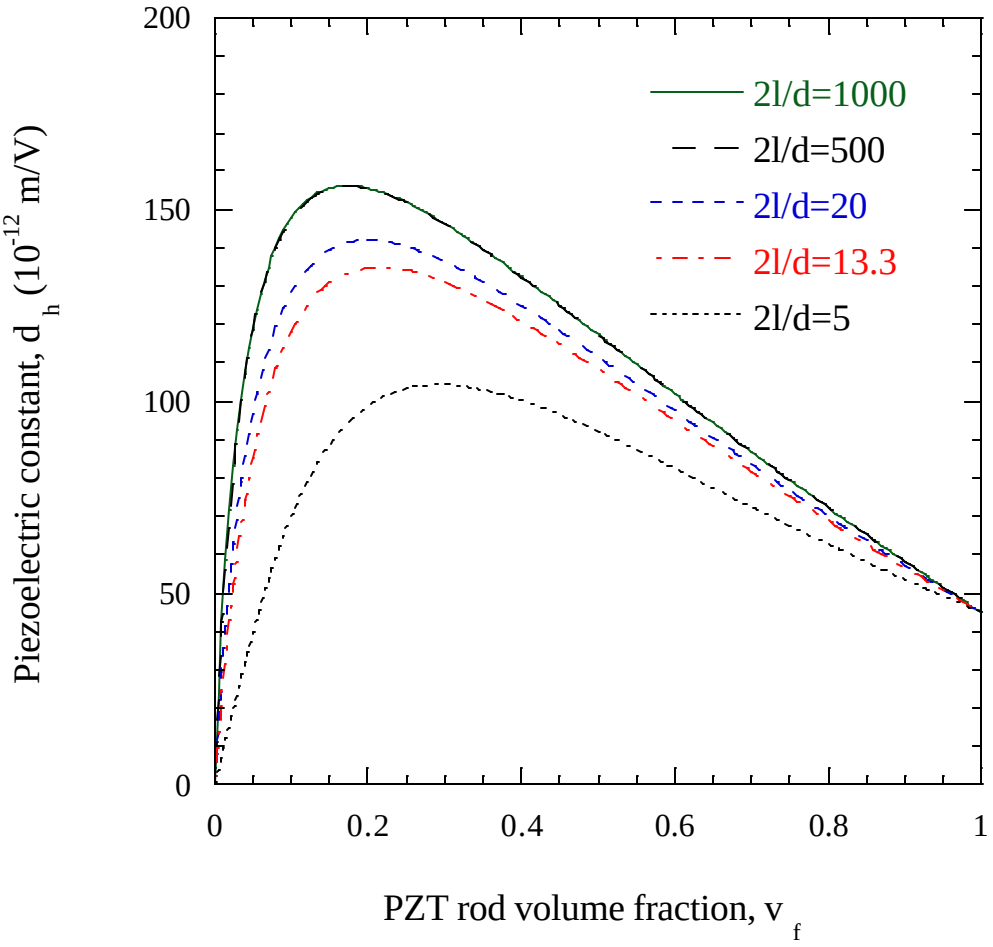

Fig. 4.8. Variation of $\bar{d}_h$ with volume fraction of PZT rods for different rod aspect ratios.

saturated value of $\bar{d}_h$ approaches the value predicted by the generalized plane strain model. For a composite with small rod aspect ratio, the simple generalized plane strain models significantly over predict the $\bar{d}_h$. In practical applications, the PZT rod aspect ratios are typically small ($2l/d < 25$) due to poling limitations, and the finite concentric cylinder model would more accurately predict the behavior.

4.3.3 Influence of matrix stiffness on $\bar{d}_h$

The influence of matrix stiffness on $\bar{d}_h$ of 1-3 piezocomposites was examined by varying the matrix stiffness ($2l/d = 13.3$) and using the finite concentric cylinder model. The results are plotted in Fig. 4.9 where $Y^{(3)}$ is the Young's modulus of the matrix and Y^0 is the modulus of plain Spurr epoxy listed in Table 2.3 (Case 1). The $\bar{d}_h$ increases with decreasing matrix stiffness but saturates for a very soft matrix. The effect of softening the matrix is similar to the effect of increasing the PZT rod aspect ratio. These two effects are responsible for causing axial stress amplification, which is significant at low PZT rod volume fractions.

4.4 Stress Reduction and The Role of Interphase

The enhancement of electromechanical coupling under hydrostatic pressure is achieved either by increasing the axial stress or by decreasing the lateral stress in the piezoceramic rods. The aforementioned results of the influence of the rod aspect ratio and the matrix stiffness on $\bar{d}_h$ demonstrates how axial stress amplification in the rods can be achieved from these two effects. The results also show the saturation from these two effects.

Because the actual stress transfer is through the interface between the rods and the matrix, the incorporation of any existing interphase region into the micromechanical analysis of 1-3 piezocomposites may be important for understanding composite behavior.

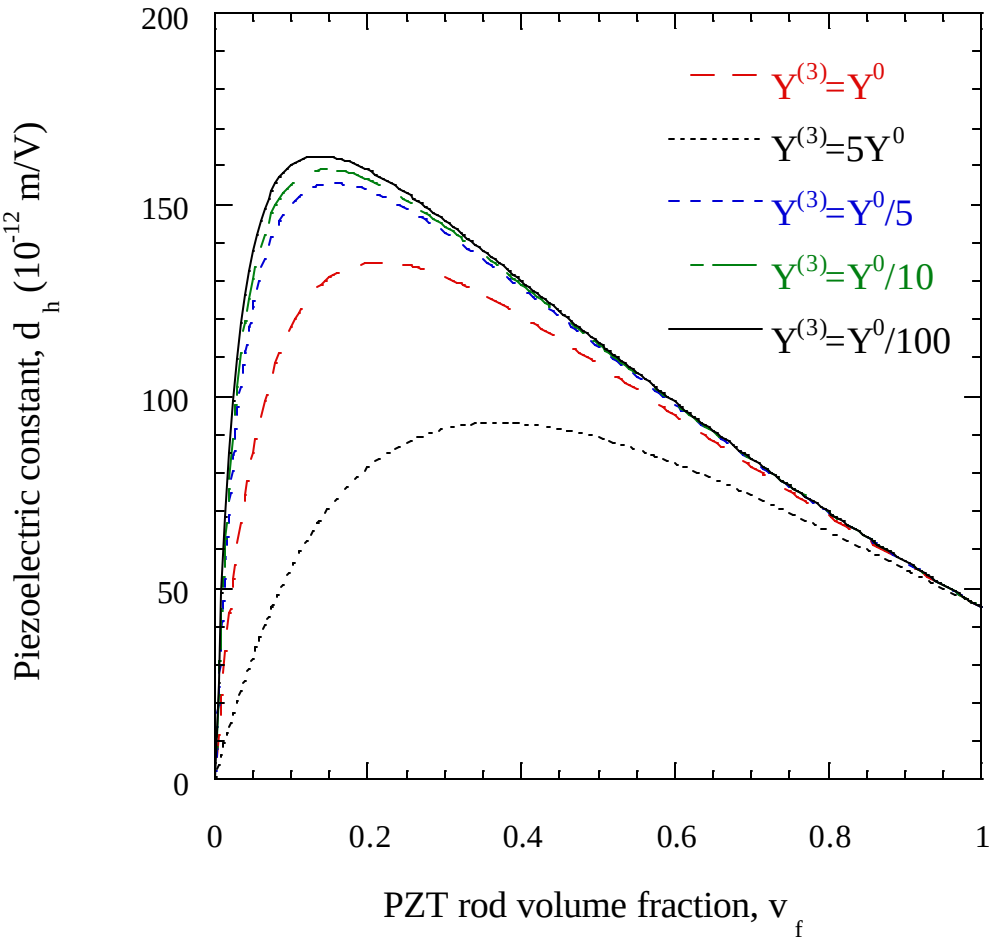

Fig. 4.9. Variation of $\bar{d}_h$ with volume fraction of PZT rods for different matrix moduli.

Experiments in Chapter 3 verified that an interlayer significantly influences the out-of-plane displacement of a 1-3 piezocomposite. In Chapter 2, a thin interlayer was introduced between the piezoceramic rods and the matrix in the micromechanical model. Interlayer properties had a significant effect on the effective charge constants, $\bar{d}_{33}$ and $\bar{d}_{31}$, as shown in Figs. 2.12 and 2.13. It is proposed that the presence of this thin interlayer can influence the hydrostatic behavior of the composite and change the sensitivity. Kim, Rittenmyer and Kahn (1993) showed that by casting a soft epoxy interlayer between PZT rods and a stiff polymer preform matrix, a 1-1-3 piezocomposite with high hydrostatic charge constant can be obtained. Sherrit, Wiederick and Mukherjee (1992) also described a 1-3 type PZT-air piezocomposite with extremely high effective hydrostatic piezoelectric constants and figure of merit.

4.4.1 Lateral stress reduction and the role of interlayer

The influence of an interlayer with a thickness of 0.1 mm is shown in Fig. 4.10, where the $Y^{(2)}$ is the interlayer modulus and Y^0 is the modulus of plain Spurr epoxy as given in Table 2.3 (Case 1). The PZT-5H rod aspect ratio is fixed at 13.3. The introduction of a thin soft interlayer greatly reduces the lateral stress in the PZT rod. The effect of softening the interlayer becomes dominant for rod volume fractions between 20% and 45% where the $\bar{d}_h$ increases significantly with a decrease in the interlayer stiffness.

The effect of the lateral stress reduction for the case of a soft interlayer is illustrated in Fig. 4.11. The average stresses in the PZT rods are plotted in Fig. 4.11 along with the $\bar{d}_h$ for $Y^{(2)} = Y^0/100$. A comparison with Fig. 4.7 reveals that there is a large reduction in the lateral stress for the compliant interlayer. Although the axial stress is also slightly decreased, competition among the axial stress, the lateral stress and the volume fraction of the PZT rod gives an enhanced effective hydrostatic piezoelectric constant $\bar{d}_h$. This

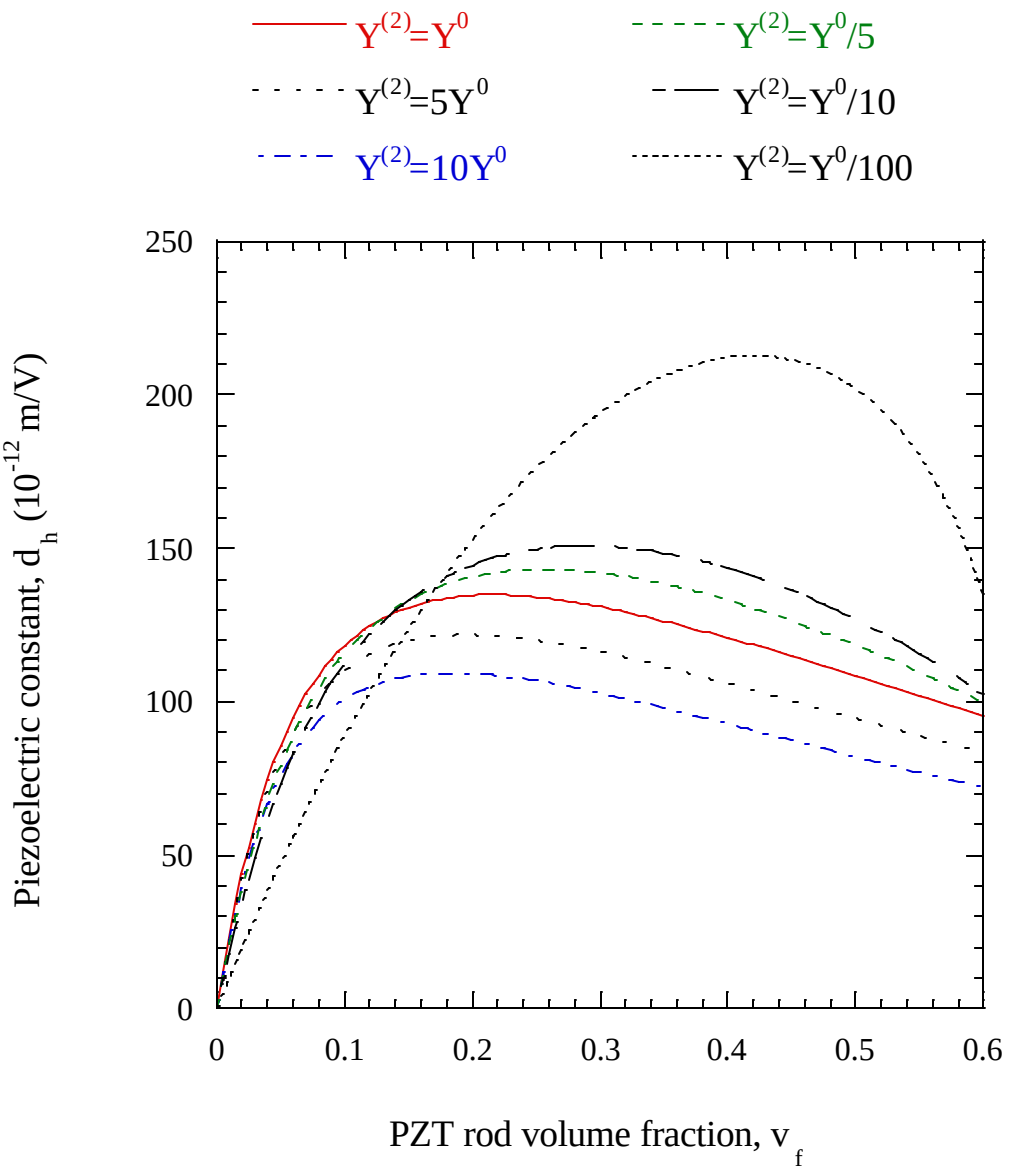

Fig. 4.10. Variation of $\bar{d}_h$ with volume fraction of PZT rods for different interlayer moduli.

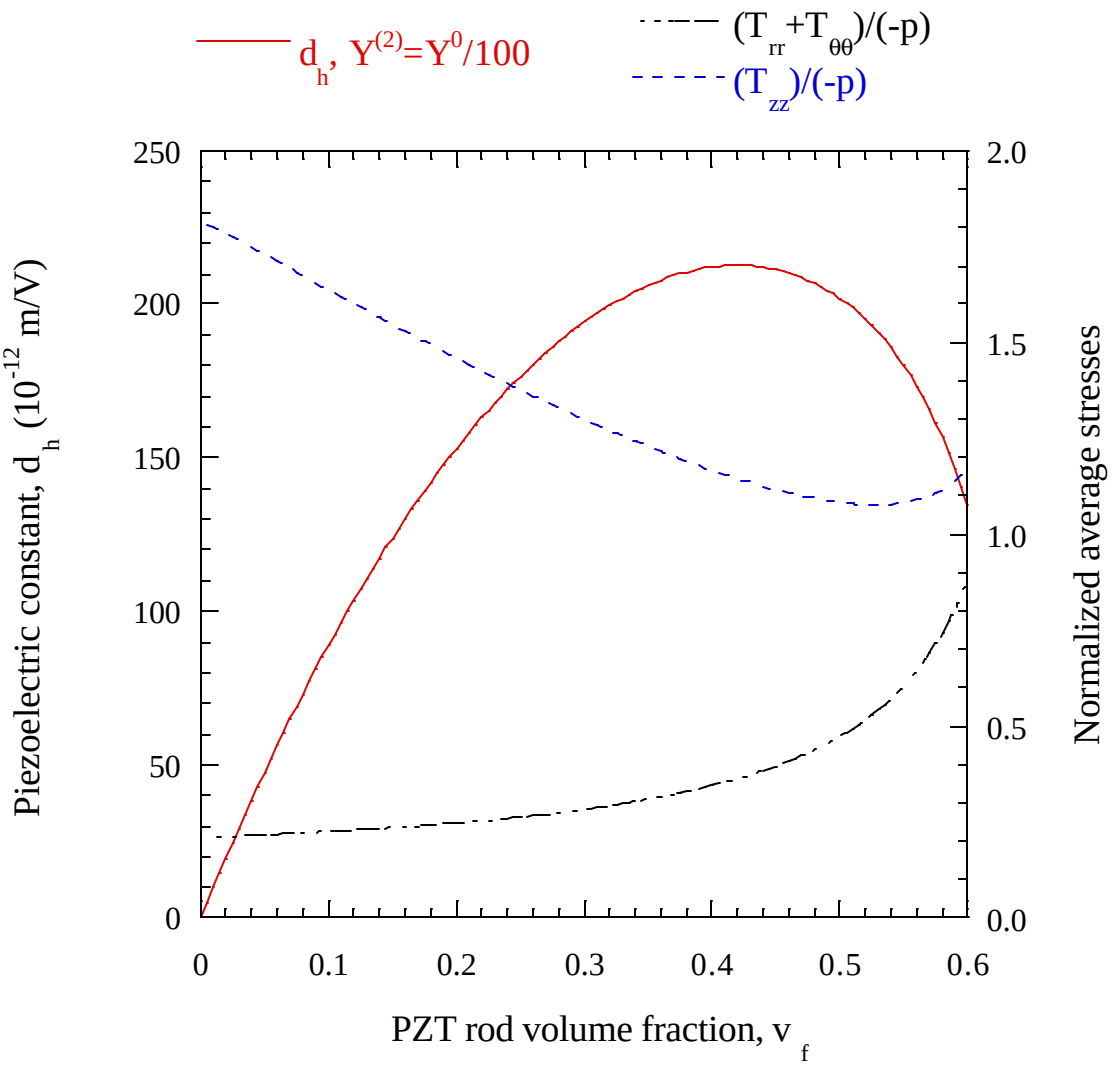

Fig. 4.11. Variation of $\bar{d}_h$ and the average stresses in the rods with rod volume fraction for the case of a very soft interlayer.

lateral stress reduction effect can be further explained by plotting the product of the average stress in the PZT rods, the rod piezoelectric constant and the rod volume fraction in Fig. 4.12 for the same case as in Fig. 4.11. According to Eq. (4.4), the difference between the curve corresponding to the average axial stress and the curve related to the lateral stress is exactly the effective hydrostatic constant $\bar{d}_h$, which is also shown in Fig. 4.12. Thus, lateral stress reduction through the introduction of a thin, soft interlayer is also beneficial for the enhancement of $\bar{d}_h$.

4.4.2 Influence of the interlayer Poisson's ratio on $\bar{d}_h$

The Poisson's ratio of the polymer matrix is also a very important parameter in designing 1-3 piezocomposites for hydrostatic applications. If the Poisson's ratio of the polymer matrix is large, the polymer matrix will be hydrostatically incompressible and large lateral stresses will develop in the piezoceramic rods. Previous solutions to suppress the Poisson effect of the polymer matrix relied on introducing bubbles into the polymer matrix to reduce the Poisson's ratio. Voids, however, will also reduce the matrix stiffness and introduce an undesired bias pressure dependence to the hydrostatic sensitivity (Haun and Newnham, 1986; Kim, Rittenmyer and Kahn, 1993)

The lateral stress in the piezoceramic rods can also be reduced by controlling the Poisson's ratio of a thin interlayer. This effect is shown in Fig. 4.13 for the case of $Y^{(2)} = Y^0 / 10$. The thickness of the interlayer is fixed at 0.1 mm and the PZT-5H rod aspect ratio is 13.3. Figure 4.13 shows a compliant interlayer with a smaller Poisson's ratio can further reduce the lateral stress in the PZT rod and increases the $\bar{d}_h$ of the 1-3 piezocomposite. The maximum $\bar{d}_h$ value is again shifted to higher PZT rod volume fraction.

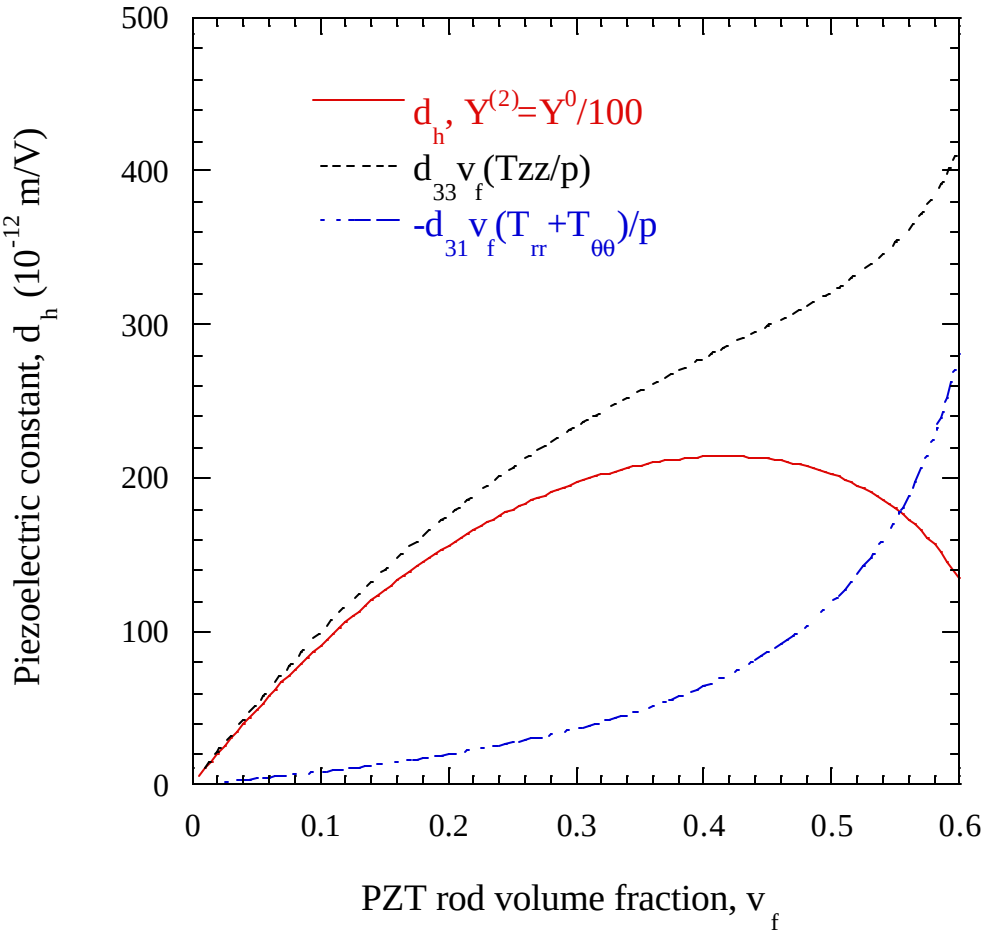

Fig. 4.12. Interactions between the axial and lateral stress versus the rod volume fraction.

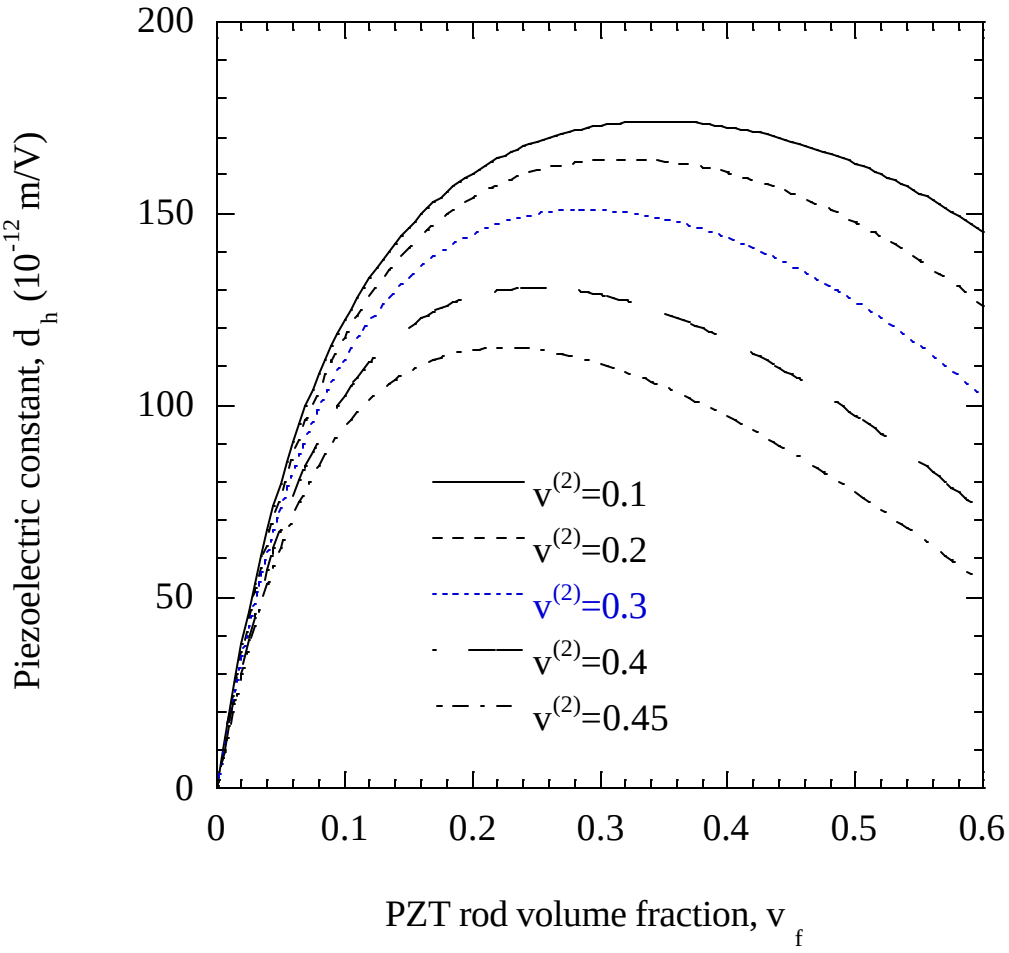

Fig. 4.13. Variation of $\bar{d}_h$ with volume fraction of PZT rods for different interlayer Poisson's ratios.

4.5 Finite Element Simulation of Piezocomposites with Tailored Interphase

In the previous discussion, lateral stress reduction and axial stress amplification were not obtained simultaneously. In order to improve the hydrostatic performance of a 1-3 piezocomposite further, the interlayer should be tailored to enhance both these effects. An interlayer that was functionally graded along the axis of the rod, such that it was stiffer at the edges of the rod to enhance load transfer and axial stress amplification and softer along the interior region of the rod to reduce lateral stresses, should be able to exploit both effects. Based on this concept, a tailored interlayer design was developed as shown schematically in Fig. 4.14. Evaluation of the hydrostatic response of a 1-3 piezoelectric composite with such an interlayer was conducted using the finite-element method. Because of the increased complexity of this tailored interphase, a numerical method is necessary to study the influence on the electromechanical coupling in the composite.

A composite cylinder model is used to represent a single piezoceramic rod, the interlayer and the surrounding matrix. The interlayer consists of two parts, the core and the edge, each with distinctive material properties. As an example, the interlayer edge was chosen as the same as the matrix. Symmetry in the axial or z coordinate is preserved. The composite model is developed with 8-node quadrilateral elements (CAX8RE elements in ABAQUS). The finite element mesh had a total of 5400 elements and is shown in Fig. 4.15. The length of the composite cylinder model $2l$ is 10 mm and the length of the interlayer core, $2H$, is 8 mm. The interlayer is of 0.1 mm thick. The diameter of the piezoceramic rod is 0.75 mm. Fig. 4.16 shows the finite mesh near the end of the interlayer core. The finite-element analysis was conducted using ABAQUS (Hibbitt Karlsson & Sorenson Inc.) software. The boundary conditions applied are shown schematically in Fig. 4.17. Material properties for the piezoceramic and epoxy matrix are from Table 2.1 and Table 2.3 (Case 1).

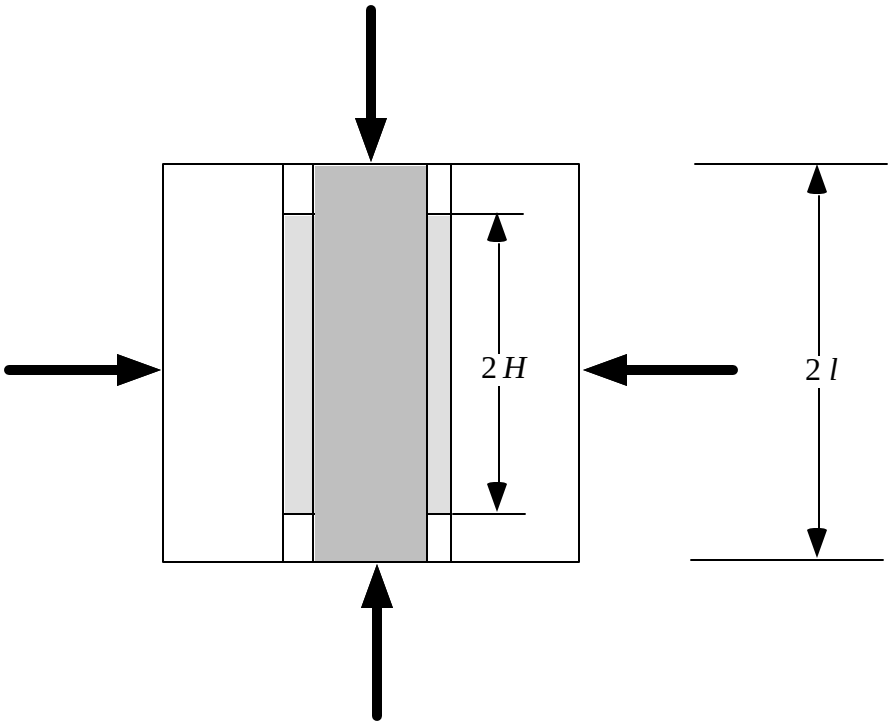

Fig. 4.14. Schematic of a 1-3 piezocomposite with a tailored interlayer.

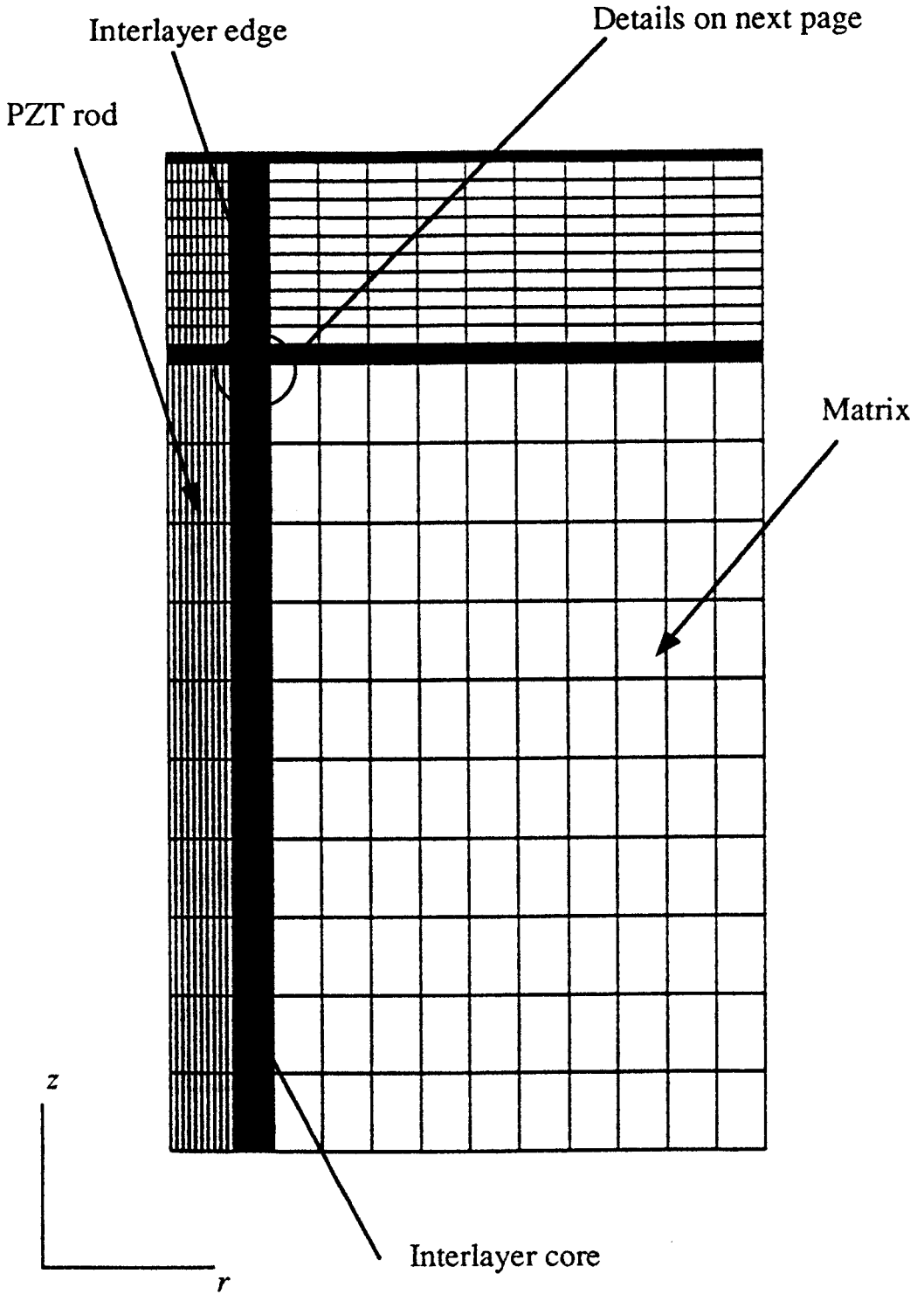

Fig. 4.15. A finite-element mesh for a composite cylinder with a tailored interlayer.

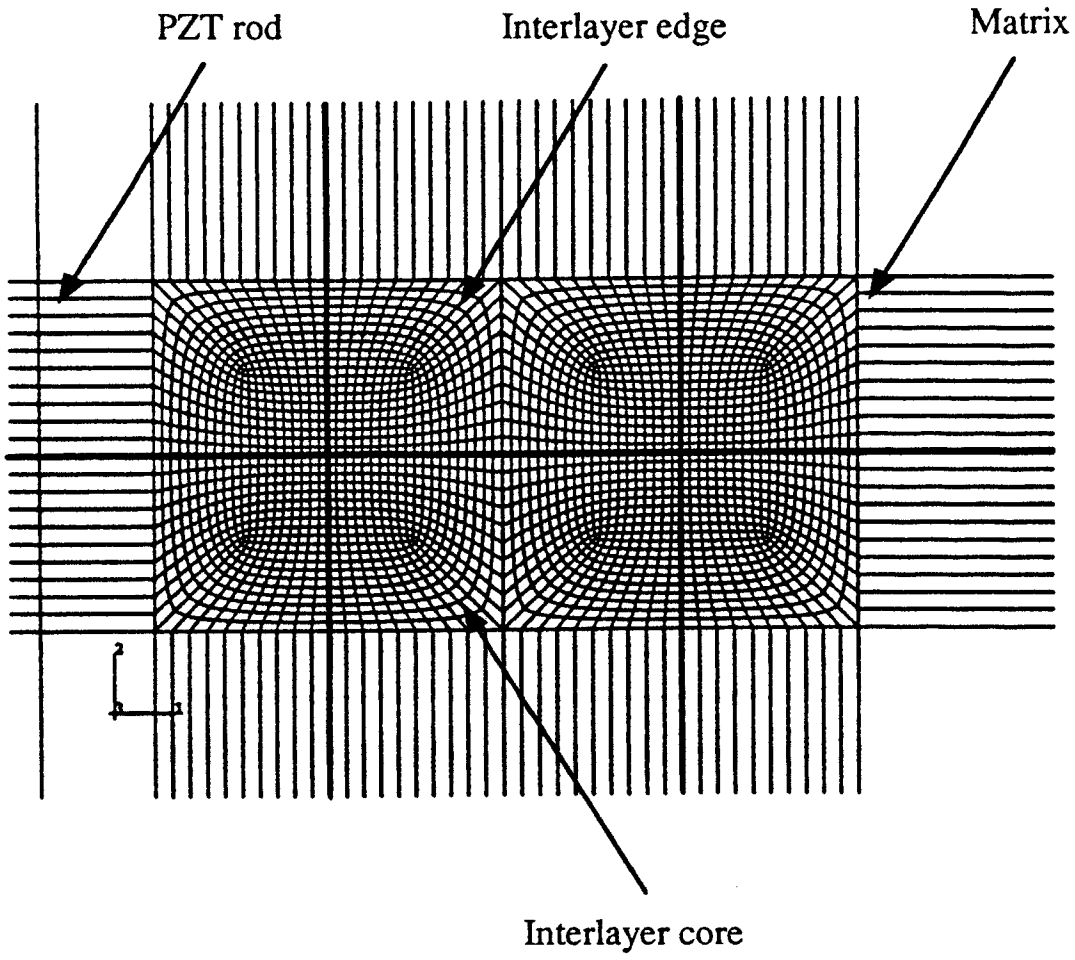

Fig. 4.16. Detail of the finite-element mesh near the edge of the soft interlayer.

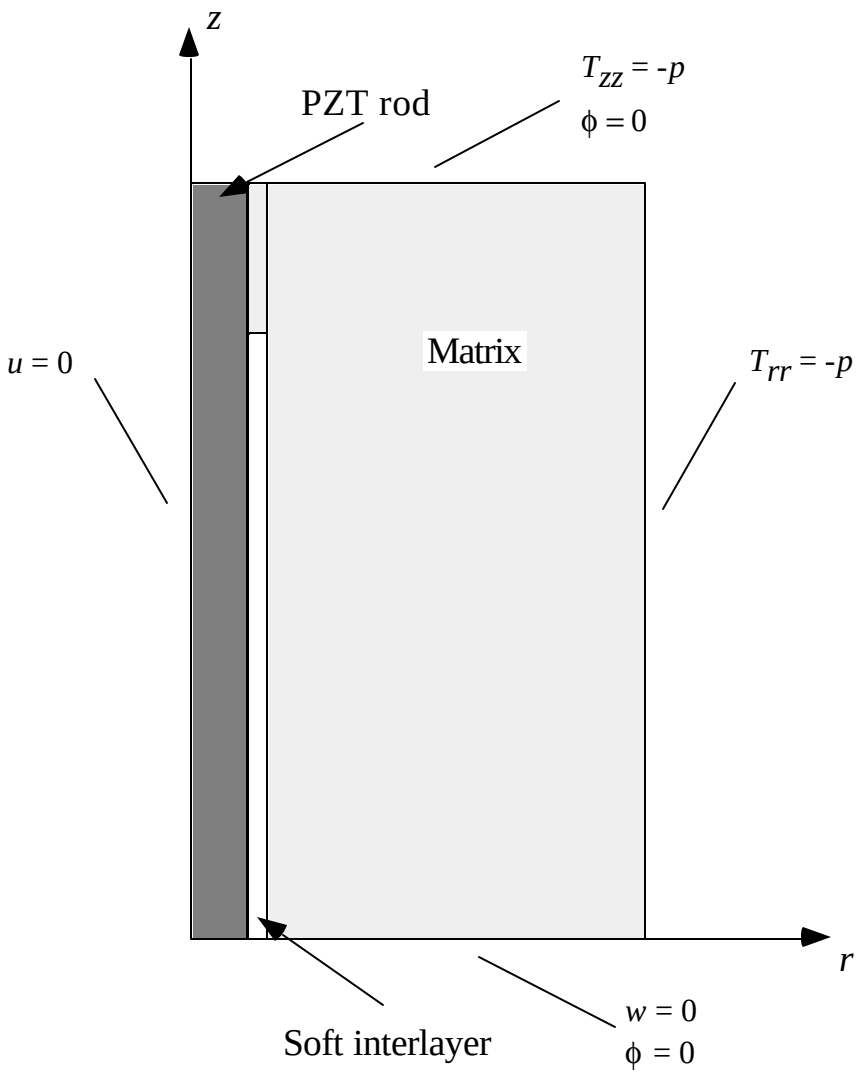

Fig. 4.17. Boundary conditions used in the finite-element analysis.

The calculated effective piezoelectric constant $\bar{d}_h$ along with values from theoretical predictions are plotted in Fig. 4.18. Finite-element results are depicted by open or closed symbols while solid or dashed lines represent analytical solutions. The composite with a graded interlayer has a broad peak when compared with the compliant interlayer case and has improved hydrostatic behavior compared with the no interlayer case. This broadened peak for the effective piezoelectric constant $\bar{d}_h$ leaves room for the consideration of other design parameters, such as the rod volume fraction that is critical to the effective dielectric constant and the acoustic impedance.

4.6 Discussion

The analysis of the hydrostatic performance of 1-3 piezocomposites demonstrated how to optimize electromechanical coupling in the design of a piezocomposite material for a specific application: to build a composite structure that transfers the external stresses applied to the active component of the composite in a pattern that most nearly approximates the piezoceramic's maximally coupled stress pattern. The micromechanics model developed in Chapter 2 was used to predict the effective hydrostatic piezoelectric constants $\bar{d}_h$, $\bar{g}_h$ and the figure of merit, $\bar{d}_h \bar{g}_h$. Parametric studies were performed to assess the influence of matrix stiffness, rod aspect ratio, interlayer stiffness, and rod volume fraction on the hydrostatic piezoelectric constants. Increasing the aspect ratio significantly increases the $\bar{d}_h$ due to the axial stress amplification and increased load transfer. This effect saturates for an aspect ratio of $2l/d > 500$ when the solution approaches the values predicted by a generalized plane strain model (infinite aspect ratio). Even though a large aspect ratio would increase hydrostatic sensitivity, piezocomposites are typically fabricated with small rod aspect ratios due to poling limitations. The properties of these piezocomposites are more accurately modeled by a finite concentric cylinder model.

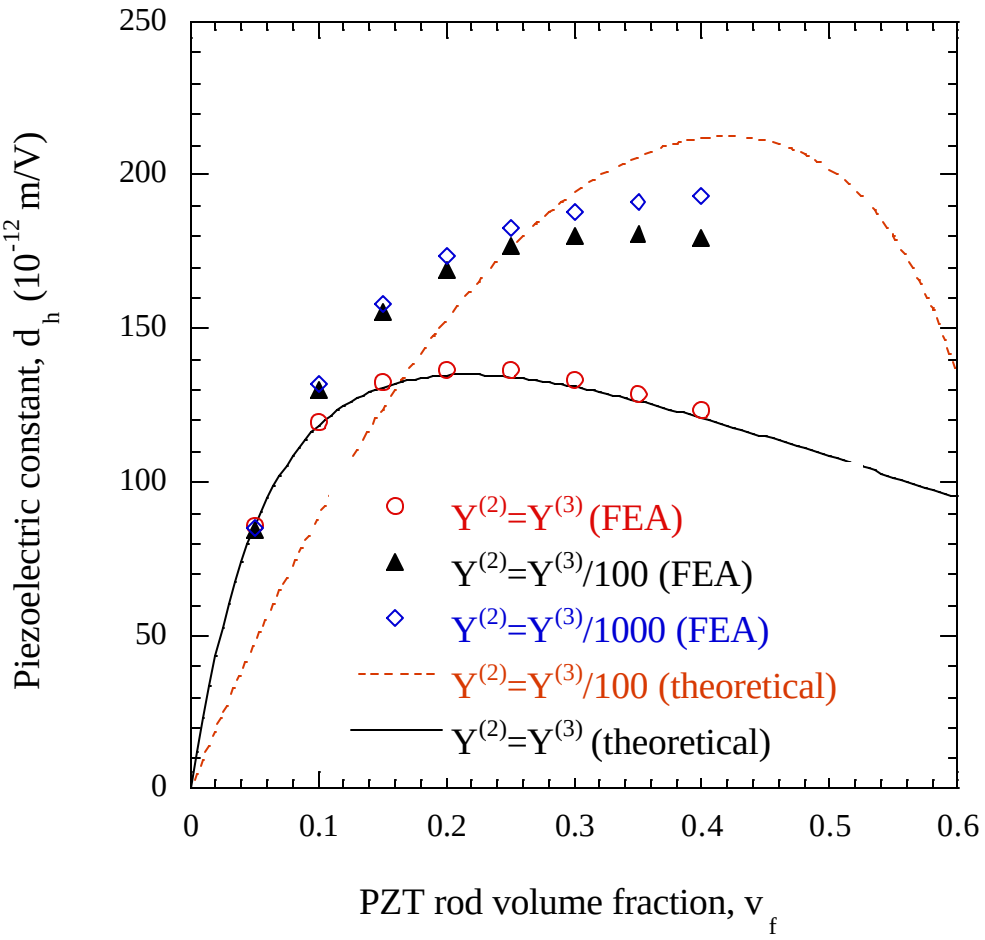

Fig. 4.18. Prediction of $\bar{d}_h$ for a 1-3 piezocomposite with a tailored interlayer.

The $\bar{d}_h$ can also be increased by decreasing the matrix stiffness or introducing a compliant interlayer around the PZT rods. Decreasing the matrix stiffness causes axial stress amplification, which leads to higher $\bar{d}_h$ values. However, difficulties may exist in fabricating an entire composite with a very compliant matrix. A compliant interlayer significantly increases the $\bar{d}_h$ by effectively attenuating the lateral stress in the PZT rods without decreasing the overall stiffness of the composite. A compliant interlayer with smaller Poisson's ratio can further increase the $\bar{d}_h$ of the 1-3 piezocomposite.

To improve the hydrostatic performance of a 1-3 piezocomposite further, one must tailor the interlayer to enhance both reduction in lateral stress and axial stress amplification. An interlayer that is functionally graded along the axis of the rod, such that it is stiffer at the edges of the rod to enhance load transfer and axial stress amplification and softer along the interior region of the rod to reduce lateral stresses, could exploit both effects. Such an optimal interlayer design would provide improved electromechanical coupling and design flexibility.

5. SUMMARY AND CONCLUSIONS

The application of piezoceramic-polymer composites continues to grow in biomedical, automotive and other industries. Because of the potential of piezocomposites for novel applications it is important to improve the conceptual understanding of these materials, to develop practical design rules, and to investigate ways of optimizing performance. In this dissertation several contributions have been made toward these goals.

5.1 Summary of Results

A micromechanics model was developed for predicting the local fields and effective behavior in piezocomposites with 1-3 connectivity. Because the presence of a thin interlayer or polymer coating around the ceramic rods can influence the local interaction between the piezoceramic and polymer matrix and change the overall performance of the composite, the model was designed to incorporate an interlayer with varying properties. This composite model was also characterized by its finite length, chosen to be equal to that of the embedded piezoceramic rods. The solutions of the displacement, stress, and electric fields in the composite model were obtained using two displacement potential functions and an electrical potential function.

The micromechanics model was used to predict static displacement behavior in a 1-3 piezocomposite. Predictions from the current model were compared with solutions generated by simple plane-strain models and other micromechanical models. The results demonstrated that the local out-of-plane displacement of the piezocomposite is highly dependent on the interaction between the polymer matrix, a thin interlayer, and the piezoelectric ceramic. In order to enhance the out-of-plane displacement, one should choose a passive matrix with small Young's modulus. This result is similar to that obtained from simple models. However, the overall stiffness of the composite is dependent on the matrix modulus, especially for lower

volume fractions. By introducing a thin compliant interlayer, one can greatly increase the out-of-plane displacement of the rod while satisfying the requirement for overall stiffness of the composite. The interlayer essentially serves to couple or decouple the rods from the matrix, depending on its stiffness.

The micromechanics model was also used to estimate the effective piezoelectric constants $\bar{d}_{33}$ and $\bar{d}_{31}$ for the composite. Rod aspect ratio, matrix properties and interlayer properties had a significant effect on the values of $\bar{d}_{33}$ and $\bar{d}_{31}$. Thus, the interlayer can be tailored to optimize the properties and increase the sensitivity of 1-3 piezocomposites.

Experimental studies focused on probing surface displacements of 1-3 piezocomposites using a scanning heterodyne laser interferometer. Static surface displacements of 1-3 PZT rod-epoxy samples with different interphase regions were measured and correlated with the effective static performance of the composite. Several types of interphase regions were considered. Coatings with elastic modulus lower than that of the epoxy matrix were applied to the rods. The influence of a silane coupling agent was also investigated. Experimental displacement profiles were compared with micromechanical predictions using the finite composite cylinder model. Micro-interferometric measurements as well as the theoretical predictions demonstrated that the out-of-plane displacement of the composite is highly dependent on the properties of the polymer matrix, a thin interlayer, and the piezoelectric ceramic. The variation of surface displacement profile due to changes in interphase properties as predicted using the composite model were compared with the experimental measurements. The predictions were in good agreement with the experimentally observed trends. The out-of-plane displacement of the rod increased significantly when a thin compliant interlayer was introduced. A silane coupling agent improved the interfacial adhesion and reduced the nonuniformity of the displacement profile in the whole composite region. Furthermore, the measured displacement profile can also be used to estimate the effective piezoelectric constants $\bar{d}_{33}$ of the composite.

The study of electromechanical coupling in piezocomposites was further developed by investigating the hydrostatic performance of 1-3 piezocomposites, an important issue in design of piezocomposites for low frequency applications. Emphasis was placed on determining the stress transferred between the passive matrix and the active piezoceramic rods and using this data to indicate the level of electromechanical coupling. The stress field in the piezoelectric ceramic under hydrostatic loading was predicted using the analytical micromechanical model developed and a finite element model as well. Optimal electromechanical coupling was achieved when a certain favorable stress field was induced in the piezoceramic.

The key principle in designing a piezoelectric ceramic-polymer composite is to maximize the electromechanical coupling. Maximum coupling is achieved by building a composite structure which transfers the applied external stresses to the composite's piezoelectric component in a pattern that most nearly approximates the piezoceramic's maximally coupled stress patterns. This investigation has shown that the improved hydrostatic performance of 1-3 piezocomposites comes from two major effects: the axial stress amplification and the lateral stress reduction in the piezoelectric rods. Thus, in designing 1-3 piezocomposites for better hydrostatic behavior, the primary goal is to increase the axial stress and to reduce the lateral stress in the piezoceramic rods.

The micromechanics model developed was used to examine systematically the effective hydrostatic piezoelectric constants $\bar{d}_h$, $\bar{g}_h$ and the figure of merit, $\bar{d}_h \bar{g}_h$. Parametric studies were performed to assess the influence of matrix stiffness, rod aspect ratio, interlayer stiffness, and rod volume fraction on the hydrostatic piezoelectric constants. Increasing the aspect ratio significantly increased the $\bar{d}_h$ due to axial stress amplification and increased load transfer. This effect saturates for $2l/d > 500$, where the solution approaches the values predicted by a generalized plane strain-model. Even though a large aspect ratio would increase hydrostatic

sensitivity, piezocomposites are typically fabricated with small rod aspect ratios due to poling limitations. The properties of these piezocomposites are more accurately modeled by a finite concentric cylinder model.

The $\bar{d}_h$ can also be increased by decreasing the matrix stiffness or introducing a compliant interlayer around the PZT rods. Decreasing the matrix stiffness causes axial stress amplification, which leads to higher $\bar{d}_h$ values. However, difficulties may exist in fabricating an entire composite with a very compliant matrix. A compliant interlayer significantly increases the $\bar{d}_h$ by effectively attenuating the lateral stress in the PZT rods without decreasing the overall stiffness of the composite. A compliant interlayer with smaller Poisson's ratio can further increase the $\bar{d}_h$ of the 1-3 piezocomposite.

To improve the hydrostatic performance of a 1-3 piezocomposite further, one must tailor the interlayer to enhance both reduction in lateral stress and axial stress amplification. It has been shown theoretically that an interlayer mechanically graded along the axis of the rod, such that it is stiffer at the edges of the rod to enhance load transfer and axial stress amplification and softer along the interior region of the rod to reduce lateral stresses, should be able to exploit both effects. This optimal interlayer design provides improved electromechanical coupling and design flexibility.

Although the current work is focused on the electromechanical behavior of 1-3 piezocomposites at low frequency, the research results and conceptual understanding obtained have importance for optimizing the design of a piezocomposite in other applications as well.

5.2 Directions for Future Work

One strength of this micromechanical analysis is the ability to explore better approaches to optimization of the electromechanical behavior of piezocomposites. The method can be used to

study the effect of the piezoceramic/polymer interface/interphase further. The results could provide a sound base for optimal interface/interphase design and control in piezocomposites.

The micromechanics methods can be applied to study piezoelectric composites with other geometrical configurations such as 2-2 piezocomposites and composites with particulates. The methods can also be used to investigate other coupled phenomena in composite materials, such as thermo-mechanical and pyroelectric effects.

The micro-interferometric method is ideally suited to investigate the local deformation in piezocomposites, especially near the ceramic/polymer interface. Accurate measurement of the effective piezoelectric constants for the piezocomposites is still a difficulty in practical applications of the composite materials. The interferometer could be adapted to measure the true effective piezoelectric constant $\bar{d}_{33}$ for a composite.

The experimental method can also be used to investigate dynamic response of the piezocomposites at higher frequencies. The method can be used to measure different types of resonance modes of piezocomposites and to study rod-rod interactions. A significant amount of work remains to be done in this direction.

BIBLIOGRAPHY

Benveniste, Y. 1993a. "Universal Relations in Piezoelectric Composites with Eigenstress and Polarization Fields, Part I. Binary Media: Local Fields and Effective Behavior", *Journal of Applied Mechanics*, **60**(2): 265-269.

Benveniste, Y. 1993b. "Universal Relations in Piezoelectric Composites with Eigenstress and Polarization Fields, Part II. Multiphase Media: Effective Behavior", *Journal of Applied Mechanics*, **60**(2): 270-275.

Benveniste, Y. 1994a. "On the Micromechanics of Fibrous Piezoelectric Composites", *Mechanics of Materials*, **18**(3): 183-193.

Benveniste, Y. 1994b. "Exact Results Concerning the Local Fields and Effective Properties in Piezoelectric Composites", *Journal of Engineering Materials and Technology*, **116**(3): 260-267.

Benveniste, Y., and G. J. Dvorak. 1992. "Uniform Fields and Universal Relations in Piezoelectric Composites", *Journal of the Mechanics and Physics of Solids*, **40**: 1295-1312.

Cao, W., Q. M. Zhang and L. E. Cross. 1992. "Theoretical Study on the Static Performance of Piezoelectric Ceramic-Polymer Composites with 1-3 Connectivity", *Journal of Applied Physics*, **72**(12): 5814-5821.

Chan, H. L. W., and J. Unsworth. 1989. "Simple Model for Piezoelectric Ceramic/Polymer 1-3 Composites used in Ultrasonic Transducer Applications", *IEEE Transactions on Ultrasonics, Ferroelectrics, and Frequency Control*, **36**(4): 434-441.

Dokmeci, M. C. 1980. "Recent Advances: Vibrations of Piezoelectric Crystals", *International Journal of Engineering Science*, **18**(3-A): 431-448.

Dunn, M. L., and M. Taya. 1993. "Micromechanics Predictions of the Effective Electroelastic Moduli of Piezoelectric Composites", *International Journal of Solids and Structures*, **30**(2): 161-175.

Gururaja, T. R., A. Safari, R. E. Newnham, and L. E. Cross. 1988. "Piezoelectric Ceramic-Polymer Composites for Transducer Applications", *Electronic Ceramics*, L. M. Levinson ed. New York: Marcel Dekker.

Gururaja, T. R., W. A. Schulze, L. E. Cross, L. E. Cross, R. E. Newnham, B. A. Auld, and Y. J. Wang. 1985. "Piezoelectric Composite Materials for Ultrasonic Transducer Applications. Part I: Resonant Modes of Vibration of PZT Rod-Polymer Composites", *IEEE Transaction on Sonics and Ultrasonics*, **SU-32**(4): 481-498.

Hashin, Z. 1979. "Analysis of Properties of Fiber Composites with Anisotropic Constituents", *Journal of Applied Mechanics*, **46**: 543-550.

Hashin, Z., and B. W. Rosen. 1964. "The Elastic Moduli of Fiber-Reinforced Materials", *Journal of Applied Mechanics*, **31**(3): 223-232.

Haun, M. J., and R. E. Newnham. 1986. "An Experimental and Theoretical Study of 1-3 and 1-3-0 Piezoelectric PZT-Polymer Composites Hydrophone Applications", *Ferroelectrics*, **68**(1): 123-139.

Institute of Electrical and Electronics Engineers. 1978. "IEEE Standard on Piezoelectricity", *IEEE Std. 176-1978.*

Ikeda, T. 1990. *Fundamentals of Piezoelectricity*. Oxford: Oxford University Press.

Jaffe, B., W. R. Cook and H. Jaffe. 1971. *Piezoelectric Ceramics*. New York: Academic Press.

Jensen, H. 1991. "Determination of Macroscopic Electro-Mechanical Characteristics of 1-3 Piezoceramic/Polymer Composites by a Concentric Tube Model", *IEEE Transactions on Ultrasonics, Ferroelectrics, and Frequency Control*, **38**(6): 591-594.

Kim, C., K. M. Rittenmyer and M. Kahn. 1994. "1-1-3 Piezocomposite For Hydrophone Transducer", *Ferroelectrics*, **156**(1): 19-24.

Klicker, K. A. 1980. *Piezoelectric Composite with 3-1 Connectivity for Transducer Applications*. The Pennsylvania State University.

Lees, S., and C. L. Davidson. 1977. "Ultrasonic Measurement on Some Mineral Filled Plastics", *IEEE Transaction on Sonics and Ultrasonics*, **SU**(24): 222-225.

Li, L., K. M. Durkin and N. R. Sottos. 1994. "The Influence of Interface/Interphase Regions on the Performance of Piezocomposites", The American Society for Composites

Ninth Technical Conference, Newark, Delaware. Lancaster: Technomic Publishing Company, Inc., 5-12.

Li, L., and N. R. Sottos. 1995. "Improving Hydrostatic Performance of 1-3 Piezocomposites", *Journal of Applied Physics*, **77**(9): 4595-4603.

Monchalin, J. P., J. D. Aussel, R. Heon, C. K. Jen, A. Boudreault, and R. Bernier. 1989. "Measurement of In-Plane and Out-of-Plane Ultrasonic Displacements by Optical Heterodyne Interferometry", *Journal of Nondestructive Evaluation*, **8**(2): 121-133.

Morgan Matroc Inc. 1989. *Piezoelectric Technology Data for Designers*. Bedford: Morgan Matroc Inc.

Newnham, R. E. 1986. "Composite Electroceramics", *Ferroelectrics*, **68**(1): 1-32.

Nye, J. F. 1957. *Physical Properties of Crystals*. Oxford: Oxford University Press.

Pauer, L. A. 1973. "Flexible Piezoelectric Materials", 1973 IEEE International Convention and Exposition, New York. New York: IEEE, 1-5.

Rittenmyer, K. M., and P. S. Dubbelday. 1992. "Direct Measurement of the Temperature-Dependent Piezoelectric Coefficients of Composite Materials by Laser Doppler Vibrometry", *Journal of the Acoustical Society of America*, **91**(4): 2254-2260.

Ryan, M. J., W. R. Scott and N. R. Sottos. 1990. "Scanning Heterodyne Micro-interferometry for High Resolution Contour Mapping", in *Review of Progress in Quantitative Nondestructive Evaluation*. New York: Plenum Press.

Sherrit, S., H. D. Wiederick, and B. K. Mukherjee. 1992. "Stress Isolation PZT-Air Composites", *Ferroelectrics*, **132**(1): 61-68

Smith, W. A. 1989. "The Role of Piezocomposites in Ultrasonic Transducers", Proceedings of the 1989 IEEE Ultrasonic Symposium, 755-766.

Smith, W. A. 1992. "The Key Design Principle for Piezoelectric Ceramic/Polymer Composites", Conference on Recent Advances in Adaptive and Sensory Materials and Their Applications, Blacksburg, Va. Lancaster: Technomic Publishing Company, Inc., 825-838.

Smith, W. A. 1993. "Modeling 1-3 Composite Piezoelectrics: Hydrostatic Response", *IEEE Transactions on Ultrasonics, Ferroelectrics, and Frequency Control*, **40**(1): 41-49.

Sottos, N. R., L. Li, W. R. Scott, and M. J. Ryan. 1993. "Micromechanical Behavior of 1-3 Piezocomposites", *Smart Structures and Materials 1993*, Proceedings of SPIE, Orlando, Fla., 87-96.

Sottos, N. R., W. R. Scott and R. L. McCullough. 1991. "Micro-interferometry for Measurement of Thermal Displacements at Fiber/Matrix Interfaces", *Experimental Mechanics*, **31**(2): 98-103.

Wang, Y., and B. A. Auld. 1985. "Acoustic Wave Propagation in One-Dimensional Periodic Composites", Proceedings of the 1985 IEEE Ultrasonic Symposium, San Francisco, 637-641.

Zhang, Q. M., W. Cao, J. Zhao, L. E. Cross. 1994. "Piezoelectric Performance of Piezoceramic-Polymer Composites with 2-2 Connectivity -- A Combined Theoretical and Experimental Study", *IEEE Transactions on Ultrasonics, Ferroelectrics, and Frequency Control*, **41**(4): 556-564.

APPENDIX

The coefficients in Eq. (2.30) are given by

$$\left.\begin{aligned}
&\tilde{P}_1 = c_{11}^{(1)}(e_{15}^{(1)}e_{15}^{(1)} + c_{44}^{(1)}e_{11}^{(1)}) \\
&\tilde{P}_2 = \left[2c_{13}^{(1)}e_{15}^{(1)}(e_{15}^{(1)} + e_{31}^{(1)}) - c_{11}^{(1)}(c_{33}^{(1)}e_{11}^{(1)} + c_{44}^{(1)}e_{33}^{(1)}) + c_{13}^{(1)}c_{13}^{(1)}e_{11}^{(1)}\right. \\
&\left. + 2c_{13}^{(1)}c_{44}^{(1)}e_{11}^{(1)} - 2c_{11}^{(1)}e_{15}^{(1)}e_{33}^{(1)} - c_{44}^{(1)}e_{31}^{(1)}e_{31}^{(1)})\right]m^2 \\
&\tilde{P}_3 = \left[c_{11}^{(1)}(e_{33}^{(1)}e_{33}^{(1)} + c_{33}^{(1)}e_{33}^{(1)}) + c_{33}^{(1)}\left[c_{44}^{(1)}e_{11}^{(1)} + (e_{15}^{(1)} + e_{31}^{(1)})^2\right]\right. \\
&\left. - 2e_{31}^{(1)}e_{33}^{(1)}(c_{13}^{(1)} + c_{44}^{(1)}) - c_{13}^{(1)}\left[e_{33}^{(1)}(c_{13}^{(1)} + 2c_{44}^{(1)}) + 2e_{15}^{(1)}e_{33}^{(1)}\right]\right]m^4 \\
&\tilde{P}_4 = c_{44}^{(1)}(c_{33}^{(1)}e_{33}^{(1)} + e_{33}^{(1)}e_{33}^{(1)})m^6
\end{aligned}\right\} \qquad \text{(A1)}$$

The functions $h_{jn}^{(1)}$, where j=1,2,...24, in Eqs. (2.40) to (2.47) can be expressed in terms of modified Bessel functions of the first kind I_0, I_1 and elastic constants of the piezoelectric ceramic as follows:

$$h_{1n}^{(1)}(r) = \alpha_1 I_1(\alpha_1 r) \qquad \text{(A2)}$$

$$h_{2n}^{(1)}(r) = \mathrm{Re}\left[a_2 I_1(a_2 r)\right] \qquad \text{(A3)}$$

$$h_{3n}^{(1)}(r) = \mathrm{Im}\left[a_2 I_1(a_2 r)\right] \qquad \text{(A4)}$$

$$h_{4n}^{(1)}(r) = -\beta_1 I_0(\alpha_1 r) \qquad \text{(A5)}$$

$$h_{5n}^{(1)}(r) = \mathrm{Re}\left[-b_2 I_0(a_2 r)\right] \qquad \text{(A6)}$$

$$h_{6n}^{(1)}(r) = \mathrm{Im}\left[-b_2 I_0(a_2 r)\right] \qquad \text{(A7)}$$

$$h_{7n}^{(1)}(r)=\left[c_{11}^{(1)}\alpha_1{}^2/2-(c_{13}^{(1)}\beta_1+e_{31}^{(1)}\gamma_1)\mu_n\right]I_0(\alpha_1 r)+c_{12}^{(1)}\alpha_1/r\,I_1(\alpha_1 r)+c_{11}^{(1)}\alpha_1{}^2/2\,I_2(\alpha_1 r) \tag{A8}$$

$$h_{8n}^{(1)}(r)=\mathrm{Re}\left\{\left[c_{11}^{(1)}\alpha_2{}^2/2-(c_{13}^{(1)}\beta_2+e_{31}^{(1)}\gamma_2)\mu_n\right]I_0(\alpha_2 r)+c_{12}^{(1)}\alpha_2/r\,I_1(\alpha_2 r)+c_{11}^{(1)}\alpha_2{}^2/2\,I_2(\alpha_2 r)\right\} \tag{A9}$$

$$h_{9n}^{(1)}(r)=\mathrm{Im}\left\{\left[c_{11}^{(1)}\alpha_2{}^2/2-(c_{13}^{(1)}\beta_2+e_{31}^{(1)}\gamma_2)\mu_n\right]I_0(\alpha_2 r)+c_{12}^{(1)}\alpha_2/r\,I_1(\alpha_2 r)+c_{11}^{(1)}\alpha_2{}^2/2\,I_2(\alpha_2 r)\right\} \tag{A10}$$

$$h_{10n}^{(1)}(r)=\left[c_{12}^{(1)}\alpha_1{}^2/2-(c_{13}^{(1)}\beta_1+e_{31}^{(1)}\gamma_1)\mu_n\right]I_0(\alpha_1 r)+c_{11}^{(1)}\alpha_1/r\,I_1(\alpha_1 r)+c_{12}^{(1)}\alpha_1{}^2/2\,I_2(\alpha_1 r) \tag{A11}$$

$$h_{11n}^{(1)}(r)=\mathrm{Re}\left\{\left[c_{12}^{(1)}\alpha_2{}^2/2-(c_{13}^{(1)}\beta_2+e_{31}^{(1)}\gamma_2)\mu_n\right]I_0(\alpha_2 r)+c_{11}^{(1)}\alpha_2/r\,I_1(\alpha_2 r)+c_{12}^{(1)}\alpha_2{}^2/2\,I_2(\alpha_2 r)\right\} \tag{A12}$$

$$h_{12n}^{(1)}(r)=\mathrm{Im}\left\{\left[c_{12}^{(1)}\alpha_2{}^2/2-(c_{13}^{(1)}\beta_2+e_{31}^{(1)}\gamma_2)\mu_n\right]I_0(\alpha_2 r)+c_{11}^{(1)}\alpha_2/r\,I_1(\alpha_2 r)+c_{12}^{(1)}\alpha_2{}^2/2\,I_2(\alpha_2 r)\right\} \tag{A13}$$

$$h_{13n}^{(1)}(r)=\left[c_{13}^{(1)}\alpha_1{}^2/2-(c_{33}^{(1)}\beta_1+e_{33}^{(1)}\gamma_1)\mu_n\right]I_0(\alpha_1 r)+c_{13}^{(1)}\alpha_1/r\,I_1(\alpha_1 r)+c_{13}^{(1)}\alpha_1{}^2/2\,I_2(\alpha_1 r) \tag{A14}$$

$$h_{14n}^{(1)}(r)=\mathrm{Re}\left\{\left[c_{13}^{(1)}\alpha_2{}^2/2-(c_{33}^{(1)}\beta_2+e_{33}^{(1)}\gamma_2)\mu_n\right]I_0(\alpha_2 r)+c_{13}^{(1)}\alpha_2/r\,I_1(\alpha_2 r)+c_{13}^{(1)}\alpha_2{}^2/2\,I_2(\alpha_2 r)\right\} \tag{A15}$$

$$h_{15n}^{(1)}(r)=\mathrm{Im}\left\{\left[c_{13}^{(1)}\alpha_2{}^2/2-(c_{33}^{(1)}\beta_2+e_{33}^{(1)}\gamma_2)\mu_n\right]I_0(\alpha_2 r)+c_{13}^{(1)}\alpha_2/r\,I_1(\alpha_2 r)+c_{13}^{(1)}\alpha_2{}^2/2\,I_2(\alpha_2 r)\right\} \tag{A16}$$

$$h_{16n}^{(1)}(r)=-\alpha_1\left[c_{44}^{(1)}(\mu_n+\beta_1)+e_{15}^{(1)}\gamma_1\right]I_1(\alpha_1 r) \tag{A17}$$

$$h_{17n}^{(1)}(r) = \mathrm{Re}\left\{-\alpha_2\left[c_{44}^{(1)}(\mu_n + \beta_2) + e_{15}^{(1)}\gamma_2\right] I_1(\alpha_2 r)\right\} \tag{A18}$$

$$h_{18n}^{(1)}(r) = \mathrm{Im}\left\{-\alpha_2\left[c_{44}^{(1)}(\mu_n + \beta_2) + e_{15}^{(1)}\gamma_2\right] I_1(\alpha_2 r)\right\} \tag{A19}$$

$$h_{19n}^{(1)}(r) = \alpha_1\left[-e_{15}^{(1)}(\mu_n + \beta_1) + \varepsilon_{11}^{(1)}\gamma_1\right] I_1(\alpha_1 r) \tag{A20}$$

$$h_{20n}^{(1)}(r) = \mathrm{Re}\left\{\alpha_2\left[-e_{15}^{(1)}(\mu_n + \beta_2) + \varepsilon_{11}^{(1)}\gamma_2\right] I_1(\alpha_2 r)\right\} \tag{A21}$$

$$h_{21n}^{(1)}(r) = \mathrm{Im}\left\{\alpha_2\left[-e_{15}^{(1)}(\mu_n + \beta_2) + \varepsilon_{11}^{(1)}\gamma_2\right] I_1(\alpha_2 r)\right\} \tag{A22}$$

$$\begin{aligned} h_{22n}^{(1)}(r) = {} & \left[e_{31}^{(1)}\alpha_1{}^2/2 - (e_{33}^{(1)}\beta_1 - \varepsilon_{33}^{(1)}\gamma_1)\mu_n\right] I_0(\alpha_1 r) + e_{31}^{(1)}\alpha_1/r\, I_1(\alpha_1 r) \\ & + e_{31}^{(1)}\alpha_1{}^2/2\, I_2(\alpha_1 r) \end{aligned} \tag{A23}$$

$$\begin{aligned} h_{23n}^{(1)}(r) = {} & \mathrm{Re}\left\{\left[e_{31}^{(1)}\alpha_2{}^2/2 - (e_{33}^{(1)}\beta_2 - \varepsilon_{33}^{(1)}\gamma_2)\mu_n\right] I_0(\alpha_2 r) + e_{31}^{(1)}\alpha_2/r\, I_1(\alpha_2 r)\right. \\ & \left. + e_{31}^{(1)}\alpha_2{}^2/2\, I_2(\alpha_2 r)\right\} \end{aligned} \tag{A24}$$

$$\begin{aligned} h_{24n}^{(1)}(r) = {} & \mathrm{Im}\left\{\left[e_{31}^{(1)}\alpha_2{}^2/2 - (e_{33}^{(1)}\beta_2 - \varepsilon_{33}^{(1)}\gamma_2)\mu_n\right] I_0(\alpha_2 r) + e_{31}^{(1)}\alpha_2/r\, I_1(\alpha_2 r)\right. \\ & \left. + e_{31}^{(1)}\alpha_2{}^2/2\, I_2(\alpha_2 r)\right\} \end{aligned} \tag{A25}$$

In region 2 and region 3 the complementary solution for the displacements and stresses are of the form

$$
\left.
\begin{aligned}
u_c^{(i)} &= -\frac{1}{c_{11}^{(i)} - c_{12}^{(i)}} \frac{\partial^2 F^{(i)}}{\partial r \partial z} \\
w_c^{(i)} &= \frac{1}{c_{11}^{(i)} - c_{12}^{(i)}} \left[\frac{2c_{11}^{(i)}}{c_{11}^{(i)} + c_{12}^{(i)}} \nabla^2 F^{(i)} - \frac{\partial^2 F^{(i)}}{\partial z^2} \right] \\
T_{rr\ c}^{(i)} &= \frac{\partial}{\partial z} \left[\frac{c_{12}^{(i)}}{c_{11}^{(i)} + c_{12}^{(i)}} \nabla^2 F^{(i)} - \frac{\partial^2 F^{(i)}}{\partial r^2} \right] \\
T_{qq\ c}^{(i)} &= \frac{\partial}{\partial z} \left[\frac{c_{12}^{(i)}}{c_{11}^{(i)} + c_{12}^{(i)}} \nabla^2 F^{(i)} - \frac{1}{r} \frac{\partial F^{(i)}}{\partial r} \right] \\
T_{zz\ c}^{(i)} &= \frac{\partial}{\partial z} \left[\frac{2c_{11}^{(i)} + c_{12}^{(i)}}{c_{11}^{(i)} + c_{12}^{(i)}} \nabla^2 F^{(i)} - \frac{\partial^2 F^{(i)}}{\partial z^2} \right] \\
T_{rz\ c}^{(i)} &= \frac{\partial}{\partial z} \left[\frac{c_{11}^{(i)}}{c_{11}^{(i)} + c_{12}^{(i)}} \nabla^2 F^{(i)} - \frac{\partial^2 F^{(i)}}{\partial z^2} \right]
\end{aligned}
\right\} \qquad \text{(A26)}
$$

where $F^{(i)}$ is Love's stress function and the superscript i=2,3 for the interlayer and matrix region respectively. The functions $h_{jn}^{(i)}$ and $g_{jn}^{(i)}$, where i=2,3 and j=1,2,...12, in Eqs (2.52) to (2.58) can be expressed in terms of modified Bessel functions of the first and second kind I_0, I_1, K_0, K_1 and the elastic constants as follows:

$$
h_{1n}^{(i)} = -\left(\frac{1}{c_{11}^{(i)} - c_{12}^{(i)}} \right) m_n^2 I_1(m_n r) \qquad \text{(A27)}
$$

$$
h_{2n}^{(i)} = -\left(\frac{1}{c_{11}^{(i)} - c_{12}^{(i)}} \right) m_n^3 r I_0(m_n r) \qquad \text{(A28)}
$$

$$
h_{3n}^{(i)} = \left(\frac{1}{c_{11}^{(i)} - c_{12}^{(i)}} \right) m_n^2 I_0(m_n r) \qquad \text{(A29)}
$$

$$
h_{4n}^{(i)} = \left(\frac{m_n^2}{c_{11}^{(i)} - c_{12}^{(i)}} \right) \left[\frac{4c_{11}^{(i)}}{c_{11}^{(i)} + c_{12}^{(i)}} I_0(m_n r) + m_n r I_1(m_n r) \right] \qquad \text{(A30)}
$$

$$h_{5n}^{(i)} = m_n^2\left[-m_n I_0(m_n r) + \frac{1}{r} I_1(m_n r)\right] \tag{A31}$$

$$h_{6n}^{(i)} = m_n^3\left[\left(\frac{c_{12}^{(i)} - c_{11}^{(i)}}{c_{11}^{(i)} + c_{12}^{(i)}}\right) I_0(m_n r) - m_n r I_1(m_n r)\right] \tag{A32}$$

$$h_{7n}^{(i)} = -\frac{m_n^2}{r} I_1(m_n r) \tag{A33}$$

$$h_{8n}^{(i)} = m_n^3\left(\frac{c_{12}^{(i)} - c_{11}^{(i)}}{c_{11}^{(i)} + c_{12}^{(i)}}\right) I_0(m_n r) \tag{A34}$$

$$h_{9n}^{(i)} = m_n^3 I_0(m_n r) \tag{A35}$$

$$h_{10n}^{(i)} = m_n^3\left[\left(\frac{4c_{11}^{(i)} + 2c_{12}^{(i)}}{c_{11}^{(i)} + c_{12}^{(i)}}\right) I_0(m_n r) + m_n r I_1(m_n r)\right] \tag{A36}$$

$$h_{11n}^{(i)} = m_n^3 I_1(m_n r) \tag{A37}$$

$$h_{12n}^{(i)} = m_n^3\left[\left(\frac{2c_{11}^{(i)}}{c_{11}^{(i)} + c_{12}^{(i)}}\right) I_1(m_n r) + m_n r I_0(m_n r)\right] \tag{A38}$$

$$g_{1n}^{(i)} = \left(\frac{1}{c_{11}^{(i)} - c_{12}^{(i)}}\right) m_n^2 K_1(m_n r) \tag{A39}$$

$$g_{2n}^{(i)} = \left(\frac{1}{c_{11}^{(i)} - c_{12}^{(i)}}\right) m_n^3 r K_0(m_n r) \tag{A40}$$

$$g_{3n}^{(i)} = \left(\frac{1}{c_{11}^{(i)} - c_{12}^{(i)}}\right) m_n^2 K_0(m_n r) \tag{A41}$$

$$g_{4n}^{(i)} = \left(\frac{m_n^2}{c_{11}^{(i)} - c_{12}^{(i)}} \right) \left[\frac{-4c_{11}^{(i)}}{c_{11}^{(i)} + c_{12}^{(i)}} K_0(m_n r) + m_n r K_1(m_n r) \right] \tag{A42}$$

$$g_{5n}^{(i)} = m_n^2 \left[-m_n K_0(m_n r) - \frac{1}{r} K_1(m_n r) \right] \tag{A43}$$

$$g_{6n}^{(i)} = m_n^3 \left[\left(\frac{c_{11}^{(i)} - c_{12}^{(i)}}{c_{11}^{(i)} + c_{12}^{(i)}} \right) K_0(m_n r) - m_n r K_1(m_n r) \right] \tag{A44}$$

$$g_{7n}^{(i)} = \frac{m_n^2}{r} K_1(m_n r) \tag{A45}$$

$$g_{8n}^{(i)} = m_n^3 \left(\frac{c_{11}^{(i)} - c_{12}^{(i)}}{c_{11}^{(i)} + c_{12}^{(i)}} \right) K_0(m_n r) \tag{A46}$$

$$g_{9n}^{(i)} = m_n^3 K_0(m_n r) \tag{A47}$$

$$g_{10n}^{(i)} = m_n^3 \left[\left(\frac{4c_{11}^{(i)} + 2c_{12}^{(i)}}{c_{11}^{(i)} + c_{12}^{(i)}} \right) K_0(m_n r) + m_n r K_1(m_n r) \right] \tag{A48}$$

$$g_{11n}^{(i)} = -m_n^3 K_1(m_n r) \tag{A49}$$

$$g_{12n}^{(i)} = m_n^3 \left[\left(\frac{4c_{11}^{(i)}}{c_{11}^{(i)} + c_{12}^{(i)}} \right) K_1(m_n r) - m_n r K_0(m_n r) \right] \tag{A50}$$

VITA

Li Li graduated from the University of Science and Technology of China in 1985 with a bachelor's degree in mechanical engineering. After working five years as a research engineer in China, he came to the University of Illinois at Urbana-Champaign. He earned his master's degree in Theoretical and Applied Mechanics in January 1992. Since then he has continued his graduate study as a doctoral student in the Department of Theoretical and Applied Mechanics. Mr. Li's research interests include experimental mechanics, composite materials, electronic packaging and nondestructive evaluation. He is a student member of the American Society of Mechanical Engineers and the Society of Photo-Optical Instrumentation Engineers.

Mr. Li has coauthored three journal articles and other technical publications based on his graduate research. He has accepted a position as development staff engineer with IBM Corporation in Endicott, N.Y.